Development of a Tridyne Microthruster for CubeSat Applications

Brian Henderson

A thesis
submitted in partial fulfillment of the
requirements for the degree of

Master of Science

University of Washington

2020

Committee:

James C. Hermanson

Carl Knowlen

Program Authorized to Offer Degree:
Aeronautics & Astronautics

University of Washington

Abstract

Development of a Tridyne Microthruster for CubeSat Applications

Brian Henderson

Supervisory Committee:
Associate Professor James C. Hermanson
Aeronautics & Astronautics

A warm gas thruster using a catalyzed tridyne propellant (85% N_2, 10% H_2 and 5% O_2 by volume) was developed at the University of Washington in collaboration with Aerojet Rocketdyne for the purposes of advancing micro-propulsion technologies. Chemical equilibrium analyses were conducted to estimate performance and establish a design parameter space. Trade analyses were performed to establish the theoretical design parameters of a 1.5U (10x10x15 cm^3) Tridyne propulsion unit and the ability to compete with the current state-of-the-art in low-complexity micropropulsion applications. A 1.5U Tridyne micropropulsion system is estimated to achieve total impulses up to 1400 N-s dependent on propellant storage pressure. A high-level computer aided design was completed with use of commercial off-the-shelf, flight-heritage components and a custom engineered, additively-manufactured propellant tank by Aerojet Rocketdyne.

A bench-top prototype was designed, constructed and tested to demonstrate the technology and performance capabilities of the flight-weight design while providing greater diagnostic access, measuring mass flow rate, pressure drop across the catalyst bed, and temperatures at the beginning, middle and end of the catalyst bed. The nominal mass flow rate is 1.0 g/s with an anticipated thrust of 1 N. A laboratory environment was set-up to test the bench-top thruster, including an electro-mechanically controlled mass flow system accessing gas cylinders of both Tridyne and nitrogen and an inline accumulator bottle with comparable

volume to the flight-weight propellant tank to simulate a passively pressure regulated flow regime. The mass flow delivery and data collection and storage is controlled by a custom programmed LabVIEW GUI.

The bench-top thruster was tested for two different Tridyne reaction configurations: ignition via flow over a heated pebble bed, and ignition via flow over a catalyst bed composed of the iridium-based S-405 catalyst. A complete reaction reaching the adiabatic flame temperature was observed in both thruster configurations, with the heated pebble bed only reaching a steady state reaction at the thruster exit for flow rates under 0.8 g/s. The catalyst bed configuration thruster reached a complete Tridyne reaction after 0.6" or less of S-405 catalyst flow length. The catalyst bed configuration thruster has a characteristic velocity efficiency in the range of 0.78 - 0.94 depending on the mass flow rate and preheat temperature, with a much higher efficiency in range of 0.92 - 1.0 anticipated for the flight-weight configuration due to a shorter distance between the reaction front and nozzle. Chemical reaction startup rise times in the range of 5-10 seconds and a maximum estimated propellant flow time of 720 seconds indicate a Tridyne thruster technology is best suited for missions requiring a minimal number of startup cycles. Phase II will perform a full-scale integration of flight-geometry hardware and extensive testing under both laboratory (as in this study) and simulated space conditions.

TABLE OF CONTENTS

LIST OF FIGURES

LIST OF TABLES

LIST OF ABBREVIATIONS

1 U	CubeSat Unit Size	[10x10x10 cm^3]
ρ	Density	[$kg\ m^{-3}$]
A	Area	[m^2]
P	Pressure	[Pa]
u	Velocity	[$m\ s^{-1}$]
h	Specific Enthalpy	[$J\ kg^{-1}$]
F	Force	[N]
c_f	Thrust coefficient	
$\dot{m}$	Mass flow rate	[g/s]
I_{sp}	Specific Impulse	[s]
I_{tot}	Total Impulse	[$N\ s$]
ΔV	Change in velocity	[$m\ s^{-1}$]
g_0	Gravitational acceleration	[$m\ s^{-1}$]
$\mathcal{M}$	Mach number	
γ	Adiabatic index	
c_p	Constant pressure heat capacity	[$J\ K^{-1}$]
c_v	Constant volume heat capacity	[$J\ K^{-1}$]
V	Volume	[m^3]
T	Temperature	[K]
R_s	Specific Gas Constant	[$J\ kg^{-1}\ K^{-1}$]

c^*	Characteristic velocity	$[m\ s^{-1}]$
η_{c*}	Characteristic velocity efficiency	
r	Radius	$[m]$
σ_y	Yield Strength	$[MPa]$
t_c	Pressure vessel center wall thickness	$[m]$
t_h	Pressure vessel head wall thickness	$[m]$
L	Length	$[m]$
G	Superficial catalyst bed loading	$[lbm\ s^{-1}in^{-2}]$
a_s	Catalyst bed specific surface area	$[in^2/in^3]$
C_d	Discharge Coefficient	
TRL	Technology Readiness Level	
NASA	National Aeronautics & Space Administration	
CEA	Chemical Equilibrium Analysis	
CAD	Computer Aided Design	
MiPS	MicroPropulsion System	
PID	Plumbing and Instrumentation Diagram	
PWM	Pulse-Width Modulation	
DESO	Double-End ShutOff	
GUI	Graphical User Interface	
JCATI	Joint Center for Aerospace Technology Innovation	

ACKNOWLEDGMENTS

I would like to thank my advisors Dr. James Hermanson and Dr. Carl Knowlen for their patience, wisdom and support. The two of you are the best advisors I could have ever asked for and have served as exceptionally stabilizing, encouraging and inspiring individuals in my life. I would also like to thank Nathaniel Barry and Peter Sciuto III for their help in setting up the lab and running experiments. Lastly I want to thank my friend and undergraduate research partner Michael Sherburne, who provided invaluable electrical engineering advice to ensure I powered all of the electronics in the lab cleanly and safely.

This effort is funded by the State of Washington's Joint Center for Aerospace Technology Innovation (JCATI) and partnered with Aerojet Rocketydyne of Redmond, WA. Thank you to Matt Stevenson, Christopher Sebastian, and others at Aerojet Rocketdyne for their engineering advice and provision of S-405 catalyst.

DEDICATION

to the stars!

Chapter 1

INTRODUCTION

Prætera gigni pariter cum corpore, et una

Crescere sentinus, pariterque senescere mentem

—Lucretius, *de rerum natura*, Liber III.

Very small satellites ("CubeSats") are increasingly being deployed for near-earth space applications. In addition to their popularity with universities for educational efforts, CubeSats are seeing increased use for commercial, scientific, and military application due to their increasing sophistication, combined with very small size, low cost, low mass, and ease of launch. [1] An enabling technology for many of these emerging missions is the ability of CubeSats to perform limited orbital maneuvering, which in turn requires the development and implementation of suitable on-board propulsion systems. [2] Conventional spacecraft propulsion performance capabilities are outlined in Section 1.2.

One candidate propulsion system with demonstrated potential is a "warm gas" thruster that uses a chemical reaction in Tridyne (nominally 85% N_2, 10% H_2 and 5% O_2 by volume) to raise the temperature of a gaseous propellant. This stable, environmentally-friendly, nonflammable and storable propellant is self-heated in the thrust chamber by the chemical reaction resulting from passage through a catalyst bed as illustrated in Fig. 1.1. [3] This technology has been developed by Aerojet Rocketdyne [4], which is serving as the University of Washington's industry partner in this effort funded by the State of Washington's Joint Center for Aerospace Technology Innovation (JCATI).

In a CubeSat application, this propulsion system has an ideal thrust range from 10 mN to 1 N, depending on the mass flow rate, chamber pressure and nozzle throat diameter. The application herein is intended to have 1 N thrust capability per Aerojet Rocketdyne's com-

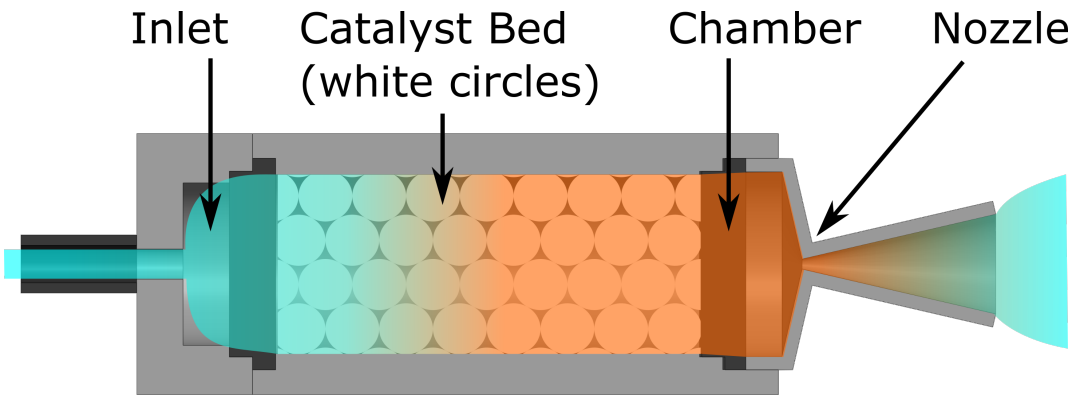

Figure 1.1: Sketch of gas heating from cold (blue) to warm (orange) as it passes over a microthruster catalyst bed.

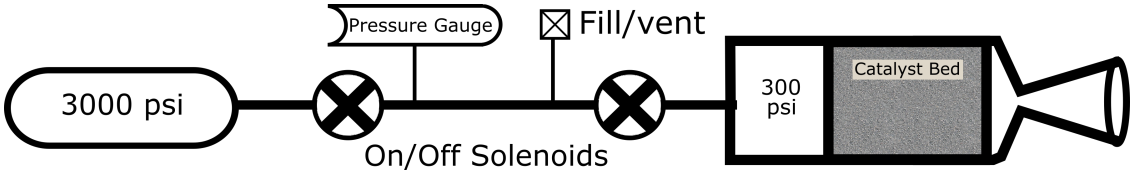

Figure 1.2: Schematic diagram of tridyne thruster configuration.

mercial interest. The proposed 1.5U (10x10x15cm^3) Tridyne propulsion system for CubeSats has a design specific impulse of 146 s and a designed total impulse of approximately 1000 N-s, exceeding the performance of commercially-available vaporizing-liquid systems. [5] The tridyne system offers advantages of system simplicity and low cost, use of a non-toxic and environmentally friendly propellant, and heating power required as is the case for vaporizing-liquid systems.

The simplicity and robustness of the system under development is evident in the component sketch shown in Fig. 1.2. The essential components are a propellant storage tank, control valves, fill/vent and propellant supply lines, and a thrust chamber with catalyst and integral exhaust nozzle. The only electrical requirements are for valve actuation and pressure monitoring as preheating of the catalyst material prior to firing is not necessary with Tridyne. [2] There is no upper limit on the stored Tridyne pressure other than the pressure rating of the storage vessel and conventional energetic payload limitations for CubeSats, though the latter is subject to change dependent on commercial interests. The system is well suited to long-term storage and will be fully re-startable.

The current state and Technology Readiness Level (TRL) of this Tridyne propellant system is between TRL 3 and TRL 4, in that the technology has been demonstrated, tested, and there appear to be no limiting issues. [6] The work demonstrated herein represents Phase I of II in the effort to firmly establish the technology in the category of TRL 5-6. The primary objectives of this effort are to develop a Tridyne microthruster employing S-405 catalyst, establish performance and effectiveness of catalyst, and design and establish competitiveness of a 1.5U Tridyne micropropulsion unit.

1.1 Theory

1.1.1 Catalysts and Chemical Reactions

A significant benefit of Tridyne is that it is inert at standard temperatures and pressures. This means that the reaction pathways in the gaseous mixture - namely, between hydrogen and oxygen - do not have sufficient energy to result in a successful reaction. Gas molecules are always colliding; whether the collisions result in a successful reaction or not depends upon whether the particles collide with sufficient energy to break the pre-existing bonds and form new bonds. This energy required to successfully react the mixture is referred to as the activation energy and is illustrated for an exothermic reaction in Fig. 1.3. [7]

All of the molecules within a given gas mixture will have a certain energy distribution as illustrated in Fig. 1.4. Some of these particles may have energies greater than the activation energy (shown in green), however there is not a sufficient frequency of collisions amongst these particles to propagate a self-sustaining reaction. By adding a catalyst, a lower activation energy reaction pathway enables more particles with sufficient energy to collide and react (shown in red + green). An alternative to maximize the number of successful collisions is to raise the bulk energy of the gas via heating, which will be explored further in Section 2. [7] [8]

The addition of a catalyst enables a reaction to occur at a lower activation energy, however this is not by lowering the activation energy of the original reaction. Instead an alternative reaction pathway is formed between the catalyst and the reactants, in this case Tridyne. In this case, the catalyst S-405 is comprised of an active metal (iridium) supported on an alumina (Al_2O_3) substrate. A high-level overview of the catalyst mechanism will be theorized here considering valence bond theory, electronic band structures and solid state physics, however a more in-depth discussion relies on advanced chemistry and quantum mechanics knowledge beyond the scope of this thesis. The process described below is illustrated in Fig. 1.5. The reaction mechanism is presented in Table 1.1.

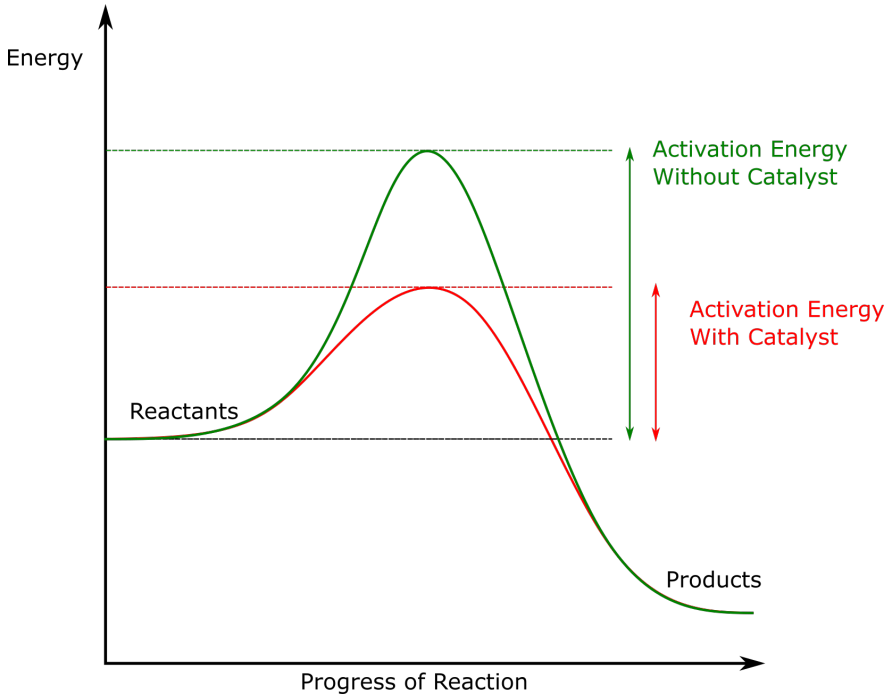

Figure 1.3: Activation energy illustration of Tridyne with and without catalyst.

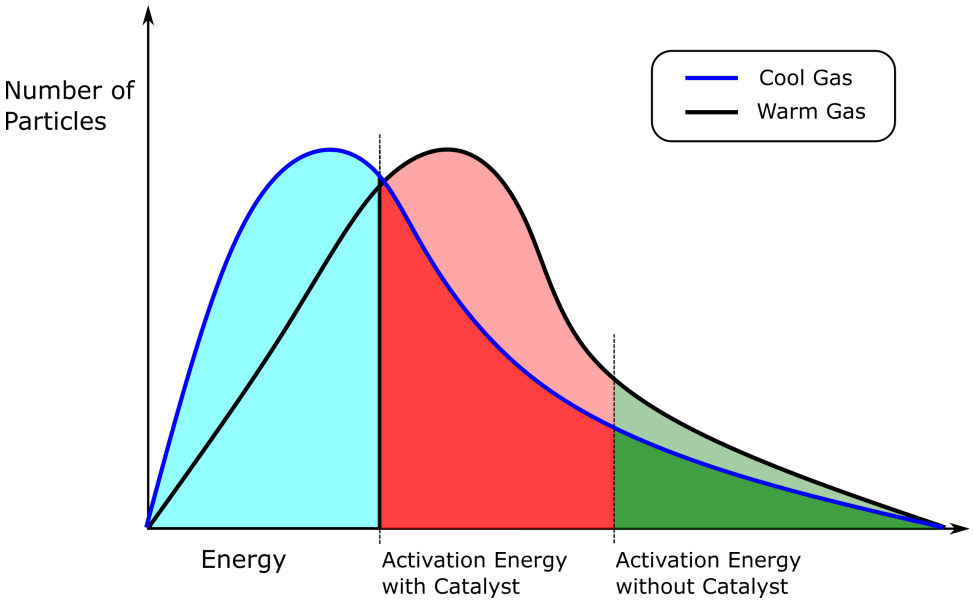

Figure 1.4: Simplified Boltzmann energy distribution of Tridyne for room temperature and pre-heated gas cases with annotated activation energies. [9]

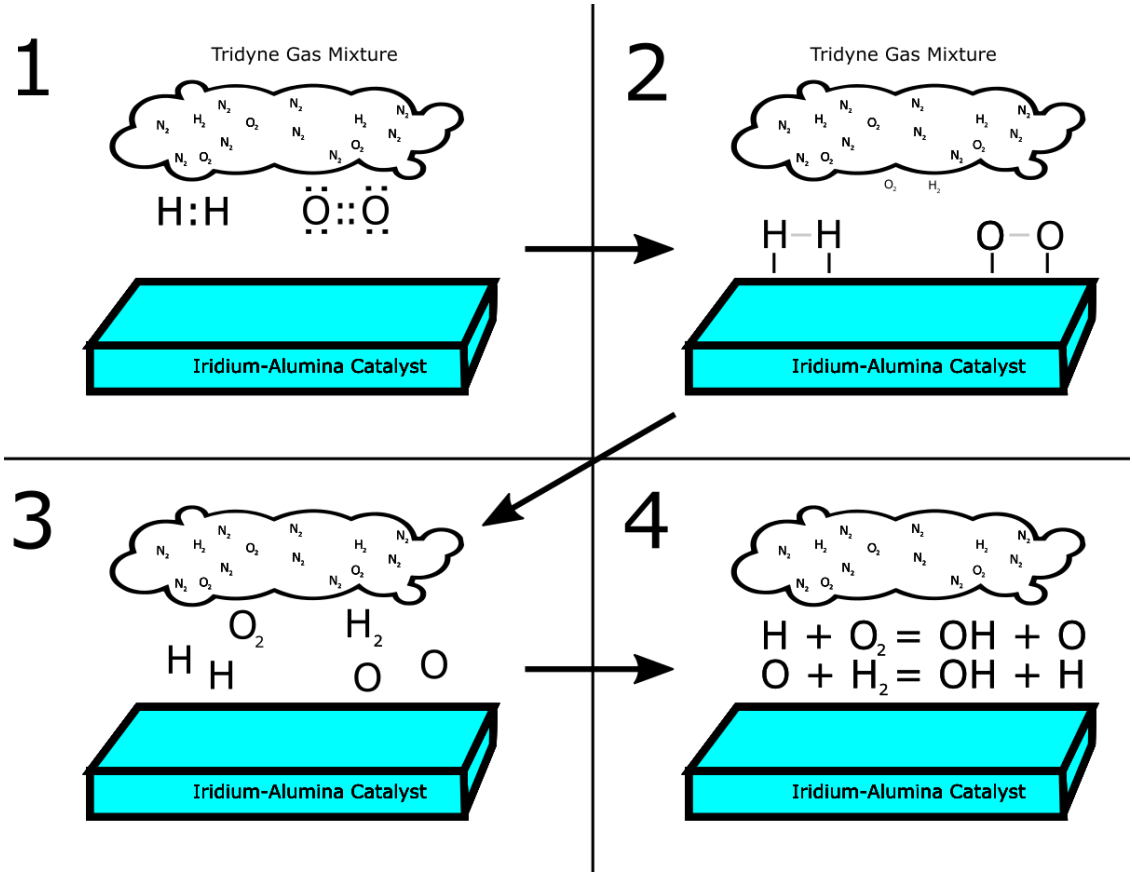

Figure 1.5: Chemisorption illustration of hydrogen and oxygen onto iridium, beginning the branching reaction chain of hydrogen and oxygen. [10]

Table 1.1: Hydrogen-Oxygen branching-propagating reaction mechanism

$$H + O_2 \rightarrow OH + O \quad \text{(branching)}$$
$$O + H_2 \rightarrow OH + H \quad \text{(branching)}$$
$$OH + H_2 \rightarrow H_2O + H \quad \text{(propagating)}$$

Iridium, along with other platinum group metals, is an excellent catalyst due to its unfilled *d*-orbital, which can be thought of as a diffuse electron cloud surrounding the iridium nucleus. This makes the metal paramagnetic to most molecules and enables weak binding to them at the surface of the metal in a process known as adsorption. This bond weakens the bonds within the molecule being adsorbed; in the case of hydrogen and oxygen with iridium, the iridium is such a strong catalyst that it basically breaks apart the H-H and O=O bonds, resulting in temporary Ir-H and Ir=O bonds instead. [8]

The reason these bonds are temporary can be explained in the context of *d*-band theory and the Fermi level of the metal. Basically, the more bonds there are between the iridium and other molecules, the greater the number of electrons will fill the valence band. In a *d*-block metal such as iridium, the electrons in this valence band can easily transfer to the conductance band of the metal. [10] [11] In other words, the electrons can transfer from the temporary Ir-H and Ir-O bonds into the surface of the iridium, breaking the bonds and resulting in hydrogen and oxygen ions in solution with the rest of the gas flow (containing H_2, O_2, and N_2). These ions can now react with the hydrogen and oxygen molecules, forming a radical OH pool which then readily propagates the reaction. [12] The difference between this catalyzed reaction pathway and the uncatalyzed one is that of the initiating reaction; the formation of hydrogen and oxygen ions requires a very large activation energy and will not readily occur at standard temperatures and pressures. [13]

1.1.2 Chemical Equilibrium Analysis and Rocket Equations

NASA's Chemical Equilibrium Analysis (CEA RUN) program is a very powerful tool developed over the past six decades. CEA relies upon iterative minimization of Gibbs free energy of the chemicals in the reaction to drive that reaction to equilibrium. To obtain the chemical equilibrium compositions the program requires two thermodynamic state functions, which allow all others to be determined. This procedure can be used to calculate theoretical rocket performance for a finite- or infinite-area combustion chamber by detailing four primary locations for the flow, as depicted in Fig. 1.6.[14]

This work makes use of NASA CEA's Finite Area Combustor (FAC) procedure. Advancing the flow along each stage of the rocket shown in Fig. 1.6 (injector, combustor, throat, exit) relies upon basic 1-dimensional assumptions for the conservation equations in Eqs. (1.1),

$$\rho_1 A_1 u_1 = \rho_2 A_2 u_2, \tag{1.1a}$$

$$P_1 + \rho_1 u_1^2 = P_2 + \rho_2 u_2^2, \tag{1.1b}$$

$$h_1 + \frac{1}{2}u_1^2 - c_p T_1 = h_2 + \frac{1}{2}u_2^2 - c_p T_2, \tag{1.1c}$$

The CEA RUN program also assumes zero velocity at the combustion chamber inlet; complete combustion; adiabatic combustion; isentropic expansion in the nozzle; homogenous mixing; ideal gas law; and zero temperature and velocity lags between condensed and gaseous species. Combustion in the finite-area chamber is assumed to be a nonisentropic, irreversible process; as energy is released from combustion, the entropy of the system increases and the pressure decreases proportionally.

The injector conditions are provided by the user; two thermodynamic states are specified, usually chamber pressure and reaction enthalpy, whereupon the enthalpy is calculated by the user-assigned chemical composition of the mixture. The combustor contraction ratio $\frac{A_c}{A_t}$ is also specified. The following equations are relevant in both NASA-CEA's solution to a FAC and analysis of experimental data taken for on the Tridyne microthruster.

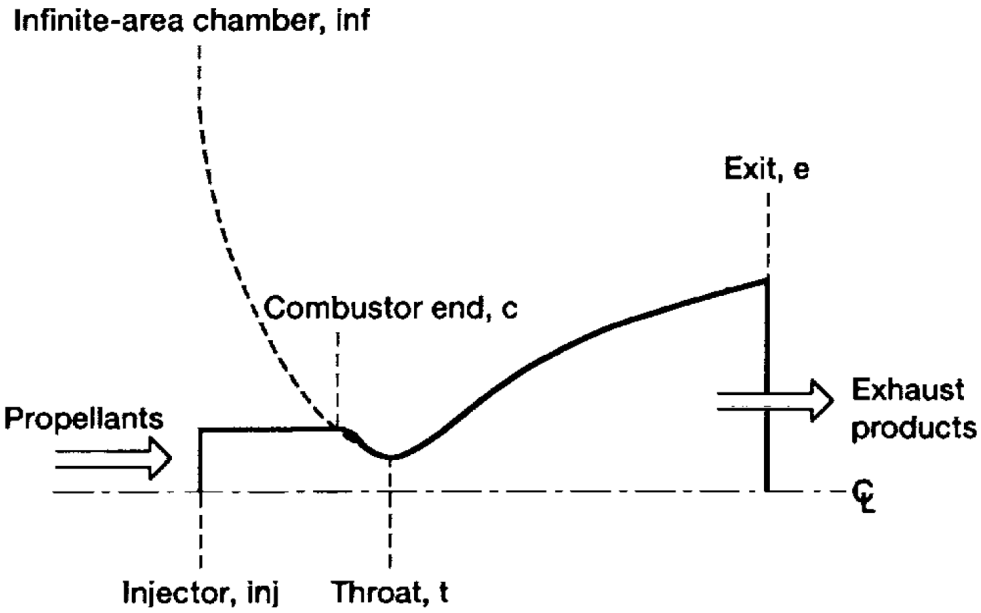

Figure 1.6: Schematics of rocket combustion chamber cross sections used in NASA CEA's theoretical rocket performance estimation. [14]

Flow Velocity By assuming adiabatic, inviscid flow, Eq. (1.1c) results in the expression for exit velocity u_e in Eq. (1.2):

$$u_e = \sqrt{2(h_c - h_e)} \tag{1.2}$$

Force By relating the conservation of momentum and mass in Eqs. (1.1b) and (1.1a) with Newton's second law $F = \frac{\mathrm{d}}{\mathrm{d}t}\Big(mv\Big)$, the net external force F is derived where $\dot{m}$ represents mass flow rate and P_a represents the free stream or atmospheric pressure. In NASA CEA, the exit pressure is set equal to the ambient pressure and the net change in momentum reduces to Eq. (1.3).

$$\begin{aligned} F &= \dot{m}u_e + \Big(P_e - P_a\Big)A_e \\ F &= \dot{m}u_e \end{aligned} \tag{1.3}$$

Specific and Total Impulse The specific impulse, I_{sp}, is a measure of how effectively a rocket uses its propellant and is, by definition, the total change in momentum delivered per unit of propellant weight consumed. Eq. (1.4) is derived from Eq. (1.3), where g_0 represents the gravitational acceleration constant.

$$I_{sp} = \frac{F}{\dot{m} g_0}$$
$$I_{sp} = \frac{u_e}{g_0} \tag{1.4}$$

The total impulse in Eq. (1.5) is another useful metric, representing the maximum momentum a given engine and fuel supply can impart on a system.

$$I_{tot} = g_0 I_{sp} m_p \tag{1.5}$$

Mach Number, Isentropic Relations and Mass Flow Rate The Mach number, $\mathcal{M}$, is the ratio of flow speed u to sound speed $a = \sqrt{\gamma R_s T}$ as shown in Eq. (1.6), where R_s represents the specific gas constant and γ the specific heat ratio of the gas.

$$\mathcal{M} = \frac{u}{a} \tag{1.6}$$

The Mach number is a very important parameter and ultimately enables convenient isentropic expansion relations. A brief derivation of these relations follows, starting from the heat capacity ratio γ:

$$\gamma = \frac{c_p}{c_v} = -\frac{dP/P}{dV/V}.$$

For an ideal gas with constant specific heats, γ is constant. We can thus integrate the above expression, [15]

$$\begin{aligned}
\gamma\frac{dV}{V} &= -\frac{dP}{P} \\
\gamma\frac{1}{V}\frac{dV}{dP} &= -\frac{1}{P} \\
\int \gamma\frac{1}{V}\frac{dV}{dP} &= \int -\frac{1}{P} \\
\gamma\ln(V) &= -ln(P) + c \\
ln(P) + \ln(V^{\gamma}) &= c \\
PV^{\gamma} &= c
\end{aligned}$$

where c represents an integration constant. The above isentropic relation can be expanded using the other definition of c_p and c_v, $c_p - c_v = R_s$. This enable the standard isentropic relations for temperature, pressure and volume:

$$\frac{T_2}{T_1} = \Big(\frac{P_2}{P_1}\Big)^{(\frac{\gamma-1}{\gamma})} = \Big(\frac{V_1}{V_2}\Big)^{(\gamma-1)}$$

The stagnation, or total, thermodynamic properties can be defined from the energy equation (Eq. (1.1c)) when flow is stagnated, denoted by the subscript 0, by using the definition of specific enthalpy $dh = c_p dT$.

$$\begin{aligned}
h_0 &= h + \frac{1}{2}u^2 \\
h_0 - h &= \frac{1}{2}u^2 \\
T_0 - T &= \frac{1}{2c_p}u^2 \\
T_0 &= T + \frac{1}{2c_p}u^2
\end{aligned}$$

Making use of the specific heat relations, $\gamma = \frac{c_p}{c_v}$ and $c_p - c_v = R_s$,

$$\begin{aligned}
c_p - c_v &= R_s \\
c_v\Big(\frac{c_p}{c_v} - 1\Big) &= R_s \\
c_v\Big(\gamma - 1\Big) &= R_s
\end{aligned}$$

The stagnation temperature expression can be simplified in terms of Mach number. Recall Mach number $\mathcal{M} = \sqrt{\gamma R_s T}$.

$$\begin{aligned} T_0 &= T + \frac{1}{2\gamma c_v} u^2 \\ &= T + \frac{1}{2\gamma} \frac{\gamma - 1}{R_s} u^2 \\ &= T + \frac{1}{2} \frac{T}{\gamma R_s T} (\gamma - 1) u^2 \\ &= T\Big(1 + \frac{\gamma - 1}{2} \frac{1}{a^2} u^2\Big) \\ T_0 &= T\Big(1 + \frac{\gamma - 1}{2} \mathcal{M}^2\Big) \\ \frac{T}{T_0} &= \Big(1 + \frac{\gamma - 1}{2} \mathcal{M}^2\Big)^{-1} \end{aligned}$$

The expressions for pressure and density in terms of their stagnation properties can be derived in a similar fashion. This is important; for analysis of a rocket engine, the stagnation properties are effectively the combustion chamber properties due to the combustor's relatively large area and small velocity in comparison to the throat and exit. The isentropic flow equations are summarized in Eqs (1.7).

$$\frac{T}{T_0} = \Big(1 + \frac{\gamma - 1}{2} \mathcal{M}^2\Big)^{-1} \tag{1.7a}$$

$$\frac{P}{P_0} = \Big(1 + \frac{\gamma - 1}{2} \mathcal{M}^2\Big)^{\frac{-\gamma}{\gamma - 1}} \tag{1.7b}$$

$$\frac{\rho}{\rho_0} = \Big(1 + \frac{\gamma - 1}{2} \mathcal{M}^2\Big)^{\frac{-1}{\gamma - 1}} \tag{1.7c}$$

Applying Eqs. (1.7) to the conservation of mass in Eq. (1.1a) gives the steady-state mass flow rate,

$$\begin{aligned} \dot{m} &= \rho u A = \frac{P}{T} \frac{uA}{R_s} \\ \dot{m} &= \frac{A P_0}{\sqrt{T_0}} \sqrt{\frac{\gamma}{R_s}} \mathcal{M} \Big(1 + \frac{\gamma - 1}{2} \mathcal{M}^2\Big)^{-\frac{\gamma + 1}{2(\gamma - 1)}} \end{aligned} \tag{1.8}$$

Characteristic Velocity Represented by c^*, the characteristic velocity is a function of the propellant characteristics and combustion chamber design and is often used as a figure of merit in comparing propellant combinations and combustion chamber designs. [15] The characteristic velocity can be defined in two different ways:

$$c^*_{exp} = \frac{P_0 A_t}{\dot{m}} \tag{1.9a}$$

$$c^*_{th} = \frac{\sqrt{\gamma R_s T_0}}{\gamma \sqrt{[2/(\gamma+1)]^{(\gamma+1)/(\gamma-1)}}} \tag{1.9b}$$

Characteristic velocity can be determined from Eq. (1.9a) using measurable experimental data: the chamber pressure P_0 and the mass flow rate $\dot{m}$, along with a known throat diameter. Eq. (1.9b) allows determination of c^* experimentally if chamber temperature is measured, however that relation also provides a straightforward estimate of c^* dependent only on the gas properties: the specific heat ratio γ, the adiabatic flame temperature T_0, and the molecular mass. This latter calculation represents the maximum possible c^*. The c^* efficiency, $\eta_{c^*} = c^*_{exp}/c^*_{th}$, is a direct comparison of the two velocities, and represents the degree of propellant energy release completion in the combustion chamber. [15] The characteristic velocity efficiency will represent one of the major performance metrics for the Tridyne system developed in this effort.

1.2 State-of-the-Art Microthruster Propellants

There are different types of CubeSat thrusters to be chosen based on the application; multiple thrusters may be onboard a single spacecraft for attitude control systems versus (or in addition to) a primary thruster for spacecraft propulsion. Table 1.2 outlines the performance capabilities of conventional propulsion technologies, with chemical propulsion systems delineated by their propellant; for the purposes of this effort, only chemical propulsion options are considered.

Table 1.2: Survey of various satellite propulsion systems and their associated thrust range, I_{sp}, and Technical Readiness Level (TRL).

Energy	**Propellant Type**	**Propellant**	**Thrust**	**Isp**	**TRL**
Chemical	High I_{sp}	ADN	0.1 - 20 N	260	9
		HAN	0.1 - 20 N	270	6
		Hydrazine	0.1 - 400 N	220	9
	Cold Gas	Compressed Gas	10 mN - 10 N	77	9
		Saturated Liquid	10 mN - 10 N	35 (cold) 80 (warm)	9
	Warm Gas	Tridyne	10 mN - 1 N	140	4
Electric	Pulsed Plasma Thrusters		1 - 1300 μN	500 - 3000	8
	Electrospray Propulsion (Colloid, FEEP)		10 - 120 μN	500 - 5000	8
	Hall Effect Thrusters		10 - 50 mN	1000-2000	8
	Ion Thrusters		1 - 10 mN	1000 - 3500	9

1.2.1 High I_{sp} Propellants

These propellants represent the state-of-the-art for microthrusters in terms of maximizing ΔV and I_{tot}. They are stored in their liquid form and must be pressure atomized into a fine spray and mixed with a pressurant gas for injection to the thrust chamber. Gaseous helium is often used as the pressurant for LMP-103S (ADN), and nitrogen for AF-M315E (HAN) and hydrazine. The mixture is passed over a catalyst bed where the propellant blend reacts. The propellant atomization must be sufficiently fine to effectively disperse the propellant over the entire catalyst bed and minimize localized catalyst degradation, which can significantly shorten the life of the thruster.

Hydrazine (N_2H_4) The most commonly used monopropellant, hydrazine is a pumpable monopropellant liquid which can be stored for decades-long space missions. This propellant, when passed over a catalyst bed, rapidly changes state to an energetic, clean gas. The high energy density, simplicity, and extensive flight heritage have ensured this propellant as the monopropellant thruster fuel of choice for four decades. [16] However for microthrusters hydrazine is not ideal due to expensive storage, handling and disposal procedures of the toxic substance, specially when alternative non-toxic propellants offer comparable performance. From the EPA's summary of hydrazine,

> "Symptoms of acute (short-term) exposure to high levels of hydrazine may include irritation of the eyes, nose, and throat, dizziness, headache, nausea, pulmonary edema, seizures, and coma in humans. Acute exposure can also damage the liver, kidneys, and central nervous system in humans. The liquid is corrosive and may produce dermatitis from skin contact in humans and animals. Effects to the lungs, liver, spleen, and thyroid have been reported in animals chronically (long-term) exposed to hydrazine via inhalation. Increased incidences of lung, nasal cavity, and liver tumors have been observed in rodents exposed to hydrazine. EPA has classified hydrazine as a Group B2, probable human carcinogen." [17]

Furthermore, a number of alternative propellants which exhibit non-toxicity, higher flame temperatures, higher I_{sp}, higher density, and lower cost than hydrazine have been developed and qualified on space flights in the past decade.

HAN and ADN are the two leading green propellant alternatives to hydrazine and are traditionally used in their liquid forms in solution with other chemicals. Both have much higher flame temperatures than hydrazine (2200 K versus 1200 K) and thus require more resilient catalysts than the Iridium-Alumina (roughly 30%Ir / 70% Al_2O_3) S-405 catalyst which was designed for hydrazine. Substantial work has been conducted to develop ceramic catalyst carriers which can withstand the high temperature, corrosive environments of alternative propellants. [18] [19] [20] Both HAN- and ADN-based propellants additionally require a preheated catalyst bed of roughly 350 °C to initiate propellant ignition, unlike hydrazine which is spontaneous. [16] [18]

Ammonium Dinitramide (ADN, $H_4N_4O_4$) LMP-103S is the primary ADN-based propellant, selected by the Swedish Space Corporation (SSC) for project PRISMA. [21] The PRISMA mission launched in June 2010 with the primary objective to test autonomous formation flying of two satellites and a secondary objective to test of an ADN thruster, developed by Bradford ECAPS, for the first time in space. The space qualification of the thruster was concluded after roughly 15 months in space and achieved a 32% higher density impulse than the other hydrazine thruster onboard the spacecraft (named "Mango"). [21]

The LMP-103S blend is composed of 63.0 wt% ADN, 18.4 wt% methanol, 4.6 wt% ammonia, and 14.0 wt% water with a flame temperature of 2200 K and an I_{sp} of 261 s. [22]

Hydroxyl Ammonium Nitrate (HAN, $H_4N_2O_4$) AF-M315E is the primary HAN-based propellant, selected by NASA's Green Propellant Infusion Mission (GPIM) to demonstrate a green alternative to hydrazine. The GPIM mission launched to low-Earth orbit (LEO) in July 2019 and will last 13 months, testing the fuel and compatible propulsion system in space for the first time. The thrusters are created by Aerojet Rocketdyne for two

different thrust levels: 1 N and 22 N. [23] [16]

AF-M315E propellant offers a 12% higher I_{sp} (257 vs. 235 sec) and 45% higher density (1.47 vs. 1.00 g per cc) than hydrazine without the toxicity. [16] The particular composition of this blend is not published. The greater density is also associated with a greater viscosity - this can be particularly difficult to accommodate when designing microthrusters, which rely on small flow paths. [24]

Other HAN-based propellants have been developed by Japan, namely SHP163 and HNP225, with SHP163 having been successfully tested in space. This propellant is a liquid propellant composed of 73.6 wt% HAN, 3.9 wt% ammonium nitrate (AN), 16.3 wt% methanol, and 6.2 wt% water. SHP163 has a roughly 8% greater I_{sp} than AF-M315E at 276 s with a flame temperature of 2130 °C. The density is roughly 5% lower at 1.4 g cc. The propellant is used in the 1 N GPRCS thruster produced by Mitsubishi Heavy Industries and was successfully tested onboard the RAPIS-1 spacecraft in February 2019. [25]

1.2.2 Cold Gas Propellants

These systems are simple, inexpensive, and robust. They are not preferred for large ΔV missions like the above high I_{sp} systems, but are used primarily in providing small impulse bits for attitude control and limited orbital maneuvering.

Saturated Liquid These propellants are less complex than the state-of-the-art high I_{sp} propellants. The two-phase propellant is still stored in a liquid phase, however instead of relying on atomization and mixing of the liquid with a gaseous pressurant these propellants automatically convert to a gaseous state (self-pressurized). Saturation-liquid propellants all have relatively low saturation pressures such that when gas is added to the propellant tank at this pressure, it will condense into a liquid form. As the propellant tank valve is opened, the saturated liquid will readily convert to gas in order to maintain equilibrium.

Unlike the high I_{sp} propellants, the two-phase propellants do not require atomization and mixing into a gas or flow over a catalyst bed; their gaseous form is simply expanded

through a converging-diverging nozzle. In some cases this gas may be resistively heated to achieve higher I_{sp} (80 s) than the cold gas case (35 s). The choice of propellant - usually R-236fa, R-134a, SO_2 or Butane - depends on the desired thrust of the system. The thrust in these cases is directly related to the vapor pressure of the propellant, with Butane tending to offer more precise control and the others tending to offer higher ΔV. The fire duration of saturated liquid thrusters tends to be limited due to cooling of the expanding propellant, unless additional power is devoted to resistive heating of the thruster as is common practice. [26] [5]

Compressed gas Compressed cold gas propellants such as nitrogen represent the simplest form of propulsion: a pressurized gas is stored in a fuel tank, allowed to flow with the use of a regulating valve, and is expanded through a converging-diverging nozzle to generate thrust. This design has very few parts and overall leads to one of the most reliable forms of space propulsion which is still being used today, despite other, more complex systems offering higher thrusts and efficiencies.

1.2.3 Warm Gas Propellants

This category is a largely semantic one; propellants are specified as "warm" due to a low flame temperature. In reality the warm-gas Tridyne proposed here has a comparable flame temperature to hydrazine, but much lower achievable ΔV and I_{tot} due to a lower propellant storage density. Some cold gas propellants can be placed in this category as well; sulfur dioxide, for example, has been used in a micro-cavity plasma discharge thruster which ionizes and accelerates the propellant to greatly improve the gas temperature and associated I_{sp}. [27] Other saturated-liquid propellants such as R-236fa rely on resistive heating of the gas to improve performance. [28] The Tridyne mixture is placed in its own warm gas category here as it cannot compete with high I_{sp} propellants such as hydrazine and relies on a different heating mechanism (chemical rather than electrical) than cold gas propellants.

Tridyne Tridyne is nominally 10% hydrogen, 5% oxygen, and 85% nitrogen by volume. This mixture is stored in the gaseous form and thus does not have any chemistry-associated pressure limitations. Tridyne is inert and non-toxic just as with the other cold gas propellants, however the hydrogen and oxygen in the mixture react spontaneously when exposed to a catalyst (typically Iridium or Palladium). This endothermic reaction heats up the bulk nitrogen which then expands out of a converging-diverging nozzle. All of the components of this system are identical to those in compressed gas systems, except for the addition of catalyst just upstream of the nozzle. The chemical reaction tends to heat the mixture by roughly 1100 K, resulting in an almost 2x improvement in I_{sp} as compared to using pure nitrogen (146 s vs. 77 s). This I_{sp} is roughly 4x that of cold refrigerant thrusters (35 s) and 2x that of resistively heated refrigerant thrusters (80 s), the latter of which require additional system power for resistive heating to achieve that I_{sp}. A Tridyne propulsion system can take advantage of this improved I_{sp} and the ability to achieve high pressures to compete with refrigerant systems while offering greater simplicity, stability, safety and fire duration.

Chapter 2

COMPUTER-AIDED ANALYSIS

Usque adea ne

Scire tuum nihil est, nisi te scire hoc sciat alter?

—Persius, *Satires*, I, xxiii.

The central interest of this project's funding source, the Joint Center for Aerospace Technology Innovation (JCATI), is to bolster the Washington State economy. Thus this project should result in a deliverable which will ultimately lead to increased product sales by and job opportunities with the industry partner for this effort, Aerojet Rocketdyne. This leads to the central question: is this proposed Tridyne-based CubeSat propulsion system a worthwhile, competitive product? In this section, the initial design parameter ranges for a Tridyne microthruster are identified and performance estimates are provided.

The initial design parameter ranges were identified using NASA's chemical equilibrium analysis (NASA-CEA) for a range of preheat temperatures and chamber pressures. Theoretical Tridyne performance was estimated for various storage pressures via a basic simulation of pressure's effect on both system and propellant masses. While diminishing returns due to thick-walled pressure vessels occur after a certain point, this rough estimate suggests Tridyne will be still able to compete with leading CubeSat microthrusters.

2.1 NASA-CEA Performance Estimates

A python code was written to automate the creation of .inp files for NASA-CEA, enabling efficient massive simulation of chemical equilibria from the command line. The corresponding .plt files were then organized into a multidimensional NumPy array to study the effect of preheat temperature, chamber pressure, and exit area expansion ratio on design parameters

such as throat diameter, mass flow rate and thrust (see Appendix A.1). The calculated adiabatic flame temperatures were employed in the c^* efficiency calculations.

Aerojet Rocketdyne plans to provide a nozzle with a .023" throat and a 100:1 exit area expansion ratio. The primary benefit of a Tridyne propulsion system is its simplicity, and therefore the pressure should be unregulated and allowed to decrease with time. Fig. 2.1 represents a hypothetical change in thrust and mass flow rate for different chamber pressures and throat diameters using equations (2.1) and the temperatures, pressures, and thrust coefficients output by NASA-CEA. The provided nozzle with a .023" throat should provide 1N of thrust with a 1.0 g/s flow rate for a 300 psig chamber pressure, which is in Aerojet Rocketdyne's requested range. The thrust and mass flow rates are given respectively by:

$$T = A_t c_{f_e} P_c, \tag{2.1a}$$

$$\dot{m} = \frac{A_t P_0}{\sqrt{T_0 R_s}} \Big(\frac{2}{\gamma + 1} \Big)^{\frac{\gamma+1}{2(\gamma+1)}}. \tag{2.1b}$$

The dependence of specific impulse on preheat temperature is demonstrated in Fig. 2.2 for the 100:1 expansion ratio nozzle. The values shown are for a mixture containing 6% H_2, 3% O_2, balance nitrogen. This is the mixture which will be used for laboratory testing due to gas supplier limitations. The I_{sp} for a mixture containing 10% H_2, 5% O_2, balance N_2 was calculated across the same range in Fig. 2.2 and has an identical profile with an increased magnitude by 22 s. As expected, a higher preheat temperature will enable a greater momentum imparted per gram of the expanding propellant. The dependence of flame temperature on preheat temperature is shown in Fig. 2.3 and will be used in Chapter 4 to estimate the maximum characteristic velocity. The decrease of flame temperature at higher preheat temperatures is most likely due to dissociation losses.

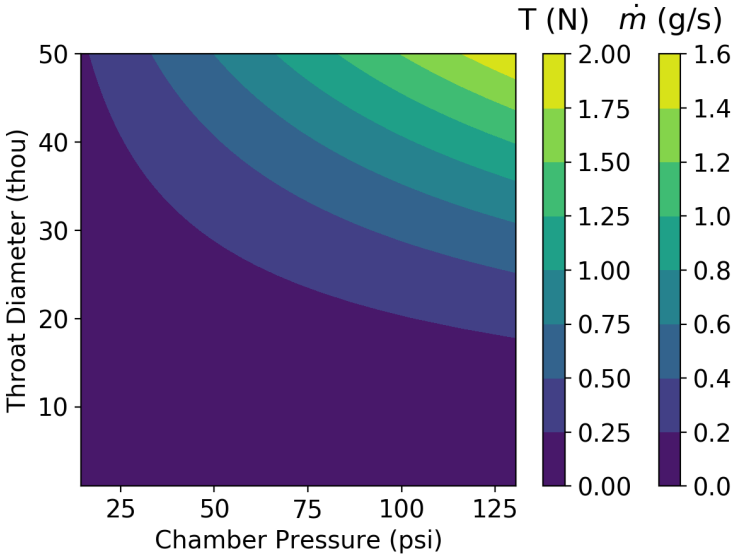

Figure 2.1: Thrust levels for different chamber pressures and throat diameters as calculated by NASA-CEA. Thrust and mass flow rate curves are proportional, with the two colorbars here representing the respective values.

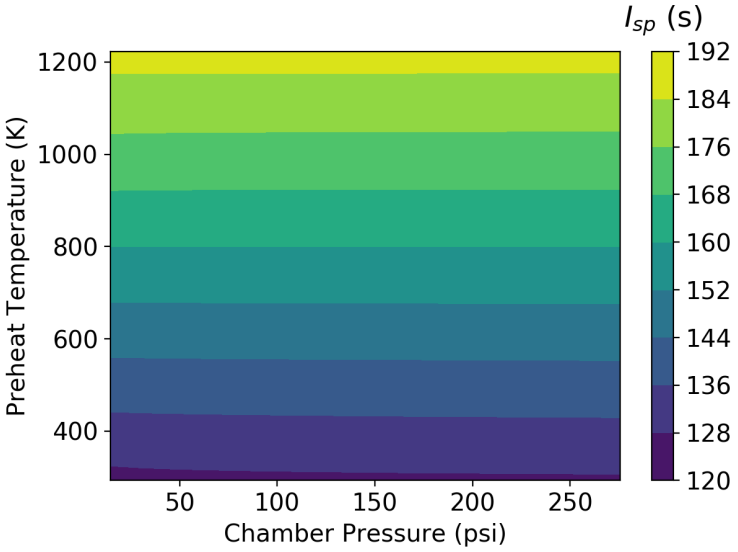

Figure 2.2: NASA-CEA change in I_{sp} for different chamber pressures and preheat temperatures.

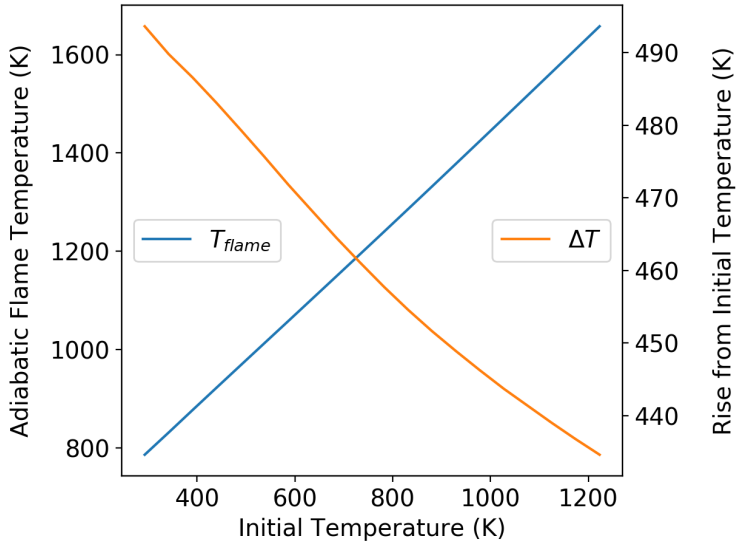

Figure 2.3: Adiabatic flame temperature variation for initial preheat temperature.

2.2 State-of-the-Art Performance Comparison

2.2.1 State-of-the-Art Overview

The competitiveness of Tridyne should be evaluated against state-of-the-art thrusters comparable in complexity and cost. This means looking at low cost, low complexity thrusters which rely on cold or warm gas technology. Most cold gas thrusters favor saturated liquid propellants such as R-236fa over compressed gases such as N_2, due to the much higher propellant storage density and the higher margin of safety from lower storage pressures. Table 2.1 presents thruster specifications using three different saturated liquid propellants representative of current CubeSat low impulse thruster offerings; for consistency one leading manufacturer, VACCO, was chosen to consider these various propulsion systems.

The warm gas SO_2 thruster is in actuality a low-temperature plasma thruster; the gas is ionized via micro-cavity discharge as shown in Fig. 2.4, with an additional preheat of the gas to improve performance. As indicated in Table 1.2 this thruster has a much higher total impulse than the refrigerant thrusters, whose typical plumbing and instrumentation diagram (PID) is shown in Fig. 2.5. The PID for the Tridyne system developed in this

Table 2.1: Characteristics of selected state-of-the-art, low impulse, 1U propulsion systems. [5] [27] [28]

VACCO State-of-the-Art Propulsion Systems	100 mN ADN Liquid	5.4 mN SO_2 Warm Gas	25 mN R236-fa Cold Gas	10 mN R-134a Cold Gas
Number of Thrusters	5	1	4	5
Dry mass (kg)	1.09	0.84	0.96	-
Wet mass (kg)	1.62	-	1.80	1.24
Propellant Density (g/cm^3)	-	1.45	1.37	1.23
Net Thrust (mN)	100	5.4	100	50
Specific Impulse (s)	192	70	54	40
Total Impulse (N-sec)	1036	595	336	250
Total Power (W)	8	15	12	10

effort is displayed in Fig. 2.6. The SO_2 micro-cavity discharge technology will only work for small throats (hence "micro-cavity") and low pressures (vapor pressure at the nominal preheat temperature), however, and is thus limited to lower thrust levels with VACCO/CU-Aerospace's thruster being designed for 5.4 mN. [27] The refrigerant thrusters, however, still rely on electricity to resistively heat the propellant - both for the purposes of increasing propellant storage pressure (and thus performance) and for ensuring only vapor is extracted from the storage tank and expanded out the thrusters. If the R-236fa were not heated, the thrusters would only be able to fire a limited duration before the cooling from the expanding propellant ultimately caused the propellant to condense. [28] [5]

These systems represent the state of the art for 1 mN - 1 N thrusters, and their predictable delivery pressure being self-regulated by the propellant vapor pressure is a strong advantage in comparison to high pressure systems. However they have complexity which is not present in a proposed Tridyne system, such as the reliance on resistive heating and the additional power requirements associated therewith. If comparable performance (ΔV and I_{tot}) can be achieved, a Tridyne system can leverage the other end of this engineering challenge trade-off of self-pressurization versus resistive heating.

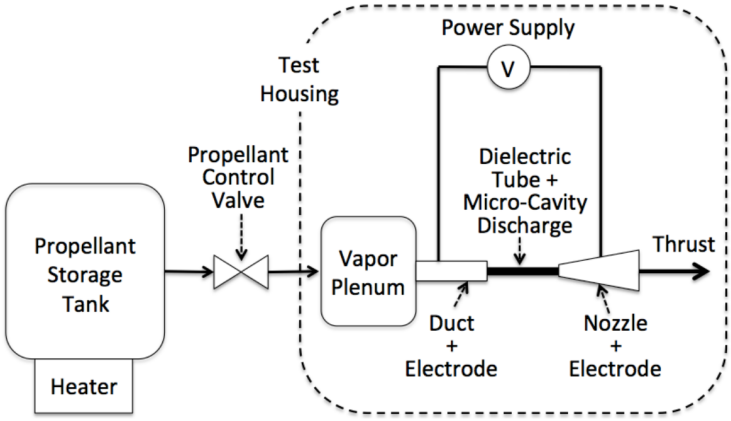

Figure 2.4: Schematic of basic robust prototype PUC [SO_2] thruster system. The components within the dashed region were tested inside the test housing. Image and caption reproduced from [27].

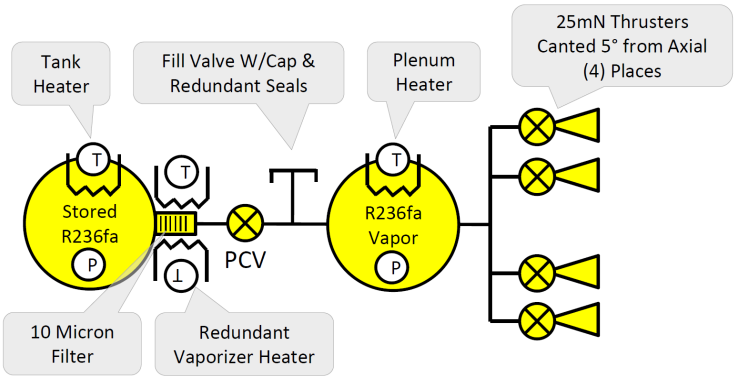

Figure 2.5: Schematic of VACCO and CU Aerospace's R-236fa Standard MicroPropulsion System (Standard MiPS). Image reproduced from [28].

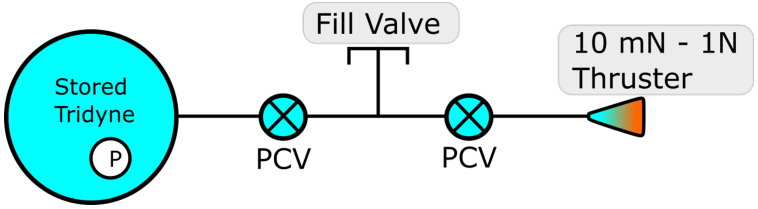

Figure 2.6: Schematic of the Tridyne micropropulsion system developed in this effort.

2.2.2 Design Considerations for Tridyne Systems

The achievable performance of a Tridyne system was estimated here by solving a volume-constrained pressure vessel problem for a range of propellant storage pressures and tank materials. The associated propellant and tank masses allow for calculation of performance metrics such as ΔV and I_{tot} by assuming the ideal I_{sp} from Section 2.1 can be achieved. The classic Tsiolkovsky rocket equation in Equation (2.2),

$$\Delta V = I_{sp}\ g_0\ ln\frac{m_0}{m_0 - m_p} \tag{2.2}$$

indicates performance depends on both I_{sp} and propellant mass, the latter of which can be increased by increasing the storage pressure for a compressed gas. For a saturated liquid system, this storage pressure is limited by the saturation pressure. A performance comparison between a theoretical 1U tridyne system to that of a market leading, commercially available R-236fa 1U microthruster was conducted in Python (see Appendix A.2). An estimated system dry mass (excluding the dry propellant storage tank) was assumed to be 60% of the total reported dry mass in Table 1.2. For a Tridyne system, an estimated 80% of the total 1U CubeSat volume was devoted to the propellant tank. The dry system mass was used in estimating ΔV between the two thrusters, and the volume constraint was used in a volume optimization procedure for a propellant tank. The solution procedure is as follows:

A matrix of cylindrical pressure vessels was initialized in the range of [1.0, 4.8] cm inner radii and [3.0, 7.0] cm lengths. These parameters are annotated in a plotted example of a cylinder shown in Fig. 2.7 and represent a range of possible different shapes which can fit into a 1U (10x10x10 cm) volume. The required thickness for the walls are calculated per standard cylindrical pressure vessel relations in Eqs. (2.3) with a required burst:storage pressure ratio of 2.5. The external volume of the vessel was then calculated.

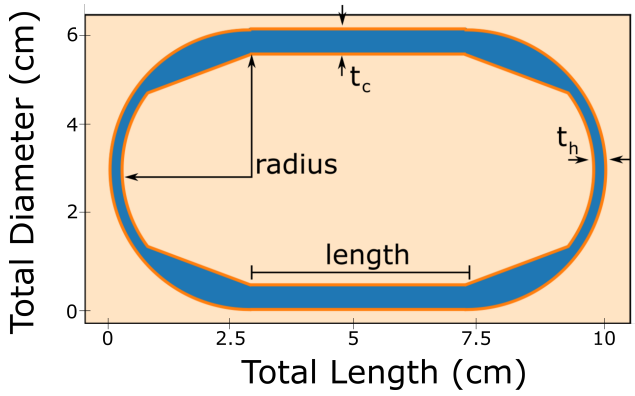

Figure 2.7: Plot of cylindrical pressure vessel with annotated design parameters.

$$t_c = \frac{Pr}{\sigma_y - .6P} \tag{2.3a}$$

$$t_h = \frac{Pr}{2\sigma_y - .2P} \tag{2.3b}$$

$$V_{outer} = \pi(r + t_c)^2 l + \frac{4}{3}\pi(r + t_h)^3 \tag{2.3c}$$

The pressure vessel volume constraint was used as a mask on all solution arrays as illustrated in Fig. 2.8. The optimum point was identified as maximizing both the total propellant mass m_p and the ratio of propellant to total mass $\frac{m_p}{m_t}$ as illustrated in Fig. 2.9, whereby the lightest region of the two overlaid contours represents the optimum design point. It is evident here that a sphere (large radius, small length) is the ideal pressure vessel, which is to be expected.

This pressure vessel volume optimization procedure was repeated over a range of storage pressures and propellant tank materials, with the associated system masses represented in Fig. 2.10. The materials selected are standard alloys which rely on aluminum ($AlSi_{10}Mg$), iron (316 stainless steel), and titanium (Ti_6Al_4V) for their strength, with density and yield strength provided by the metal additive manufacturing company *materialise*. [29] In actuality, the pressure vessel which has been designed for additive manufacturing by Aerojet Rocketdyne is a cubic rather than cylindrical shape - this represents a limitation of the results

here, however for a high level overview the methods employed herein are still sufficient. The variation of m_p to m_t as shown in Fig. 2.8 for different cylindrical aspect ratios is minimal (4% difference in $m_p/(m_p + m_t)$ at most).

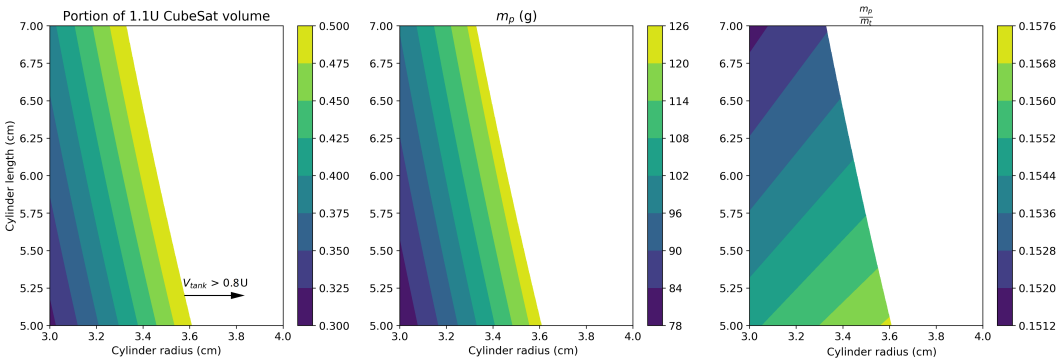

Figure 2.8: Volume-constrained optimization procedure for a hypothetical Tridyne propellant tank at a given pressure.

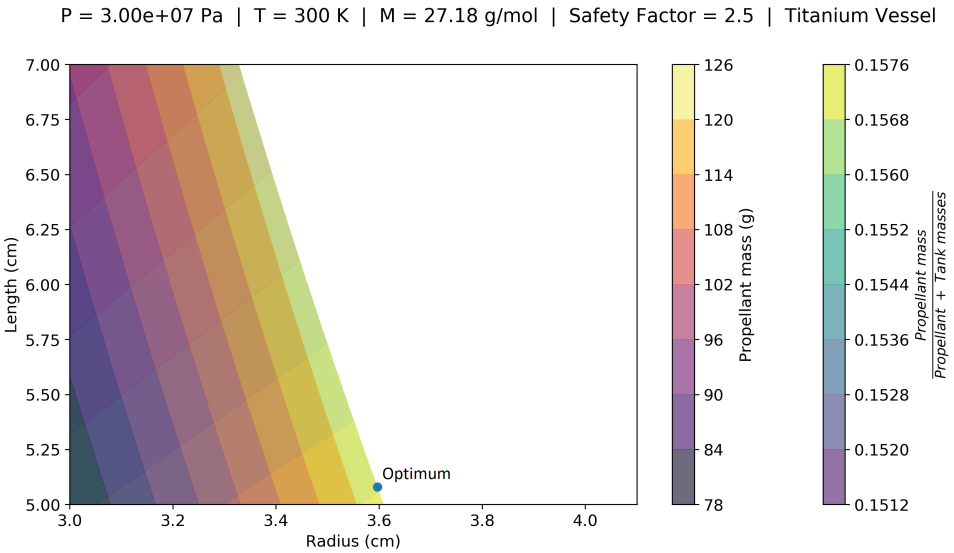

Figure 2.9: Volume-constrained optimum design point for a hypothetical Tridyne propellant tank at a given pressure.

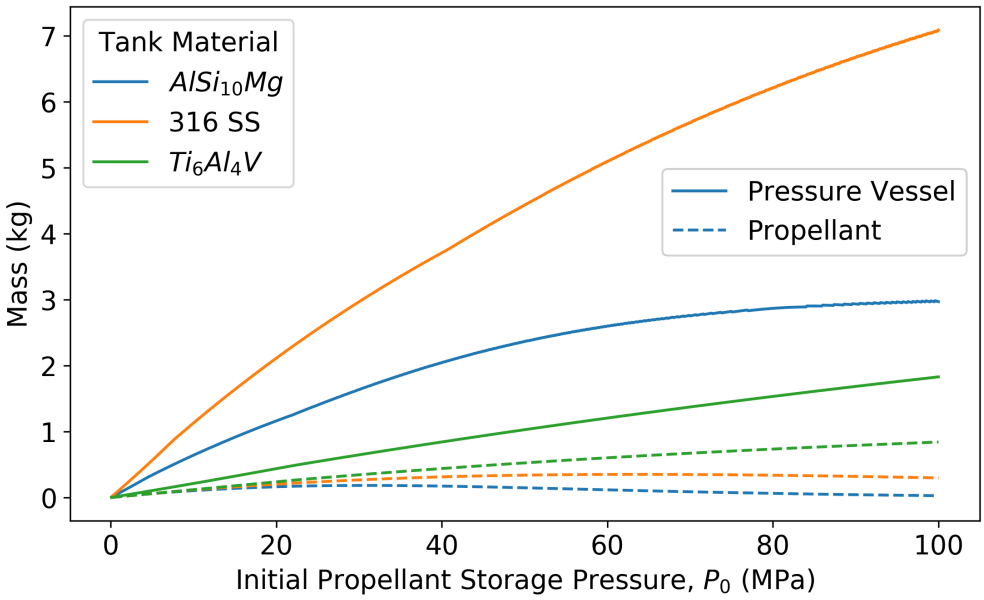

Figure 2.10: System masses for various propellant storage pressures and tank materials for a hypothetical 1U Tridyne propulsion system.

The total impulse and achievable ΔV were then calculated per Equations (1.5) and (2.2), relying on the theoretical specific impulse of 146 s for a nominal Tridyne mixture (10% H_2, 5% O_2, 85% N_2) calculated from NASA-CEA. The results are displayed in Fig. 2.11 with reference points included for the VACCO Standard MiPS. [28] A trade-off with system mass occurs as pressure increases due to increasing pressure vessel mass; Aluminum should not be used at pressures above 25 MPa (3.6 kpsi) and stainless steel above 60 MPa (8.7 kpsi). To be competitive with the state-of-the-art, titanium pressure vessels should be used. This will enable a Tridyne propulsion system to take full advantage of its main strength: being a compressible gas. With a high pressure Tridyne system relying on an additively manufactured tank, the achievable ΔV and I_{tot} can more than double the performance of conventional cold gas thrusters and can even be greater than low-temperature micro-cavity discharge SO_2 plasma thrusters.

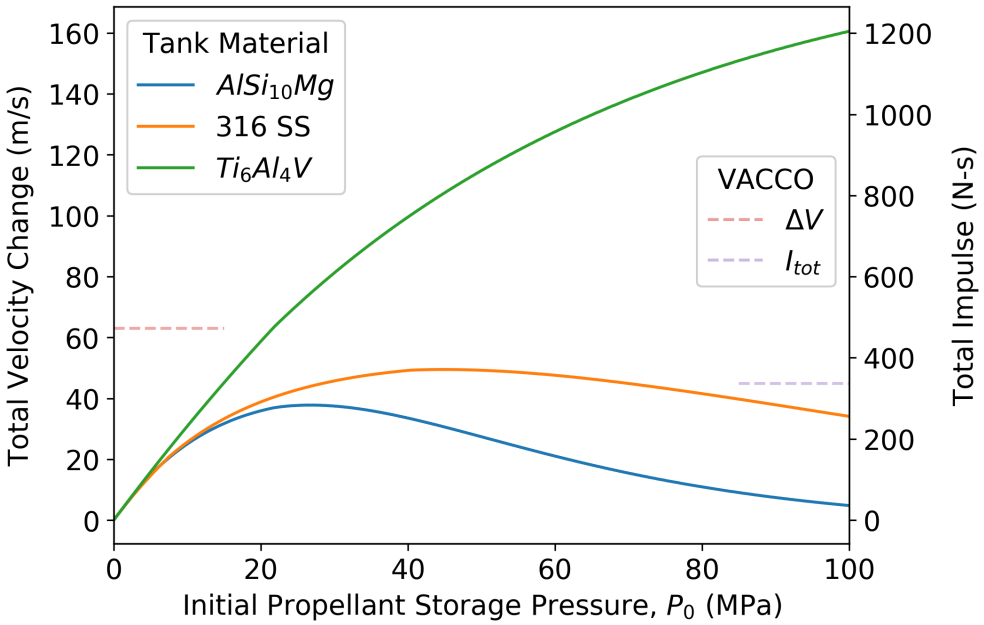

Figure 2.11: Total impulse and ΔV for various propellant storage pressures for a hypothetical 1U Tridyne propulsion system. The curves represent both ΔV (left y-axis) and I_{tot} (right y-axis). Reference points are included for a VACCO Standard MiPS thruster detailed in Table 1.2. [28]

Table 2.2: Comparison of tridyne and R236-fa propellant properties and performance for 1U propulsion units

Propellant	Isp (s)	Storage Pressure		Density ($\frac{g}{cm^3}$)	ΔV ($\frac{m}{s}$)	I_{tot} (N s)
R-236fa	54	Limited (Sat. Liquid)	460 kPa (70 psi)	1.37	63	340
Tridyne	146	Variable (Gaseous)	10 MPa (1.5 kpsi)	0.112	26	160
			100 MPa (15 kpsi)	1.12	140	840

Table 2.2 demonstrates the benefits of a non-pressure-limited, high I_{sp} propellant such as Tridyne in comparison to a conventional saturated liquid propellant. The achievable ΔV was estimated for a hypothetical 4 kg payload and a dry system mass based on the VACCO Standard MiPS. [28]

A 1U propulsion unit was chosen as the size for in-depth analysis as it represents a mid-range of small CubeSat propulsion unit sizes. The range for a VACCO Standard MiPS is actually offered from 0.4 - 1.4U; the code in Appendix A.2 was run for each case corresponding to VACCO's thruster specifications. The CubeSat structural mass was estimated as 60% of VACCO's reported dry mass for each respective size, and a payload mass for estimating achievable ΔV was estimated as 400% of VACCO's reported dry mass. The associated system masses are compared for the different propulsion unit sizes and storage pressures in Fig. 2.12.

Performance contour plots for storage pressure and CubeSat size are presented in Fig. 2.13 for an aluminum and a titanium tank. The trends are anticipated; larger propulsion units will have greater ΔV and I_{tot}, aluminum has an optimal storage pressure before performance decreases, and titanium offers greater performance. This is evident in Fig. 2.12, where the achievable propellant mass is much higher for titanium than aluminum. This is because the stronger titanium can have thinner walls and thus more internal volume available to the propellant. At very high pressures the aluminum tank walls must be so thick that the increase in propellant density is not sufficient to counteract the decrease in available volume, as is evident in Fig. 2.12.

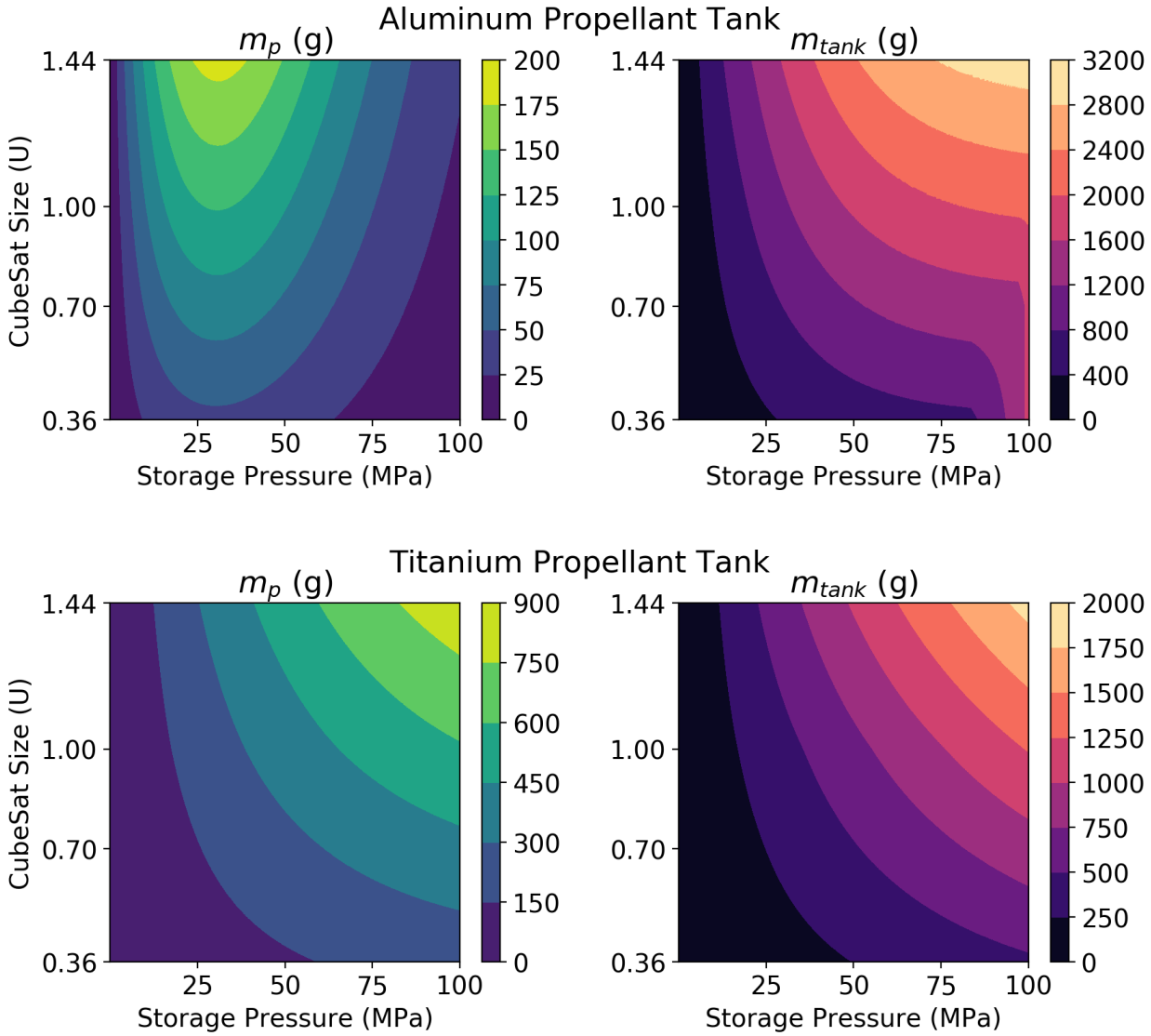

Figure 2.12: Propellant and propellant tank masses for various propellant storage pressures and CubeSat sizes using aluminum and titanium tanks.

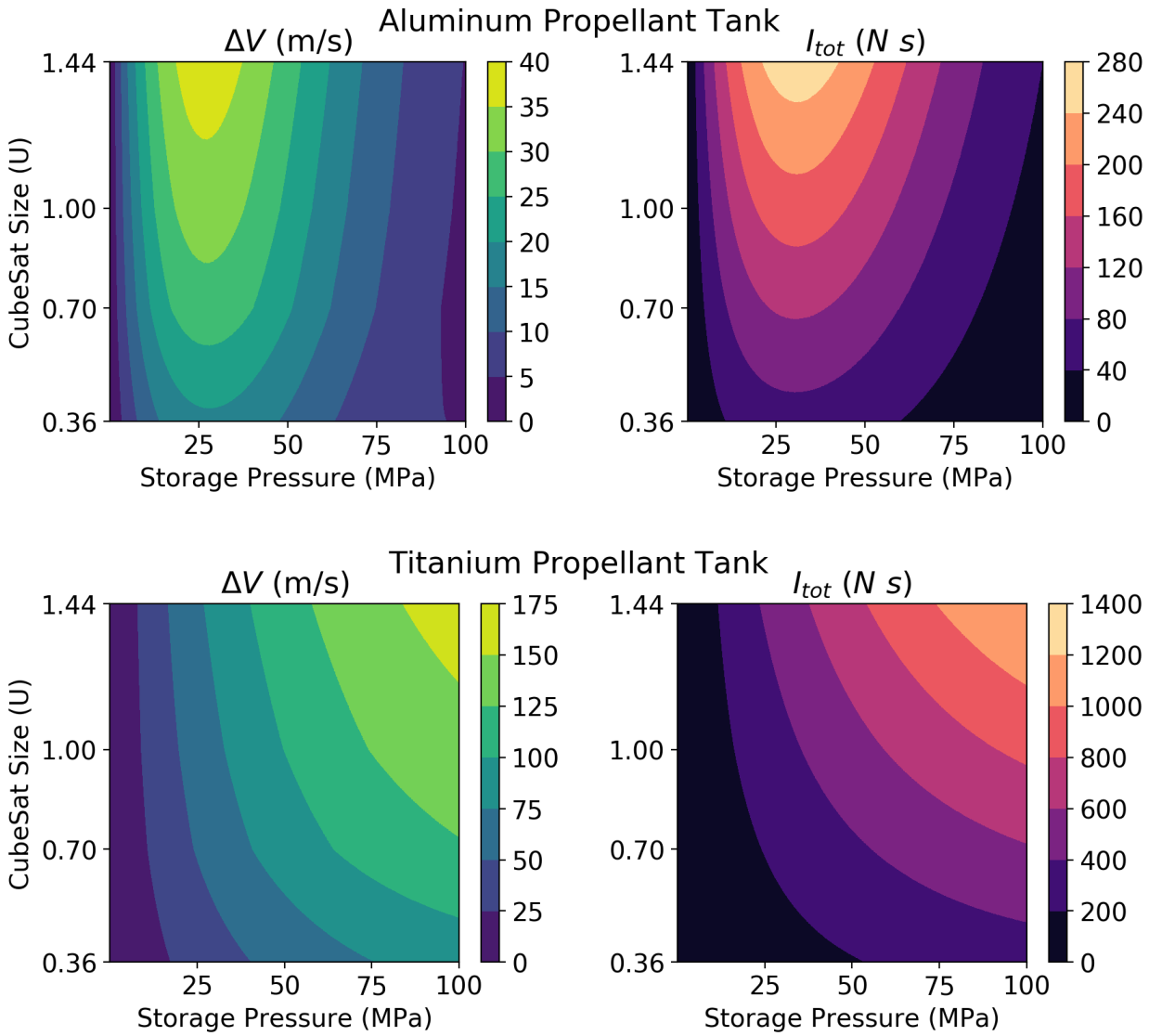

Figure 2.13: Total impulse and ΔV for various propellant storage pressures and CubeSat sizes using aluminum and titanium tanks.

2.3 Cantera Flammability Estimates

The flammability of the Tridyne mixture is a concern to ensure ignition and efficient combustion completion. The flammability was computationally investigated for a range of reactant:diluent concentrations and initial temperatures and pressures. The mix is supposed to be stable at room temperature, but at what temperature will the reaction ignite? Drawing from the background of collision theory in Section 1.1.1, there should exist a temperature ("auto-ignition temperature") for a given pressure and reactant concentration wherein the exothermic chain branching oxidation reactions occur with sufficient frequency to self-accelerate the hydrogen-oxygen reaction mechanism. In other words, the heat release from oxidation must be high enough to overcome the cooling or quenching rates due to the collective gas behavior (recall the Boltzmann distribution) and/or due to the properties of the gas vessel (heat lost due to walls). [30] [31] In this computational investigation, heat transfer effects with the gas vessel are neglected.

A limited investigation of auto-ignition temperature was conducted computationally here and experimentally in Chapter 4 by use of a resistively heated pebble bed to ignite the reaction. The reaction rates and temperature rise for this heated pebble bed case will be compared to those for the S-405 catalyst case in Chapter 4. The computational work was performed in Python using the CANTERA library, which is an open source suite of tools for chemical kinetic, thermodynamic and transport problems (see Appendix A.3). [32] This investigation was limited in that the thermodynamic properties were considered while the vessel effects were neglected; this is not expected to detract from the relevance of these results to reacting with a heated pebble bed, where the vessel temperatures will be hotter than the auto-ignition temperatures with sufficient thermal mass and can be assumed constant.

The basis of the chemical analysis is simple; much like NASA-CEA, Cantera relies on a minimization of Gibbs free energy and, for the $H_2 - O_2 - N_2$ gas mixture, a library of reaction mechanisms provided from [33]. An IdealGasReactor() object was initialized in Cantera with a starting temperature, pressure and reactant concentration. This reactor was

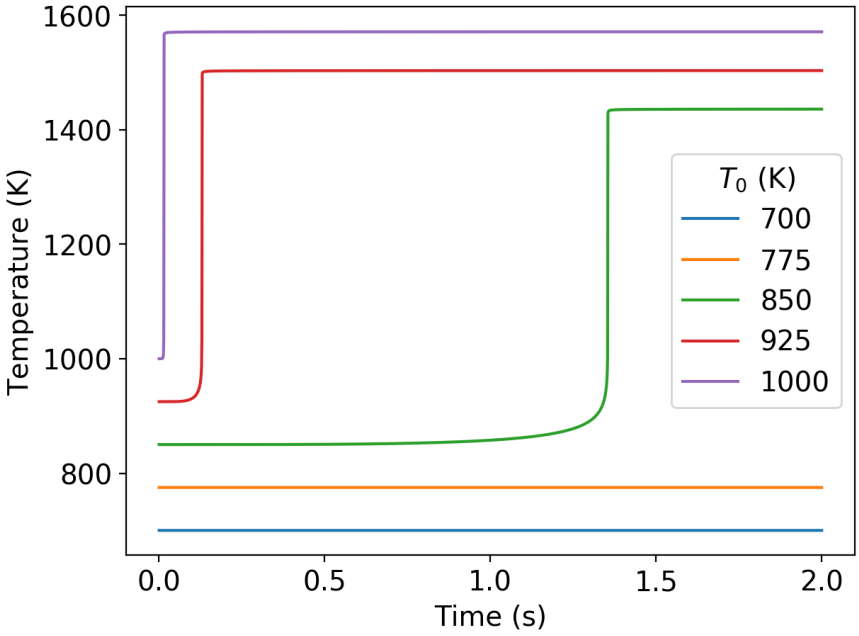

Figure 2.14: Cantera-simulated $H_2 - O_2 - N_2$ Tridyne ignition for different initial temperatures. 100 psi chamber pressure and 6% H_2 3% O_2 balance N_2.

then simulated with discrete time steps. A plot of the temperature vs. time profile for different initial temperatures, a 100 psi chamber pressure, and a 6% H_2 3% O_2 balance N_2 is shown in Fig. 2.14. The auto-ignition time was defined as the time it took for the system temperature to rise to the adiabatic flame temperature and was extracted as a scalar for each simulated initial temperature T_0. In this case, it is clear the Tridyne reaction does not progress for temperatures below 850 K. The 6% H_2 blend was considered here as this was the maximum concentration which could be readily purchased from commercial gas suppliers (Praxair) for benchtop testing. The 10% H_2, 5% O_2, balance N_2 blend is still the nominal Tridyne gas mixture for the flight-weight thruster configuration.

The simulation procedure for auto-ignition temperature was then conducted for a range of reactant concentrations, preheat temperatures and chamber pressures. For the purposes of comparing to experimental values, any thermodynamic combination with ignition time greater than 1 second was considered non-reactive. The auto-ignition time profiles for the

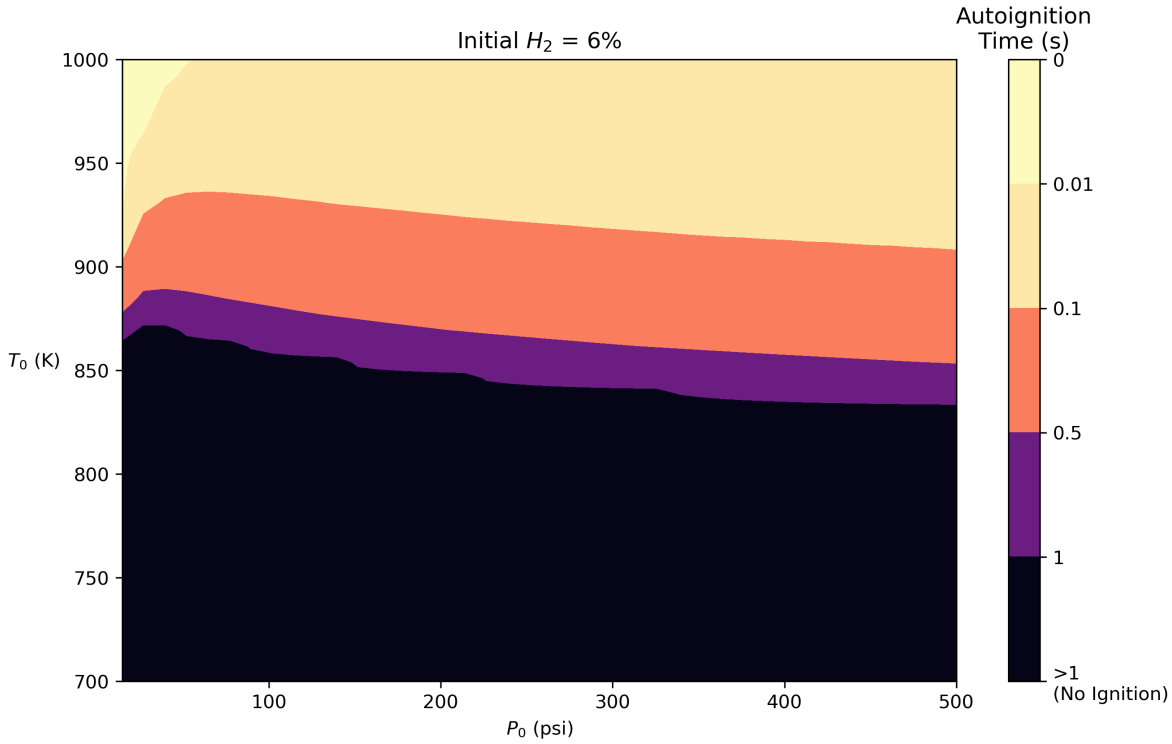

Figure 2.15: Cantera-simulated $H_2 - O_2 - N_2$ reactions' auto-ignition time profile for varying starting temperatures and pressures with 6% H_2 3% O_2 balance N_2.

nominal Tridyne mixture in this experiment is presented in Fig. 2.15 and suggests a minimum preheat temperature of 900 K is required to propagate the $H_2 - O_2$ reaction in the absence of catalyst, with reaction going to completion quicker at temperatures of 1000 K and above.

The variation of auto-ignition timing on pressure is minimal. The adiabatic flame temperature for varying concentrations and preheat temperatures is presented in Fig. 2.16, along with auto-ignition timings. The results are anticipated from Fig. 2.3; the flame temperature does not change significantly with preheat temperature (on the order of 50 K over an 800 K T_0 range), but does increase when the concentration of H_2 is increased. This suggests that a higher combustion performance is achieved with a higher $H_2 - O_2$ reactant concentration in Tridyne, and furthermore that this more energetic blend is still inert at standard temperatures and pressures. However the combustion performance must also be balanced

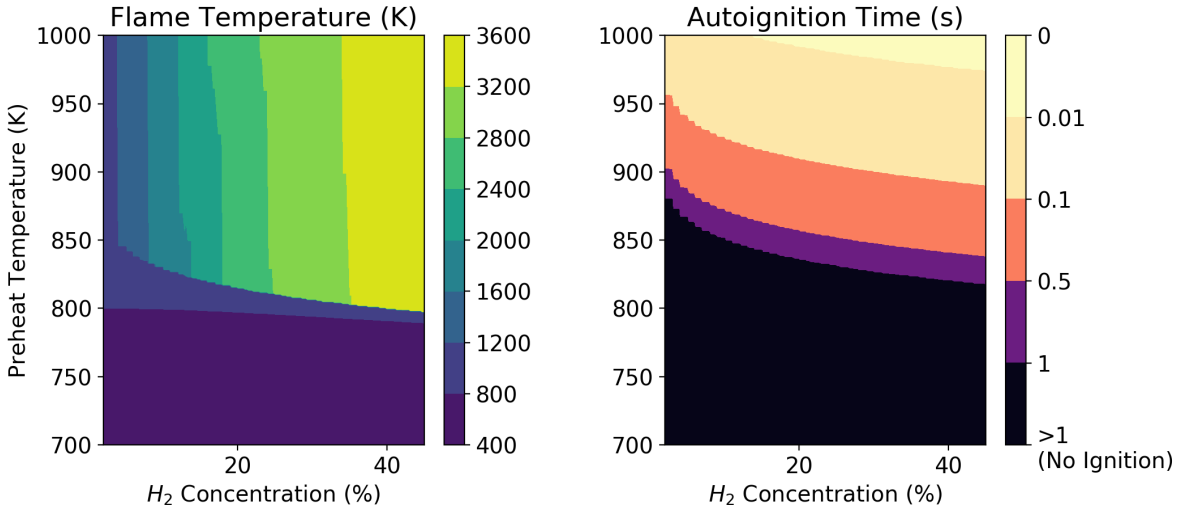

Figure 2.16: Cantera-simulated $H_2 - O_2 - N_2$ reactions' flame temperature and auto-ignition time profiles for varying starting temperatures and H_2 concentrations with a 100 psi chamber pressure. The O_2 concentration is 50% that of H_2 for each case with balance N_2.

with other factors - in the case of using S-405 catalyst, the 10% H_2, 5% O_2, balance N_2 blend is preferred over higher concentrations as the low adiabatic flame temperature of 1400 K minimizes catalyst degradation and thus maximizes thruster lifespan. [4] The $H_2 - O_2$ reactant concentrations in a Tridyne gas blend (and, thus, flame temperature and I_{sp}) can be tailored depending on mission requirements.

Chapter 3

THRUSTER DESIGN AND EXPERIMENTAL SETUP

Non ulla laborum,
O virgo, nova mi facies inopinaque surgit,
Omnia præcepi atque animo mecum ante peregi

—Virgil, *Eclogues*, 10.

3.1 Basic Parameters

Based on the chemical equilibrium analysis detailed in Section 2.1 and the provided flight-weight nozzle by Aerojet Rocketdyne of 0.023", a 200 psi chamber pressure can be expected to result in 1 N of thrust and an associated 0.8 g/s flow rate. However the lab bench-top thruster design for initial performance testing, which is detailed in the following section, relied on convenient, easy-to-use systems and hardware resulting in slightly different operating parameters. Of most important note is that the Tridyne blend employed was of a 6% H_2, 3% O_2, balance N_2 composition, as opposed to the stoichiometric 10% H_2 mix. This lower concentration of reactants was selected due to supply chain limitations (relying on Praxair for gas distribution) and should only affect the maximum flame temperature as explained in Section 2.3.

The S-405 catalyst bed length was designed based on Hydrazine scaling parameters provided in Eckart Schmidt's *Hydrazine and its Derivatives*. [34] The relevant equations are reproduced in Equations (3.1) using English engineering units (lbm/s, in, psia, etc). L represents the catalyst bed length, A_c the chamber cross sectional area, P_0 the chamber pressure, $\dot{m}$ the mass flow rate, a_s the catalyst bed specific surface area, and G the superficial bed loading. A value of 160 in^2/in^3 for a_s was selected from [34].

$$L = 0.3 + \frac{204.5G^{0.7}}{(P_0 a_s)^{0.3}} \tag{3.1a}$$

$$G = \frac{\dot{m}}{A_c} \tag{3.1b}$$

The S-405 catalyst used was 25-30 mesh, which can be approximated as roughly 0.021 inch diameter spheres. In reality these are flakes which can pass through a sieve with this diameter of hole opening. The density of catalyst is roughly 1.76 g/cm^3 (28 g/in^3). [35] Assuming random volumetric packing efficiency of 60%, this length was converted to anticipated required mass of S-405. Table 3.1 presents an overview of the nominal thruster design parameters for both flight-weight and bench-top configurations.

Table 3.1: Flight-weight and bench-top thruster nominal design parameters for a 1 N Tridyne thruster using S-405 Catalyst

System	d_t (in)	d_c (in)	P_0 (psia)	$\dot{m}$ (g/s)	F (N)	$L_{catalyst}$ (in)	$m_{catalyst}$ (g)
Flight-weight	.023	0.4	200	0.8	1	0.84	1.3
Benchtop	.05	0.5	80	1	1	0.78	2.0

The designs for the two systems vary significantly. The CubeSat configuration needs to be as efficient with space as possible due to volume constraints and thus relies on welded fittings, while the bench-top configuration needs to be as user-friendly as possible due to the experimental nature of prototype testing and thus relies on NPT and Swagelok fittings.

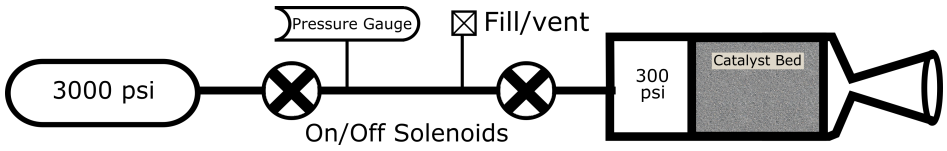

Figure 3.1: Plumbing and instrumentation diagram for the CubeSat Tridyne system.

3.2 CubeSat Configuration

The CubeSat configuration is, for Phase 1 of this project, only considered with CAD to evaluate the feasibility of building such a system. Phase 2 will represent a deeper development into the 1.5U CubeSat configuration including the construction and testing of a physical prototype. The remainder of Phase 1's scope was to build up a laboratory environment where that Phase 2 testing will be possible and to evaluate the Tridyne chemical reaction under varying conditions.

The plumbing and instrumentation diagram (PID) for the CubeSat configuration is displayed in Fig. 3.1. The simplicity of the system is evident, with high pressure solenoid valves allowing gas to flow through the catalyst bed and expand out the nozzle exit. Two solenoid valves were included to allow pulsed-wdth modulation (PWM) of the gas delivery to deliver precise impulse bits. A pressure transducer was included to quantify the quantity of propellant remaining. The fill/vent port was based on a double-end shutoff (DESO) fitting. The computer-aided design (CAD) of the CubeSat configuration is displayed in Fig. 3.2, including the traditional "tuna-can" volume which is allotted to CubeSats in this class.

The solenoids are based on the Parker-Hannifin© Series 9 Miniature Calibrant Valve. This device has a marketed operating pressure of 8.6 MPa (1250 psi) with a 0.030" orifice diameter, however a custom-engineered version of the same device using a smaller orifice diameter can achieve substantially higher pressures. The off-the-shelf version of these calibrant valves however are sufficient for a flight-weight prototype. An alternative which is substantially more expensive (by roughly 150x), but has space heritage and represents the state-of-the-art for high pressure solenoids, is the Marotta MV602L miniature latching valve. These Marotta valves are larger and only one can fit within the 1.5U CubeSat.

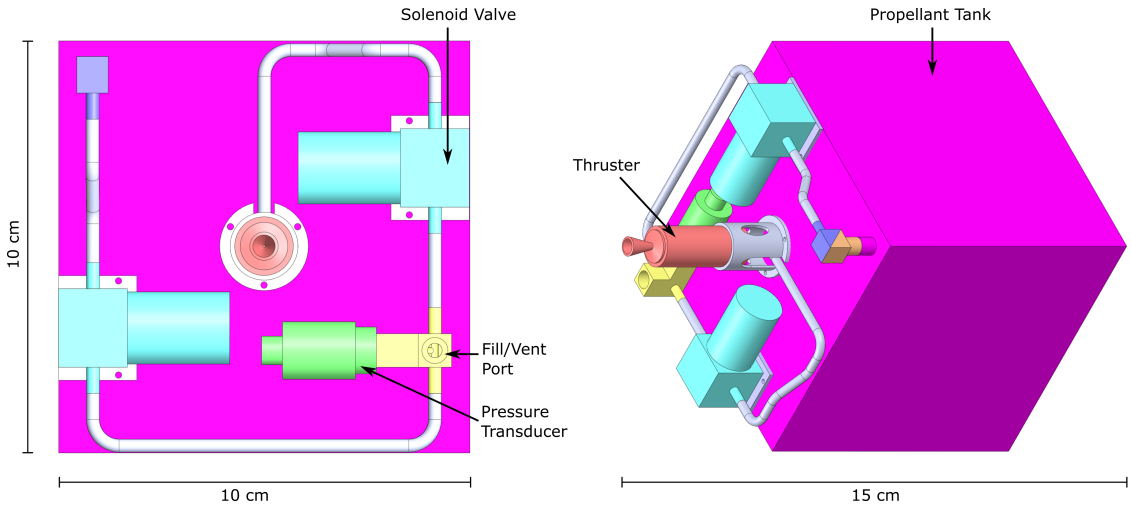

Figure 3.2: CAD of the 1.5U CubeSat Tridyne propulsion unit. Left, 2D overview. Right, isometric view. Primary CubeSat structure and propellant tank details not shown (proprietary Aerojet Rocketdyne information).

The pressure transducer modeled is the GP:50 model 7202 compact flight heritage pressure transducer capable of up to 15 kpsi. The fill/vent port is based on a double-end shutoff (DESO) fitting from Swagelok, model SS-QM2-D-200. These two components will be connected together in a custom fitting which welds to a T-union in the main supply line between the two solenoid valves.

The propulsion unit was designed such that all tubing can be welded; this requires a minimum of 0.25" tube stubs on both sides of tubing being welded together, along with 0.25" minimum bend radii for the 1/8" tubing. The weld at the propellant tank will be performed last with the geometry designed to offer sufficient clearance for the orbital weld head being used (0.4"). A thermal standoff on the thruster secures it to the propellant tank with tack welds to the surface of the pressure tank.

The propellant tank was additively manufactured with a roughly square form factor capable of storing high pressure gas. A bimetallic fitting is shown in Fig. 3.2 to transition from the tank material (Aluminum for prototype, Titanium for flight-weight design) to the tubing material (316 stainless steel).

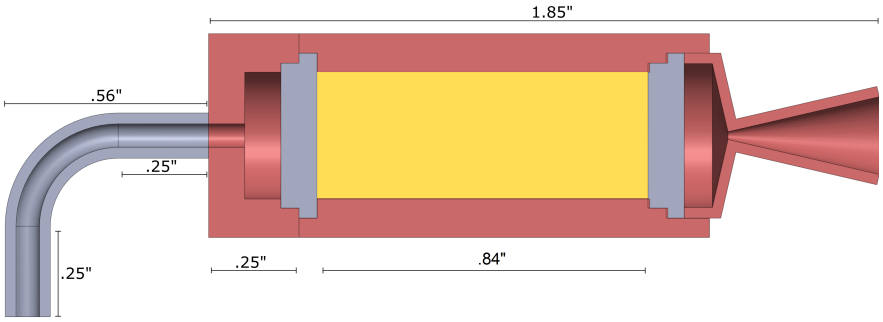

Figure 3.3: CAD of the flight-weight Tridyne thruster with annotated dimensions. Inside the thruster, yellow represents the S-405 catalyst and gray represents the catalyst bed-plates.

The thruster along with its dimensions are displayed in Fig. 3.3. The majority of this length will fit within the standard 1.6" (40 mm) tuna-can length for CubeSats with the remaining height being comparable to the required height for the fill/vent ports and solenoid valves. [37]

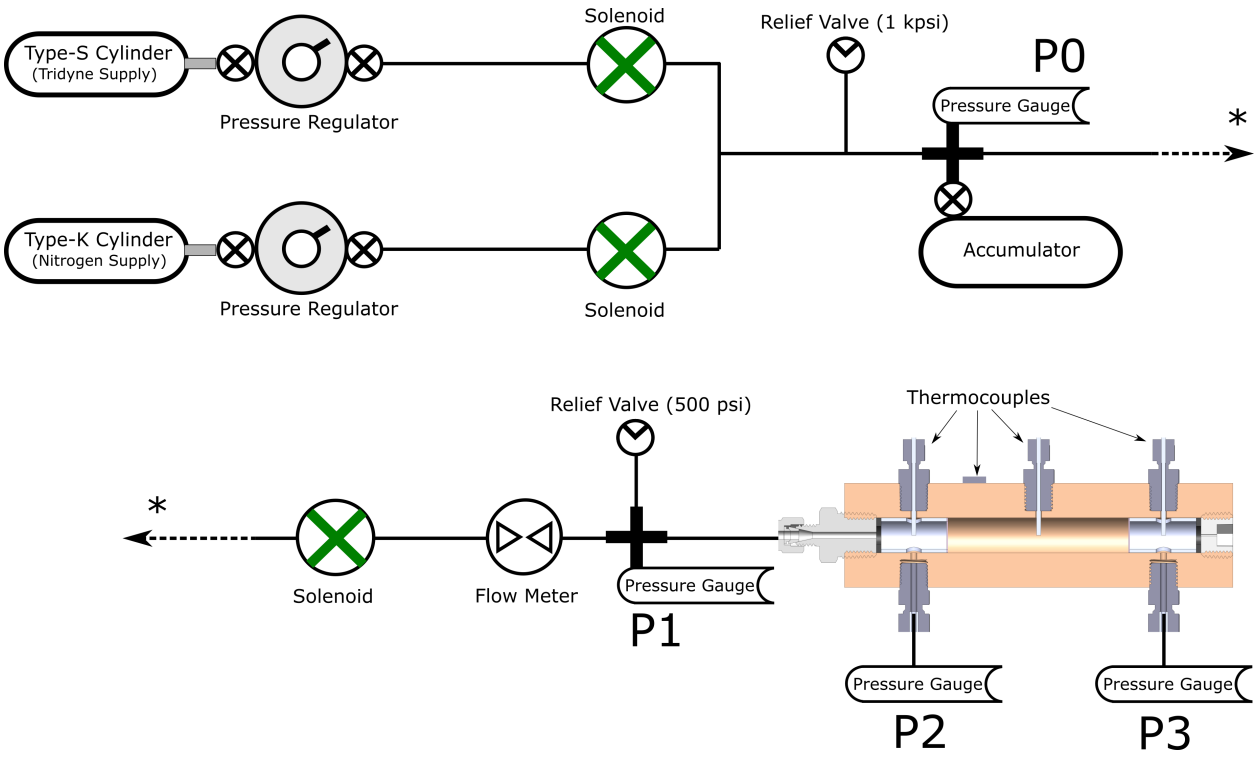

Figure 3.4: Plumbing and instrumentation diagram for the bench-top Tridyne system.

3.3 Bench-top Thruster

3.3.1 Nominal Thruster Design

The bench-top thruster was designed to support a wide range of preliminary testing on the Tridyne thruster. The Tridyne reaction was initially initiated by raising the temperature of the gas as explained in Section 1.1.1 and Section 2.3. This was performed via a heated pebble bed. The Tridyne reaction was then initiated for the S-405 catalyst at various preheat temperatures. The essential measurements for thruster performance include mass flow rate, temperature, and pressure. The complete PID of the bench-top system is detailed in Fig. 3.4. An annotated view of the thruster is presented in Fig. 3.5.

The temperature measurements were recorded at the inlet, center of catalyst bed, and exit of catalyst bed (but still inside the thruster) using OMEGA TJ-36-CAXL-116E-6 ther-

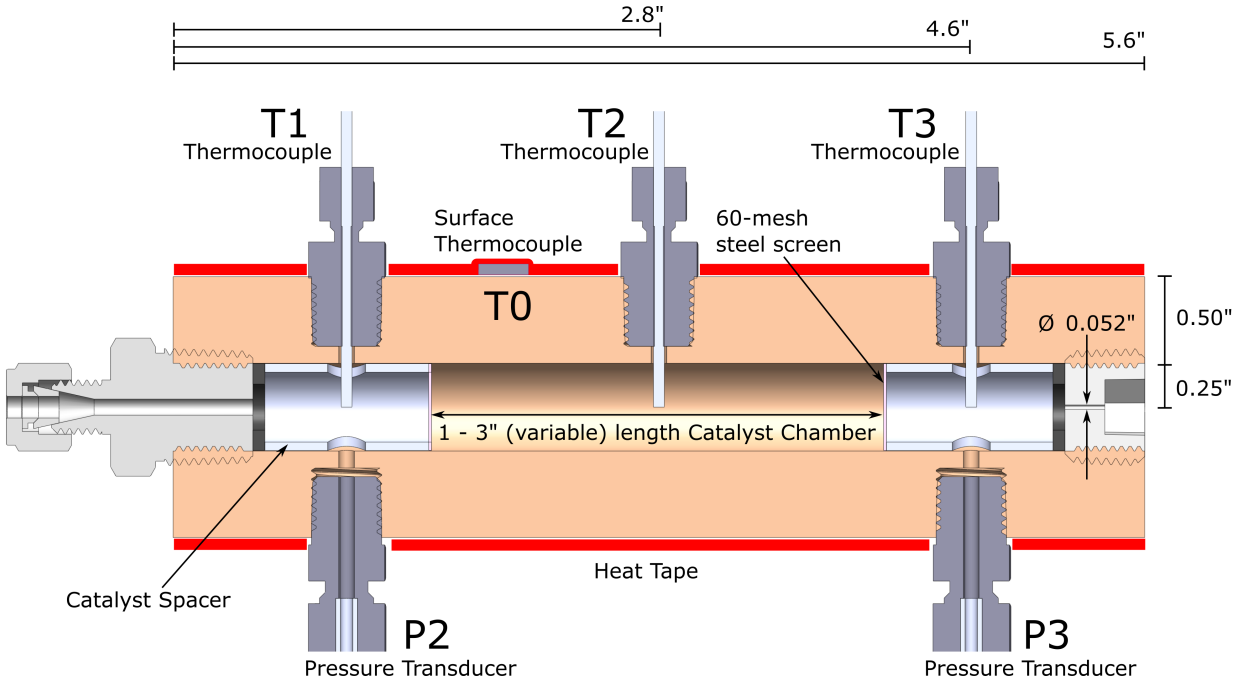

Figure 3.5: Bench-top thruster CAD with annotated components and dimensions.

mocouples rated to 1040 ^oC. A surface-mounted thermocouple was also used (not shown in Fig. 3.5). The pressure measurements were recorded at the inlet and exit using OMEGA PX309-500G5V pressure transducers. The mass flow measurements were recorded by an OMEGA FMA5500a mass flow controller with a range of 0 - 50 Standard Liters per Minute (SLM). Five feet of 1/8" 316 stainless steel tubing connect the mass flow meter to the inlet of the thruster.

The thrust chamber was designed to allow for easy variability of the catalyst type and catalyst bed length, which was accomplished by means of the 316 stainless steel "catalyst spacer" as annotated in Fig. 3.5. This is essentially an extra-long washer with access ports included for the diagnostics. A 60-mesh wire cloth screen made of 304 stainless steel was fit on the interior end of each spacer, sized to include a tight slip-fit to the inner bore of the thruster. This slip-fit was easily installed or removed by sliding a rod through the thruster until the ports on the catalyst spacers aligned with the diagnostic ports. A range of catalyst spacer lengths were created to test a number of catalyst bed lengths, however in reality only

two main lengths were tested: 1" for the S-405 catalyst, and 3" for the steel pebble bed.

Heat tape was required to conduct heated pebble bed testing and heated catalyst bed testing. The OMEGA DHT051020LD heat tape is rated to 760 ^oC and provides 13.1 W/in^2. This was wrapped around the outside of the thruster and then surrounded by insulation.

The pebble bed consists of 1/8" chrome steel balls. A 3" long pebble bed, combined with the nominal chamber pressure test range (20 - 150 psi) and associated mass flow rates, will enable residence time for sufficient heat transfer to the gas to prompt the hydrogen-oxygen reaction. The S-405 catalyst bed length is nominally 0.8" long requiring an estimated 2 grams of catalyst. In practice the catalyst bed came out to be 1.2" long with 6.6 grams of catalyst used; it is possible the density estimate from [35] was outdated and that the random volumetric packing efficiency for small loose flakes is much greater than for spheres. The length difference was due to the removal of washers from the original design and was not a problem; extra catalyst primarily served to add additional pressure drop across the catalyst bed, and at these length scales was negligible.

Lastly, an accumulator bottle was included inline as shown in Fig. 3.4. This bottle has a 500 cm^3 storage volume with an 1800 psig maximum storage pressure. This bottle could used to simulate "blow-down" testing, whereby a high pressure storage vessel is opened to allow flow through the thruster with an orifice limiting the delivery pressure. The blow-down flow regime is the anticipated flow regime for the flight-weight CubeSat unit.

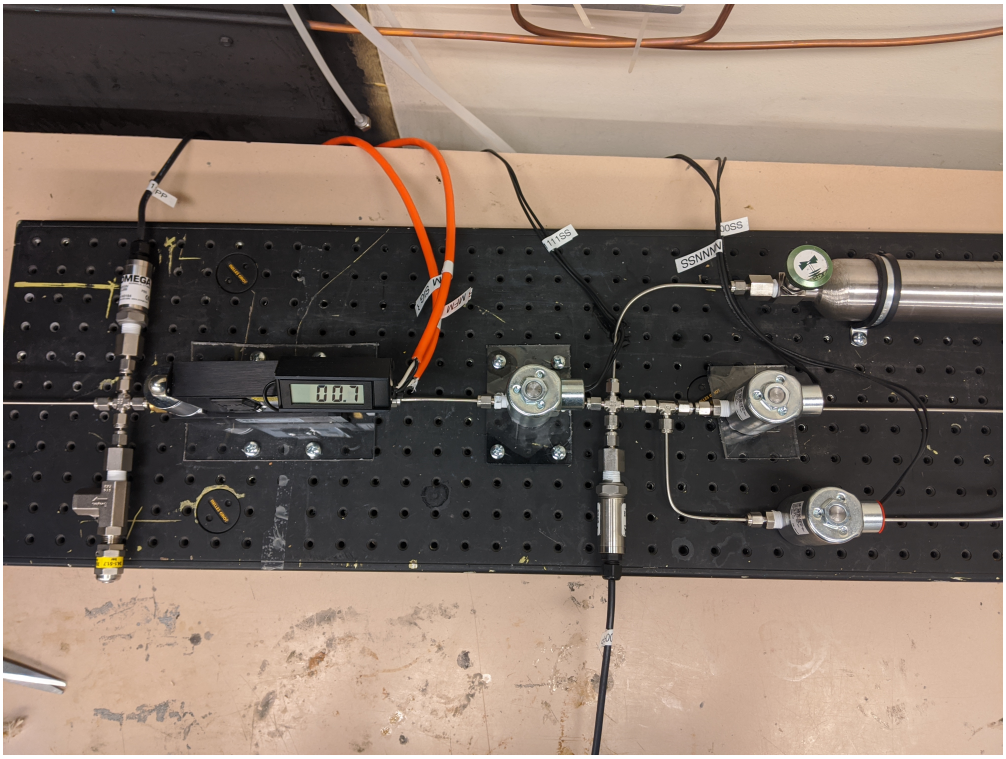

Figure 3.6: Laboratory mass flow delivery system based on the design in Fig. 3.4.

3.3.2 Experimental Setup

The mass-flow-delivery side of the experimental setup detailed in the PID of Fig. 3.4 is pictured in Fig. 3.6. The solenoids, mass flow meter, and accumulator bottle were mounted to the base of an optical board with a grid of 1/4”-20 mounting holes. The mass flow meter used was actually a mass flow controller, however the flow control solenoid was set to be always open using an electrical jumper.

The mass flow delivery connects to the thruster pictured in Fig. 3.7 with 5 feet of 1/8” diameter 316 stainless steel tubing. The thruster is pictured in Fig. 3.7 with 2” thick insulation surrounding it for heated testing. A proportional-integral-derivative controller is located to the lower right and controls the heat tape power with reference to either the catalyst bed thermocouple or the surface thermocouple.

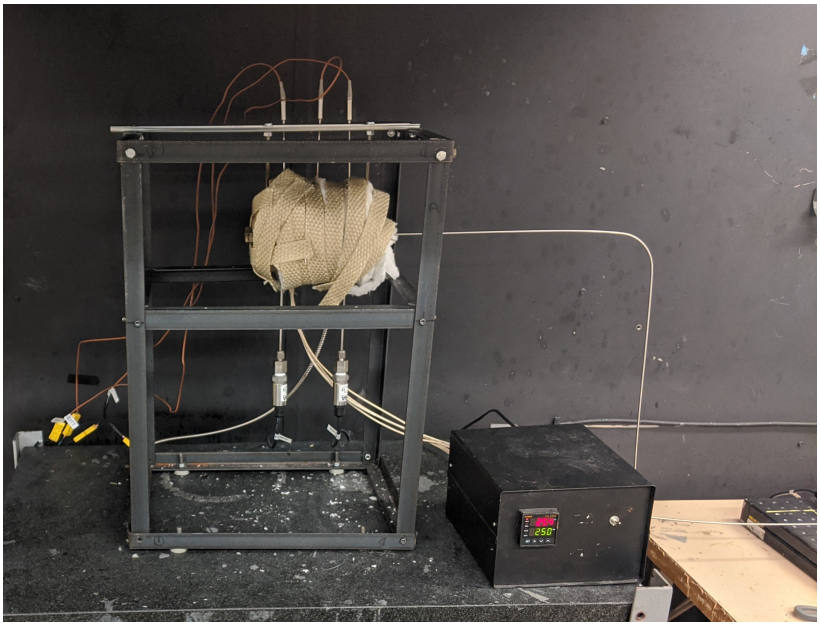

Figure 3.7: Laboratory thruster mount and thruster. The thruster is covered in insulation for heated testing, and the proportional-integral-derivative controller for the heat tape is located to the lower right.

Figure 3.8: Laboratory insulated thruster without heat (left, 20^oC) and with heat (right, $850\ ^oC$). The strong red glow for the heated case is due to black body radiation for hot steel.

Figure 3.9: Laboratory thruster without (left) and with (right) heat tape. The color change in the heat tape is due to one having been used before. The three thermocouples extend from the top of the thruster and the two pressure transducers from the bottom, with an additional thermocouple tapped to the surface.

The insulated thruster without heat ($T_{thruster} = 290$ K) and with heat ($T_{thruster} = 1100$ K) is pictured in Fig. 3.8. The thruster without heat tape and without insulation is pictured in Fig. 3.9.

The power required for all of the diagnostics is detailed in Fig. 3.10. The power supply used was a 24 V, 60 W AC/DC converter supplied by Mean Well Inc. (model IRM-60-24ST). Buck converters manufactured by DROK model LM2596 were used to convert the 24 V power to acceptable voltages of 12 V and 9 V for the mass flow meter and pressure transducers, respectively. The power supply unit used has a 150 mV peak to peak ripple as an artifact from the AC power conversion, but this could be reduced with nicer power supplies. A redesign of the power system would use individual AC/DC converters for the 9 V and 12 V power (rather than buck converters) to minimize noise in the power supply; for the solenoids a noisy signal is okay, however for powering diagnostics that noise will creep into their collected data and need to be filtered out digitally. Passive signal filtering methods were

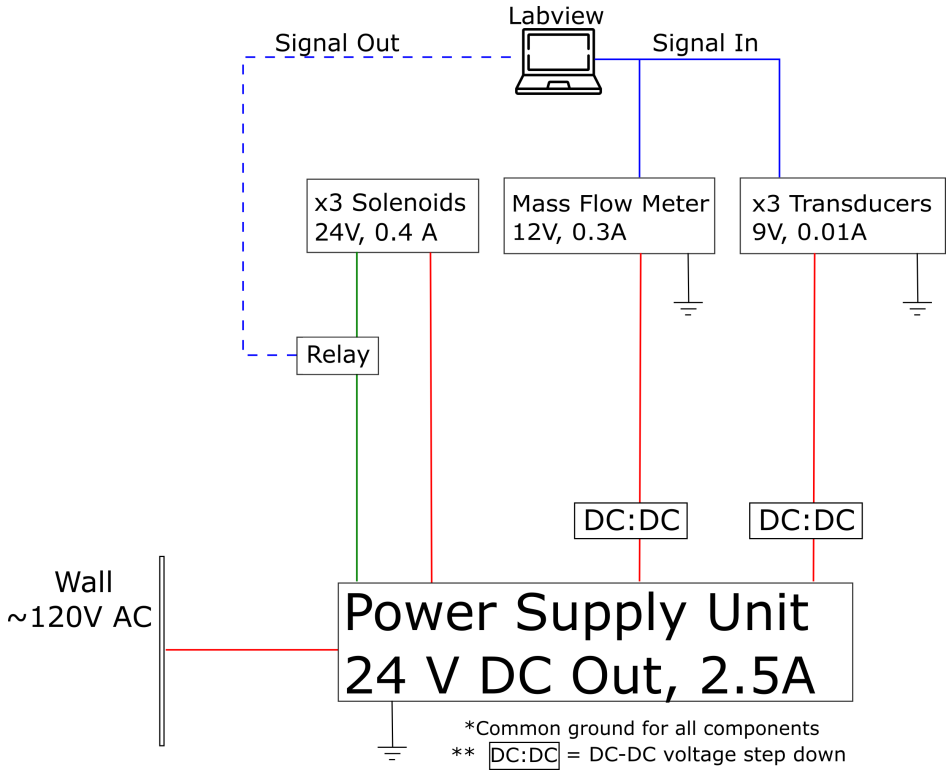

Figure 3.10: Power supply overview for bench-top experiment diagnostics and mass flow delivery.

considered and testing including RC and RLC filters and ultra-low-noise linear low-dropout voltage regulators (TI brand LM350AT and LT1084CT), however in the end a combination of 1 μF bypass capacitors and minimal digital filtering was sufficient to provide clean data.

The power supply was contained within a custom polycarbonate enclosure and is pictured in Fig. 3.11, along with a laptop running LabVIEW and the data acquisition unit. A National Instruments brand Compact Data Acquisition system, the NI cDAQ 9178, was used in conjunction with three modules: the NI-9215 voltage input module for the pressure transducer and mass flow meter measurements, which output their signal in the range of 0 - 5 V; the NI-9482 electromechanical relay module, which allows switching of solenoids for the mass flow delivery system from LabVIEW; and the NI-9212 temperature input module for the thermocouples.

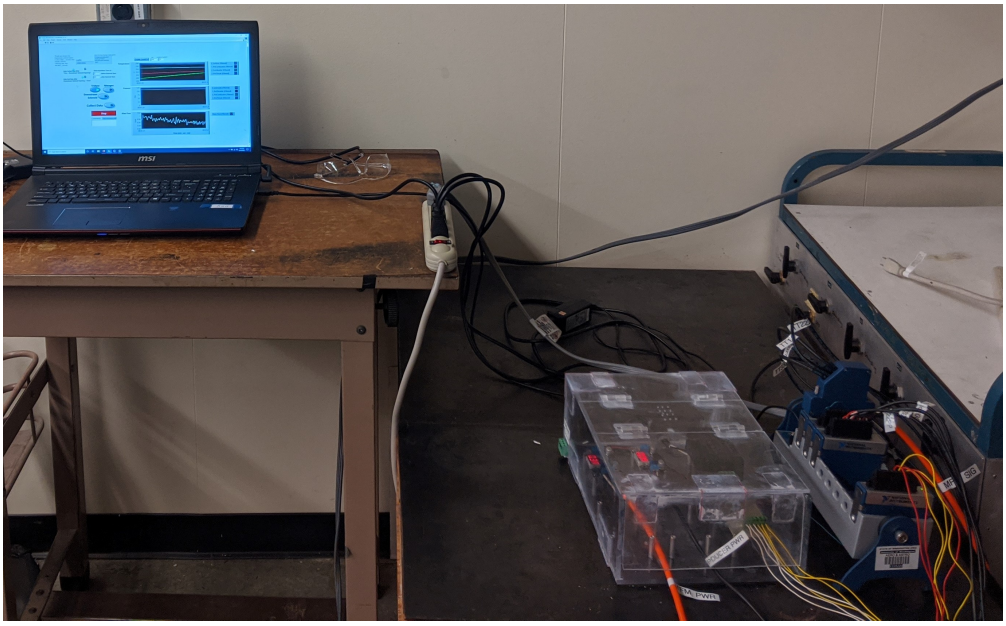

Figure 3.11: Laboratory data acquisition and power management setup.

The LabVIEW graphical user interface (GUI) pictured in Fig. 3.12 controlled and collected data for the experiment. The data acquisition could be set to automatically start and stop based on the mass flow system opening, or every component could be controlled manually. Two solenoids opened flow from either the Tridyne or nitrogen supply bottles and allowed gas entry to the accumulator bottle pictured in Fig. 3.4 if it's valve was open. The "downstream" solenoid then opened flow from this volume through the thruster. The data files were automatically named in a year:month:day:shot format (yymmddsss), stored in a folder for the associated date which was also automatically created. The files were stored in a .csv format containing a time column and associated measurements from four thermocouples, four pressure transducers, and one mass flow meter. The rate of data collection and number of samples per data collection loop were default set to 200 Hz and 10 samples respectively and could be changed by the user on the front panel.

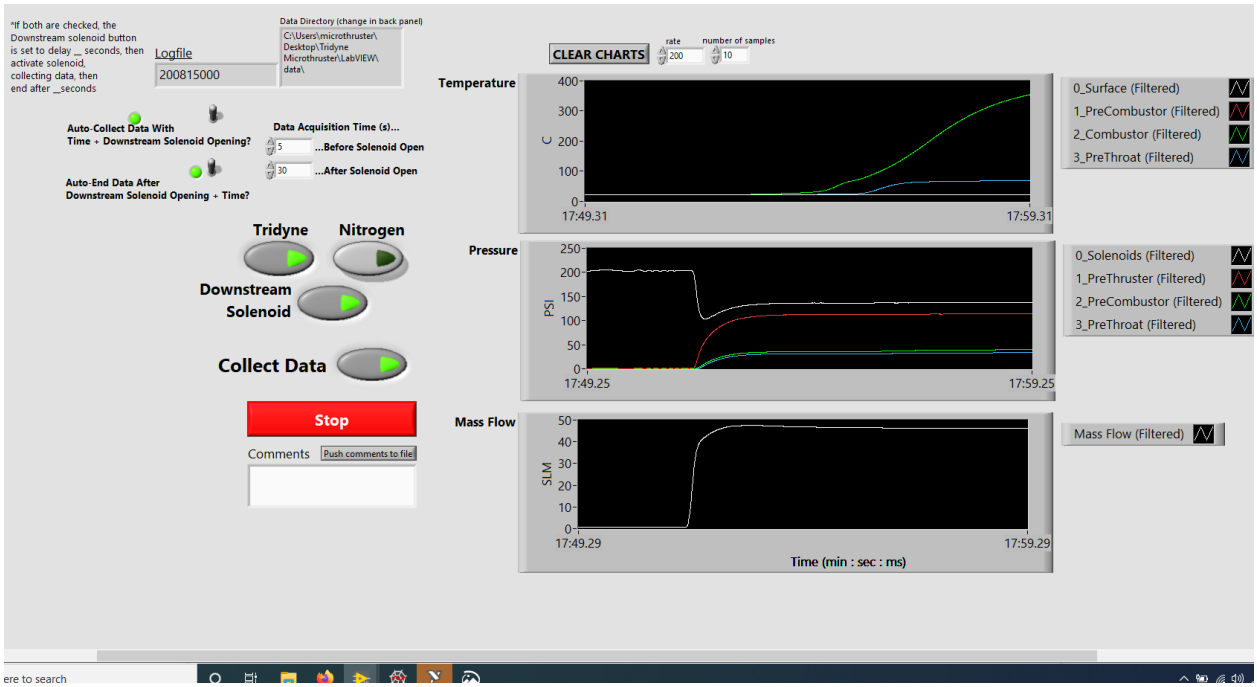

Figure 3.12: LabVIEW graphical user interface to control the bench-top thruster experiment. Back-end of LabVIEW code is available .

Chapter 4

THRUSTER TESTING

Medio de fonte leporum,

Surgit amaro aliquid quod in ipsis floribus angat

—Lucretius, *de rerum natura*, Liber IV.

Two configurations of the bench-top thruster were tested: the first contained a 3" pebble bed comprised of 1/8" diameter chrome steel balls, and the second a 1.2" catalyst bed comprised of 25-mesh S-405 catalyst. Testing for a range of preheat temperatures T_i and chamber pressures P3 (and thus mass flow rates $\dot{m}$) was conducted for four systems: heated pebble bed with nitrogen gas, heated pebble bed with Tridyne gas, room temperature catalyst bed with Tridyne gas, and heated catalyst bed with Tridyne gas.

Heated nitrogen testing was conducted in the pebble bed thruster to approximate the impact of heat transfer from the pebble bed to the gas at high preheat temperatures. Heated pebble bed testing was then conducted to provide a comparison point for the catalyzed Tridyne gas performance. This enabled estimates of required power input to achieve similar performance via resistive heating as compared to a catalyzed reaction. Heated pebble bed testing also validated computational chemical equilibrium analyses of ignition temperature. The S-405 catalyst bed thruster configuration was then tested to evaluate the performance of the Tridyne propellant in the presence of S-405 catalyst at different temperatures and ultimately provide insight on the design of a flight-weight thruster employing the same catalyst.

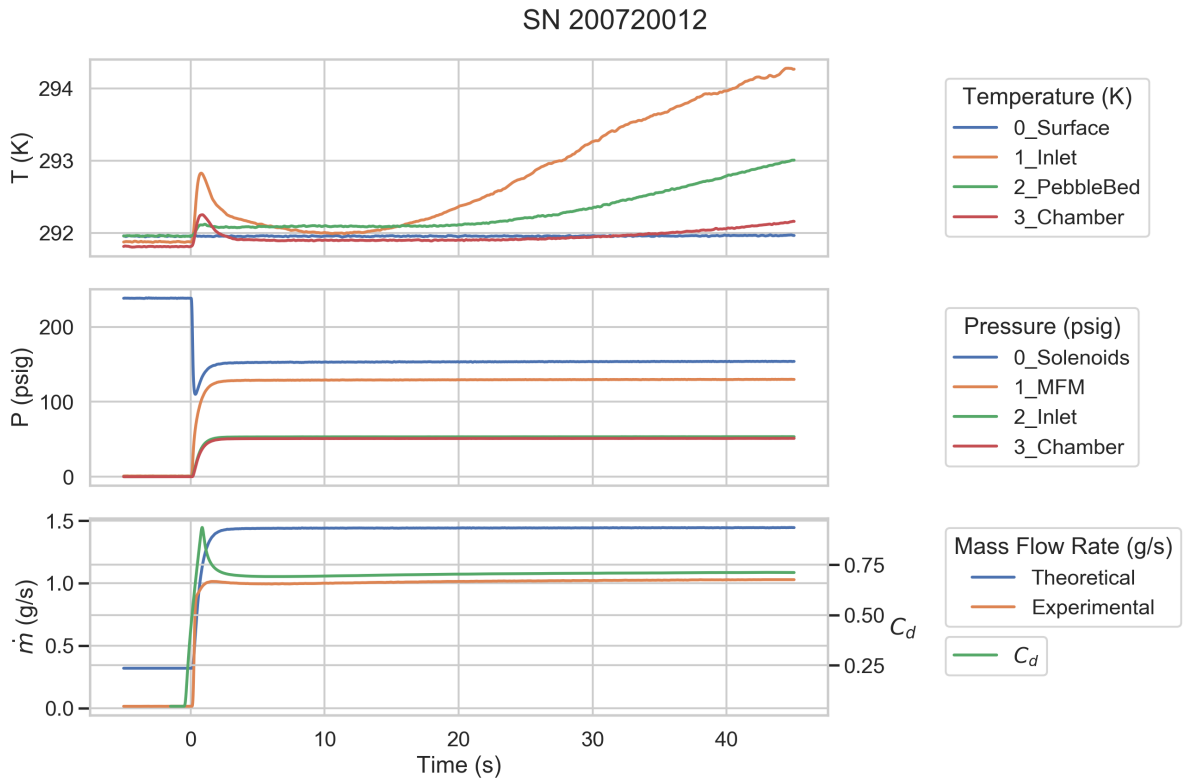

Figure 4.1: Typical experimental data plot for cold gas nitrogen testing, shot number (sn) in yymmddsss format: 200720012.

4.1 Discharge Coefficients

The first thruster configuration (Pebble Bed) relied on a nozzle made of a set screw with a 0.050" hole bored through the center by a machine shop with an orifice length of 0.23". Initial testing revealed a substantially low discharge coefficient of roughly 0.7 due to the high L/d ratio of 5.0. The second thruster configuration (Catalyst Bed) used an upgraded nozzle: a 0.052" high precision orifice plug with a 0.07" orifice length (L/d = 1.4).

Preliminary cold gas testing was first conducted to characterize the discharge coefficient of the thruster and nozzle assembly. A standard experimental data plot is displayed in Fig. 4.1 for room temperature nitrogen testing with a 3" pebble bed. The theoretical mass flow rate was calculated from Equation 1.8.

The discharge coefficient for these cold flow tests was estimated as $C_D = \frac{\dot{m}_{exp}}{\dot{m}_{th}} = 0.75$. Such a low discharge coefficient was anticipated due to the sharp orifice and long L/d value. The discharge coefficient was used to calculate the theoretical mass flow rate in cases where the mass flow meter measurement range of 0 to 50 SLM was exceeded, within a small margin of error. The discharge coefficients were estimated for nitrogen and Tridyne testing in both thruster configurations for a range of preheat temperatures and mass flow rates as presented in Fig. 4.2.

For heated cases, the area ratio (and thus $\dot{m}_{th}$) was not expected to change by more than 1% due to thermal expansion. The adjusted throat area was calculated using $A_{hot} = A_t\Big(1 + 2\alpha T_{hot}\Big)$, where α represents the thermal expansion coefficient of steel with $\alpha = 8.8E-6\ (in/(in^oF))$. The specific heat ratio γ of Tridyne gas also has a slight temperature dependence (1.35 to 1.3) for the temperature range of interest and was calculated based on a curve fit from NASA-CEA's output and the chamber temperature T3.

The two different thruster variations had relatively constant discharge characteristics as seen in Fig. 4.2, where the outliers which had a below-average C_D were due to the experimental flow rate exceeding the 50 SLM limit on the mass flow meter as shown by Fig. 4.3. The otherwise relatively constant C_D for a respective thruster installation was used to extrapolate the anticipated flow rate for these cases.

The major difference impacting mass flow rate between the two thruster configurations (pebble bed versus catalyst bed) was the exit orifice geometry. Other differences which had less of an impact on $\dot{m}$ and C_d were the bed compositions and length. Table 4.1 summarizes the estimated discharge coefficients for each case, which were relatively constant over varying chamber pressures and preheat temperatures for the different installations. The catalyst bed nozzle had a L/d ratio which was 27% of the value for the pebble bed, and the pebble bed had a C_d which was 75% of the value for the catalyst bed.

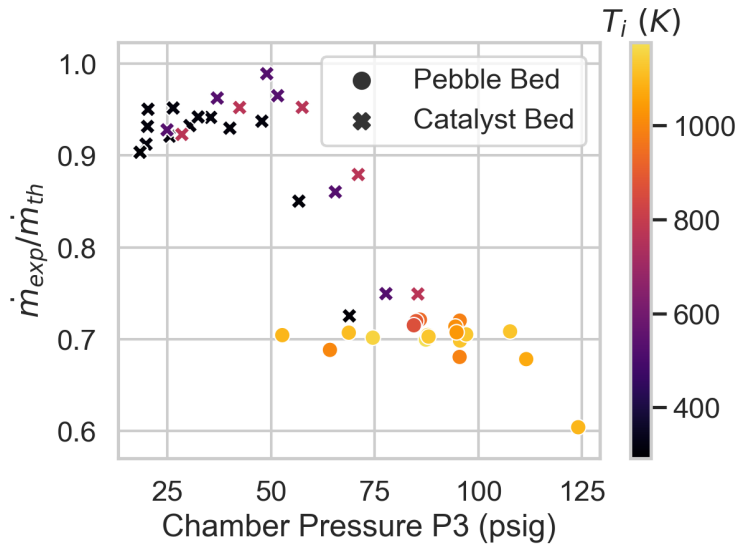

Figure 4.2: Experimental vs. theoretical mass flow rate ratios for different chamber pressures P3 and preheat temperatures T_i for Tridyne gas.

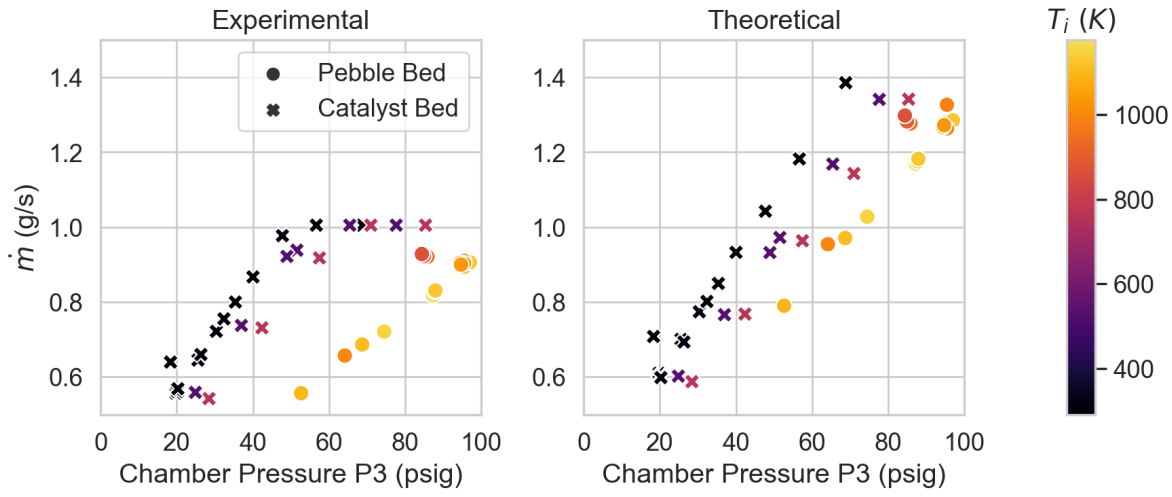

Figure 4.3: Experimental (left) and theoretical (right) mass flow rates for different chamber pressures P3 and preheat temperatures T_i for Tridyne gas. Note the experimental mass flow meter limit was reached at 1.0 g/s.

Table 4.1: Summary of discharge coefficients for different thruster configurations and gas types.

System	Nozzle		Gas	N_{trials}	C_d	
	d_t (in)	L/d			$\overline{C_d}$	σ
Pebble Bed	0.050	5.0	Nitrogen	12	0.757	0.006
			Tridyne	18	0.711	0.009
Catalyst Bed	0.052	1.4	Nitrogen	4	0.909	0.020
			Tridyne	18	0.943	0.016

Limited hot-nitrogen tests were also conducted to attempt to differentiate the effects of heating due to thermal (hot pebble bed convection) and chemical (hydrogen-oxygen reaction). Fig. 4.4 represents the temperature differential between the inlet temperature T1 with the bed temperature T2 and the chamber temperature T3. These data approximate the convective heat transfer to inert nitrogen gas and were subtracted out from T2 and T3 temperature measurements in Tridyne testing, leaving the approximate temperature rise due to the chemical reaction in the gas remaining when assuming similar heat transfer characteristics between nitrogen and unreacted Tridyne.

Upon deconstruction of the pebble bed chamber after heated tests, the chrome steel balls were found to have fused together. The joining of the steel balls is apparent in Fig. 4.5, which shows the balls after deconstruction of the pebble bed thruster. Some of the metals in the 52100 alloy chrome steel balls have sintering temperatures below 1100 K such as aluminum (0 - 0.050%), chromium (1.3% - 1.6%), copper (0 - 0.30%) and manganese (0.25 - 0.45%), with the bulk sintering temperature range of 52100 alloy steel beginning as low as 1190 K - not much lower than the maximum preheat temperature, but definitely lower than the maximum transient temperature due to Tridyne reaction. Some of the elements comprising this 52100 steel alloy may also have experienced oxidation from the hot Tridyne reaction. The maximum temperature attained was 1210 K and the average temperature attained was

1100 ± 60 K for a sum total of 11 hours of heating including three cycles of cooling back to room temperature. It is possible that the steel balls oxidized due to the hydrogen-oxygen reaction in the Tridyne gas.

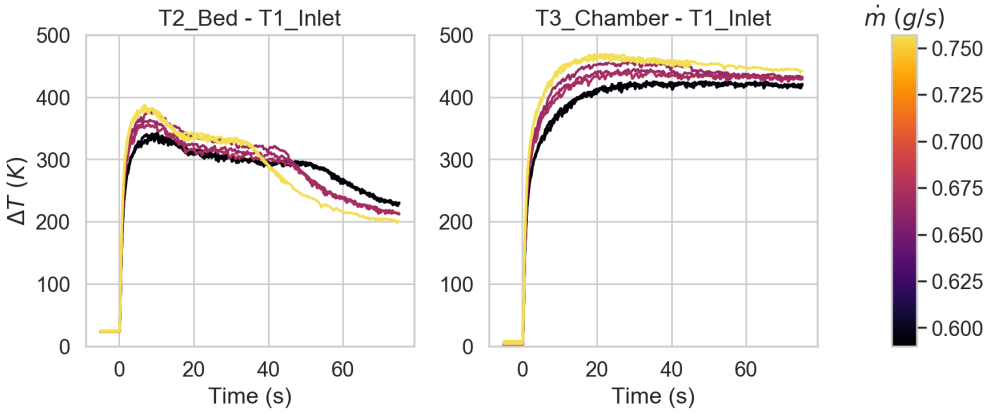

Figure 4.4: Maximum temperature rise for 1100 K nitrogen gas vs. $\dot{m}$ in T2 and T3 with inlet temperatures subtracted.

Figure 4.5: Broken down chrome steel balls after extended heating above 1100 K. Left, slag attached to balls after immediately leaving the thruster. Right, residue dislodged from the balls by manually rolling on a surface.

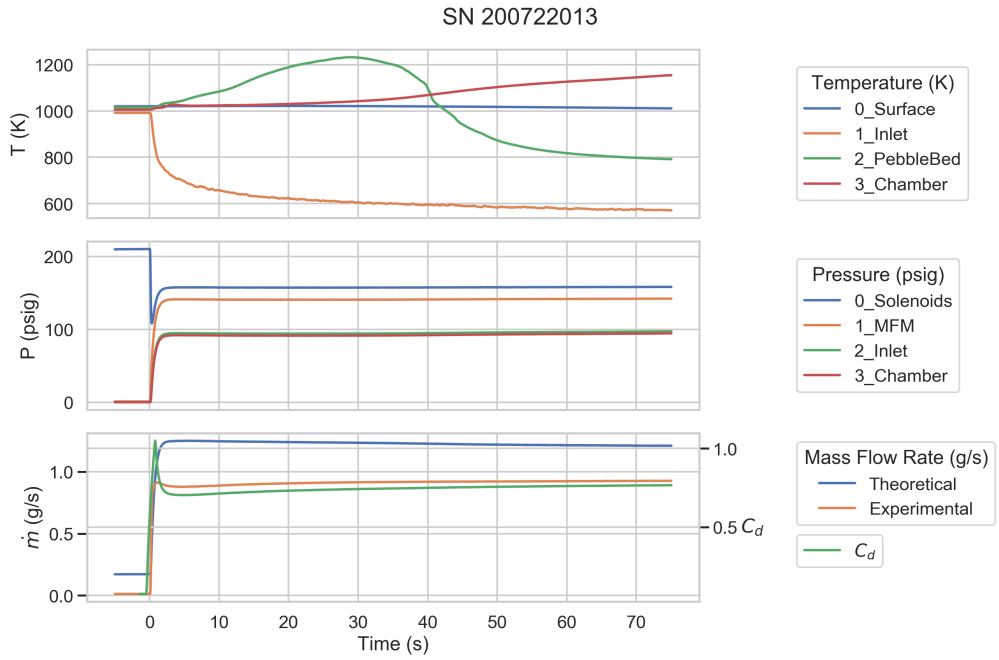

Figure 4.6: Typical data profiles for heated pebble bed Tridyne testing, sn 200722013.

4.2 Pebble Bed

Heated pebble bed testing was performed for a range of chamber pressures P3 and preheat temperatures T_i. A typical experimental data plot is shown in Fig. 4.6. A subtraction of the inlet temperature T1 from the bed and chamber temperatures T2 and T3 was performed in an attempt to reference the temperature plots to the inlet temperature of the gas. This approximated the temperature rise of the gas between the inlet and the exit of the thruster. A subtraction of the heated nitrogen temperature rises based on preheat temperature T_i and mass flow rate $\dot{m}$ dependence in Fig. 4.4 was then performed to isolate the temperature rise in the Tridyne gas due to the chemical reaction.

The pebble bed temperature profiles exhibit an interesting temperature rise/fall profile as displayed in Fig. 4.7, which presents the catalyst bed T2 and chamber T3 temperature profiles for different preheat temperatures. The catalyst bed temperature T2 rose dramatically indicating the onset of the $H_2 - O_2$ reaction, and then increased progressively until

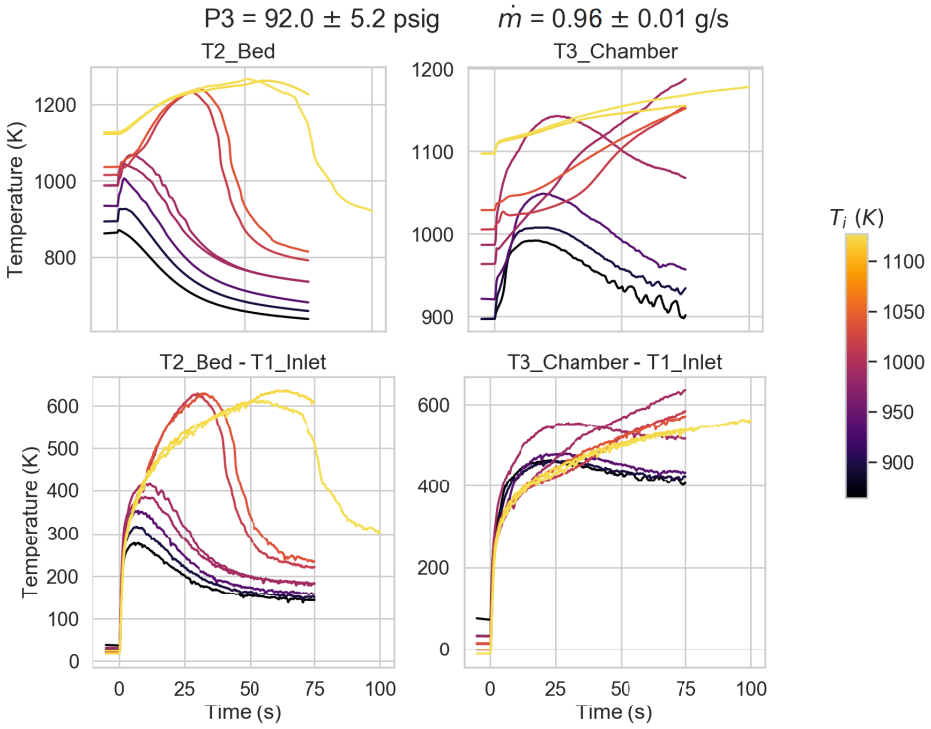

Figure 4.7: Pebble bed temperature profiles for reacting Tridyne gas at constant mass flow rate and varying preheat temperatures. Shots taken from date (in yymmdd format) 200722.

dramatically decreasing. This can be interpreted as a thermal wave passing through the pebble bed, whereby the flowing gas transferred heat away from the pebble bed into the gas. Once sufficient heat was transferred the gas began reacting and, while the flame temperature was higher than the preheat temperature, the gas was not able to replace the heat lost in the pebble bed due to the gas' flow. The reaction front then propagated downstream, leaving a cooled pebble bed behind it until all of the heat in the system was extracted. This speculative effect is depicted by Fig. 4.8.

The same "thermal wave" effect can be seen at the chamber temperature thermocouple T3, however this location may also exhibit steady-state reaction depending on the flow rate and preheat temperature. Once the Tridyne gas has reacted, it will be hotter than the thruster. The rate of heat exchange from this hot Tridyne gas into the thruster body needs

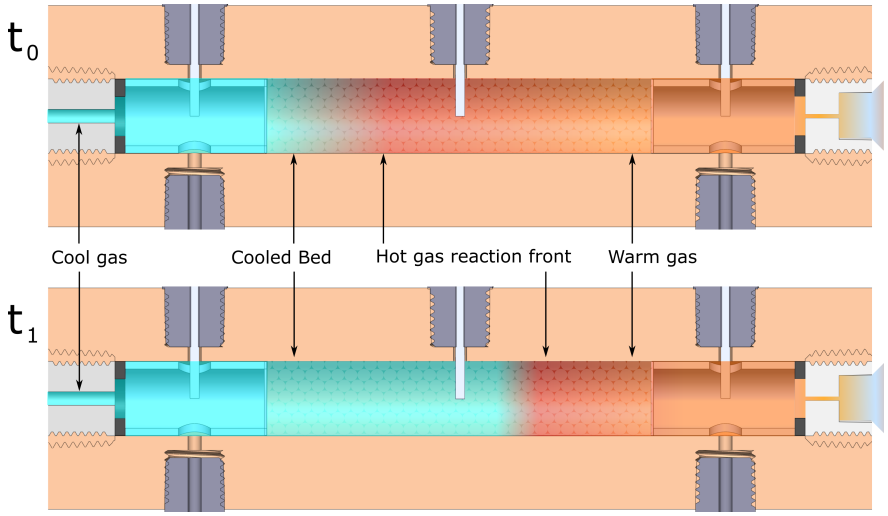

Figure 4.8: Depiction of a speculative thermal wave cooling the pebble bed, propagating the Tridyne reaction front downstream.

to heat up the exit near the throat sufficiently to sustain a reaction there once the thermal energy stored in the pebble bed is depleted. The extent to which this heat transfer occurred was unclear due to the limited spatial resolution of temperature measurements (only one in the pebble bed, one near the throat).

The rate of temperature increase with time appears to scale inversely with the preheat temperature T_i. The time to reach 95% of the maximum temperature (with respect to the initial temperature) was recorded, along with the time it takes to thereafter fall below 95%; the difference between these two was taken to be the "steady reaction time".

The temperature profile based on mass flow rate for a relatively constant preheat temperature is presented in Fig. 4.9. The results are anticipated; higher flow rates ignite the Tridyne reaction faster, but the reactions are also sustained for a shorter duration due to the faster depletion of thermal energy stored in the pebble bed. This corroborates the theory set forth by Fig. 4.8, that slower flow rates will cool the pebble bed slower, with certain cases possibly reaching steady-state.

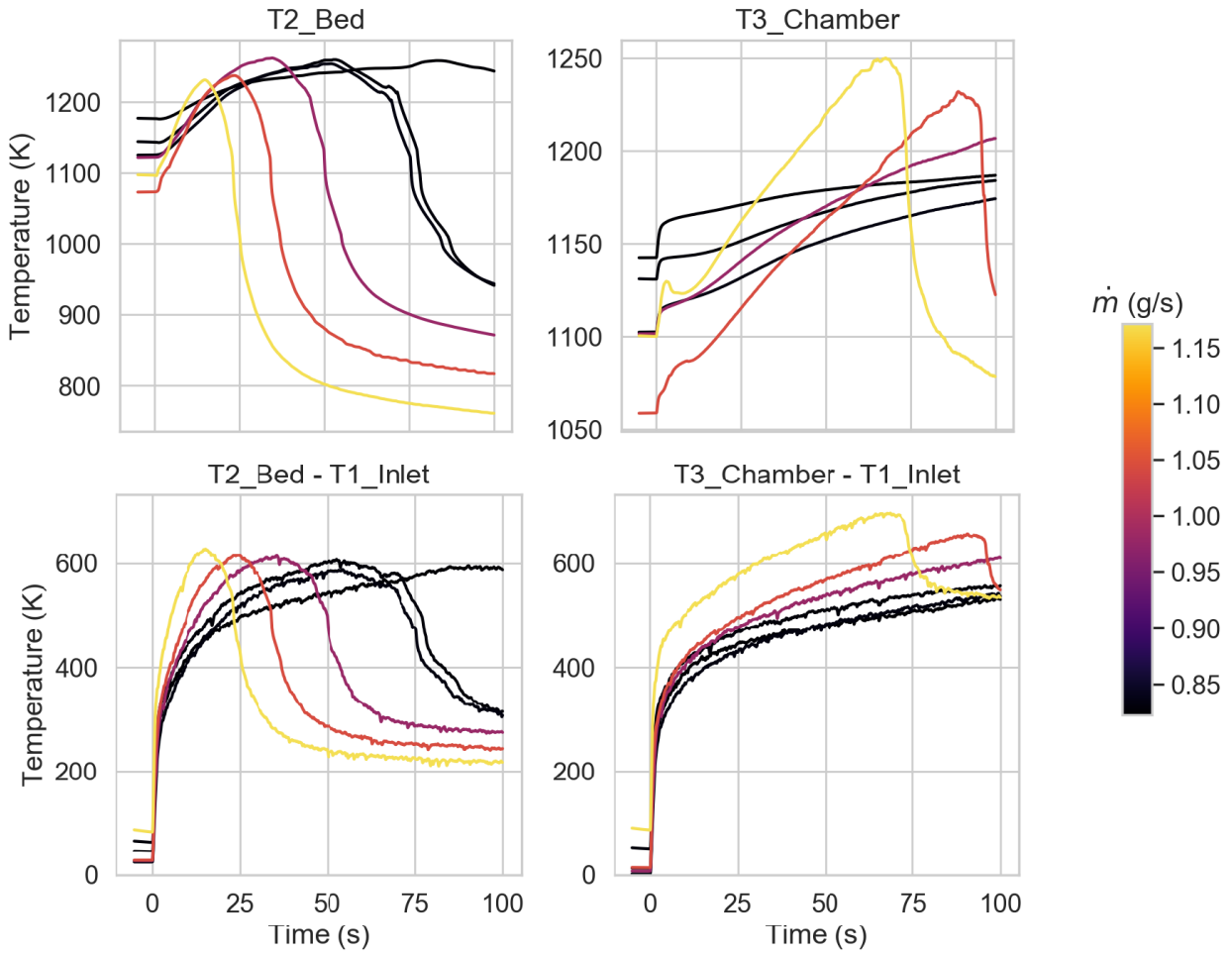

Figure 4.9: Pebble bed temperature profiles for reacting Tridyne gas with preheat temperature ranging 1075 - 1175 K and mass flow rates ranging 0.8 - 1.0 g/s. Date 200723.

A few select cases are explored for steady-state profiles by performing long duration (2.5 to 3 minute) runs as shown in Fig. 4.10. The Tridyne gas supply was limited and thus the number of long-duration trials capable of being run was low. These trials indicate that lower flow rates reach steady-state longer in duration with a lower associated maximum temperature rise.

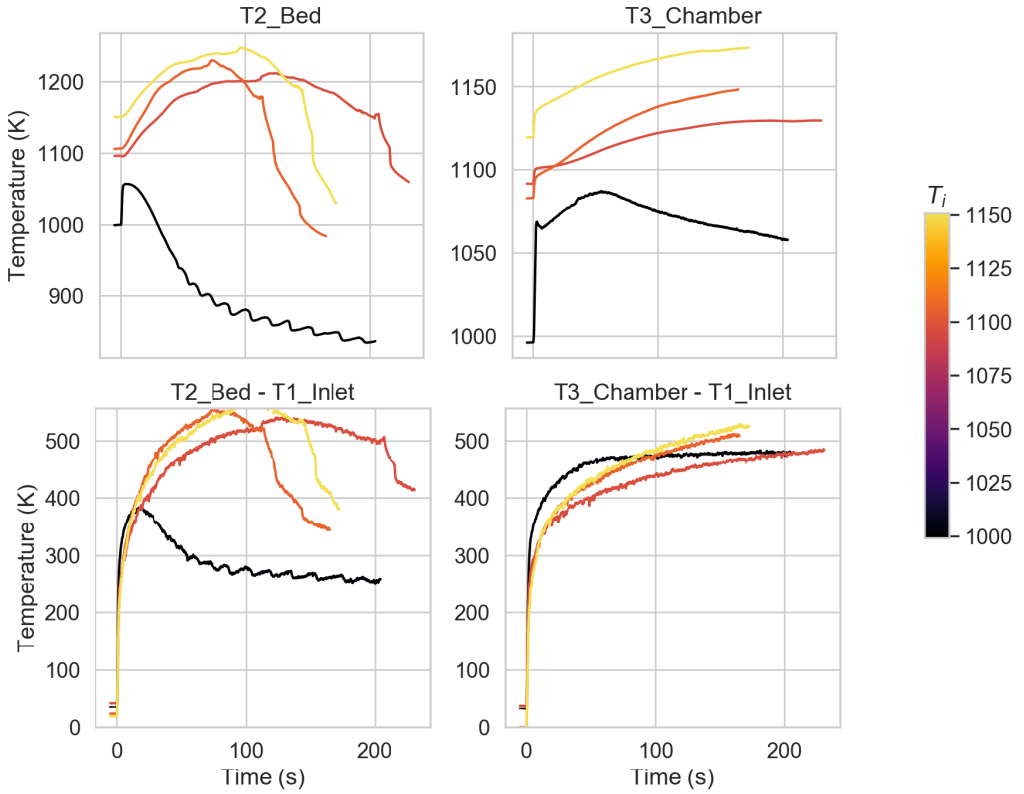

Figure 4.10: Pebble bed temperature profiles for reacting Tridyne gas at extended run durations and various preheat temperatures and mass flow rates. Date 200727.

The steady-state reaction times for all pebble bed cases are presented in Fig. 4.11. Cases where the testing ended before the reaction could decrease from the maximum recorded temperature are denoted with an x marker. Lower flow rates tended to result in longer steady reaction times, as the pebble bed energy was being depleted at a lower rate. The dependency of preheat temperature on maximum temperature rise is elucidated by looking at one range of $\dot{m} = 0.96\ g/s$ in Fig. 4.12. It is more apparent here that the maximum temperature rise peaked at a midpoint temperature of approximately 1000 K as previously described. The maximum achievable temperature was likely limited by the heat transfer between the gas and the thruster walls and atmosphere, as opposed to the enthalpy of the gas.

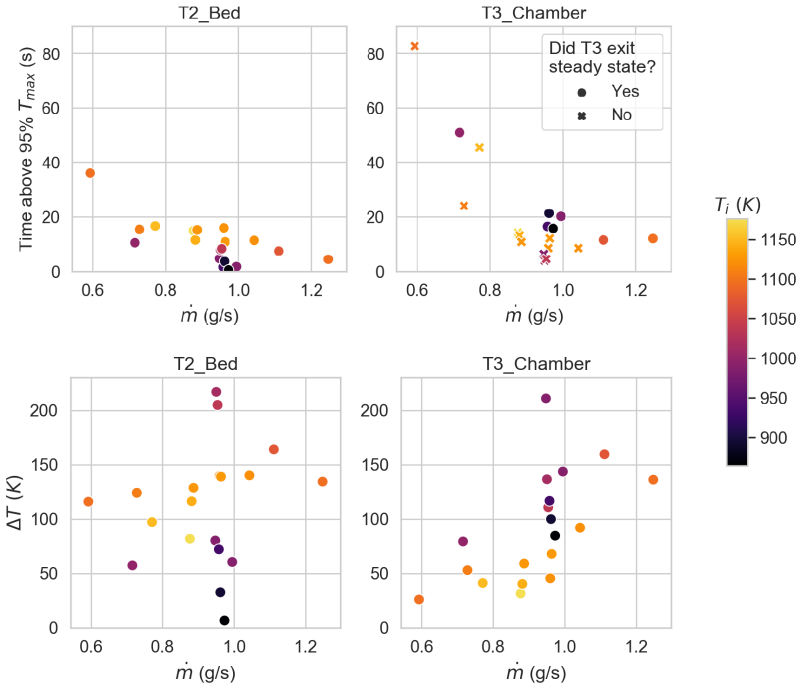

Figure 4.11: Tridyne steady reaction times (top) and temperature rise (bottom) for the pebble bed thruster at varying preheat temperatures and mass flow rates. Horizontal variations in ΔT are with constant T_i, vertical variations with constant $\dot{m}$.

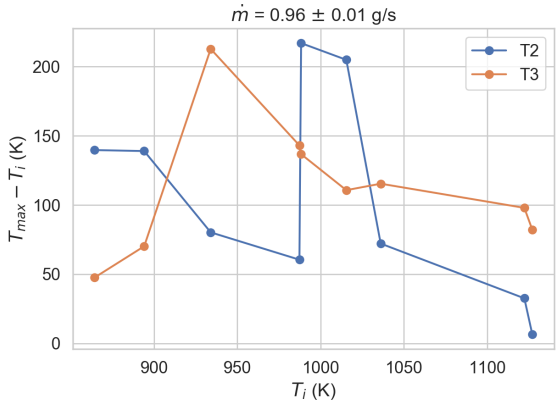

Figure 4.12: Tridyne maximum temperature rise for the pebble bed thruster for various preheat temperatures with $\dot{m} = 0.96$ g/s.

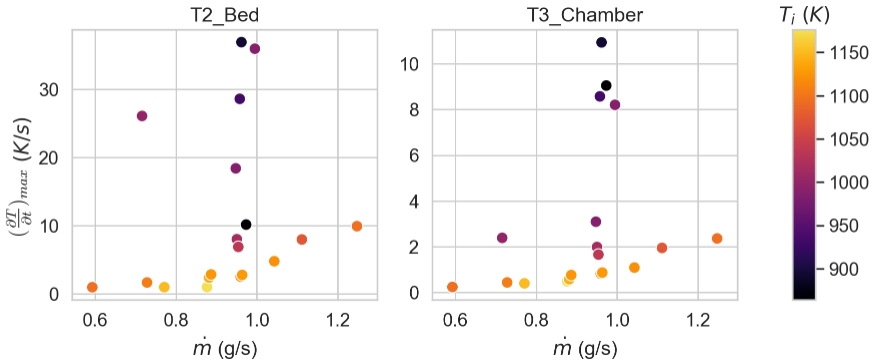

Figure 4.13: Tridyne mean temperature gradients for pebble bed center (left) and chamber (right) for the pebble bed thruster at varying preheat temperatures and mass flow rates. Horizontal variations in $\frac{\partial T}{\partial t}$ are with constant T_i, vertical variations with constant $\dot{m}$.

The associated time derivative of temperature in Fig. 4.13 for the pebble bed thruster configuration follow a more direct, albeit less readily understood profile; higher preheat temperatures result in a significantly slower temperature rise. This is contrary to what is expected from standard kinetic collision theory. Temperature is a measure of the inherent energy of a system; a gas with a higher temperature will have a higher distribution of sufficiently energetic particles to propagate the Tridyne reaction. More particles with sufficient energy implies more frequent successful collisions, which means the reaction will progress more rapidly. Experimentally, the inverse was seen here; lower preheat temperatures tended to result in a faster rise from initial to maximum temperature.

This deviation was, again, possibly due to heat transfer between the gas, thruster and atmosphere. It is true that a higher temperature gas should react faster and thus have a greater temperature release rate, however that is not what was directly measured here. The temperature measured here is at a discrete location within the thruster, beginning at an elevated temperature in the range of 875 to 1175 K. The gas entered the system at 290 K; after sufficient convective heat transfer had occurred from the pebble bed, the gas would have become sufficiently hot to react.

It should be noted that the temperature which the gas began reacting at was not neces-

sarily the preheat temperature of the catalyst bed. This explains the apparent "diminishing return" of ΔT in Fig. 4.12, and furthermore explains the decrease in mean $\frac{\partial T}{\partial t}$ for higher temperatures. The gas possibly reacted at the same temperature regardless of preheat temperature, with preheat temperature just controlling how soon that reaction would take place due to a larger temperature differential resulting in more rapid convective heat transfer into the gas. Once the gas reached a sufficient temperature to react, however, the final gas temperature would be determined by an adiabatic limit and is thereafter independent of the preheat temperature of the thruster. A hotter thruster preheat will thus have a smaller temperature differential with respect to the reacted Tridyne and will therefore experience slower heating.

The rise time to maximum temperature for the pebble bed cases is plotted in Fig. 4.14. Two trends are noticed; for low preheat temperatures, the rise time was nearly instantaneous. A clear time profile of this is displayed in Fig. 4.10. The reactions in these cases quickly ceased, matching the theory of auto-ignition temperature from Section 2.3 which suggests >1000 K preheat temperatures would be most successful in igniting and sustaining a Tridyne reaction. At temperatures >1000 K, the rise time decreased proportional to mass flow rate as the heat transfer between the gas and pebble bed occurred on a faster time scale. These rise times are not representative of the time it took the gas to react, but rather of the time it took for the hot Tridyne reaction front illustrated in Fig. 4.8 to propagate downstream.

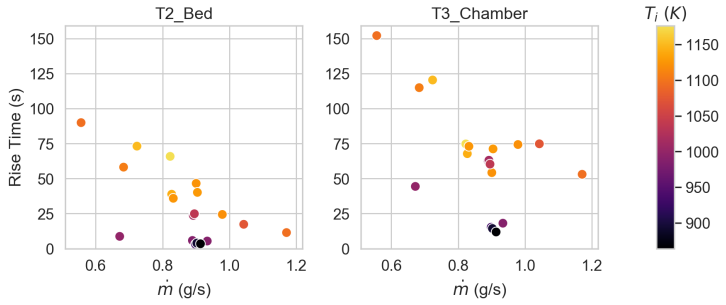

Figure 4.14: Rises times for maximum temperature in pebble bed thruster for T2 and T3 versus preheat temperature T_i and mass flow rate $\dot{m}$.

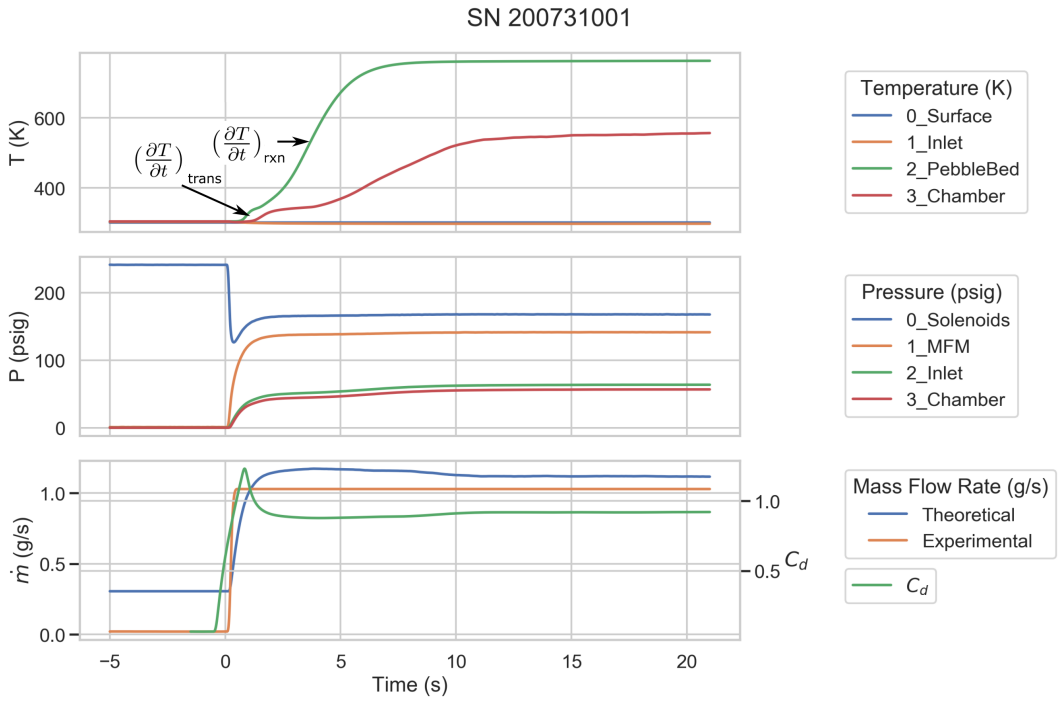

Figure 4.15: Typical shot data for 290 K catalyst bed Tridyne testing, sn 200731001.

4.3 Catalyst Bed

Tridyne testing using the S-405 catalyst bed was conducted for a range of chamber pressures and preheat temperatures. Representative data are presented in Fig. 4.15. The catalyst testing appeared to result in substantially less data scatter than the pebble-bed case; the catalyst bed T2 profile in particular rose a small amount, leveled off briefly, and then rose significantly until reaching a steady-state reaction temperature. The instantaneous temperature gradient maxima for these two regions of temperature rise was reliably extracted as scalars for each shot, in addition to the mean temperature gradients during the rise time from the initial to maximum temperature. The temperature gradients and their associated timings provide an indication of how quickly the Tridyne reaction proceeded to completion.

The decrease in temperature from T2 to T3 may be due to the reaction proceeding as far as possible within the catalyst bed and thereafter only cooling due to heat transfer with the

thruster walls. The thruster is a massive heat sink with 0.5" thick walls that readily conducts heat away from gas in the thrust chamber. An ideal thruster would expand the gas as soon as the reaction has completed, which would be more suitable for the flight-weight CubeSat thruster configuration. In the current study however, the desire to fully diagnose the thruster for different flow and reaction regimes resulted in the actual experimental c^* being quite low due to gas at T3 having cooled significantly from T2. This c^* value is reported and compared with the "theoretical experimental" c^*, which presumes that the exit of the thruster is at the exit of the catalyst bed where the temperature is greatest.

Typical Tridyne reaction temperature profiles are displayed in Fig. 4.16 for varying flow rate. The consistency of the data was generally higher than those for the pebble bed. Generally a lower flow rate resulted in a longer temperature rise time; the local maximum time rates of temperature change $(\frac{\partial T}{\partial t})_{max}$ for the reaction startup transience and their associated times as illustrated in Fig. 4.15 were extracted and are displayed in Fig. 4.17. The full reaction $(\frac{\partial T}{\partial t})_{max}$ occurred 2.3 seconds faster for 1 g/s flow rates (t = 3.9 s) than for 0.5 g/s flow rates (6.2 s). The time delays for the startup transient $(\frac{\partial T}{\partial t})_{max}$ are proportionally identical to the case for the complete reaction, occurring 0.6 seconds faster for 1 g/s flow rates (t = 1.0 s) than for 0.5 g/s flow rates (t = 1.6 s). The relative magnitudes of $(\frac{\partial T}{\partial t})_{max}$ as they relate to flow rate do not have any discernible trend at the current resolution of shot data. The trend of $(\frac{\partial T}{\partial t})_{max}$ timing decreasing for higher flow rates is consistent with the bed being loaded with gas at a higher rate, speeding up the production of a radical OH pool which generates heat and propagates the reaction. The consistently proportional timing between the startup transience $(\frac{\partial T}{\partial t})_{max}$ and the complete reaction $(\frac{\partial T}{\partial t})_{max}$, along with the scaling of these timings with respect to mass flow rate, suggest this leveling-off process of the Tridyne reaction which separates the startup transience phase from the complete reaction phase is a physical phenomenon associated with the Tridyne flow over the catalyst bed. This transient leveling-off process is not present in typical catalyzed exothermic reactions. [4] Further investigation into the chemistry and physics behind this leveling-off process would benefit from increased spatial resolution of temperature measurements in the catalyst bed.

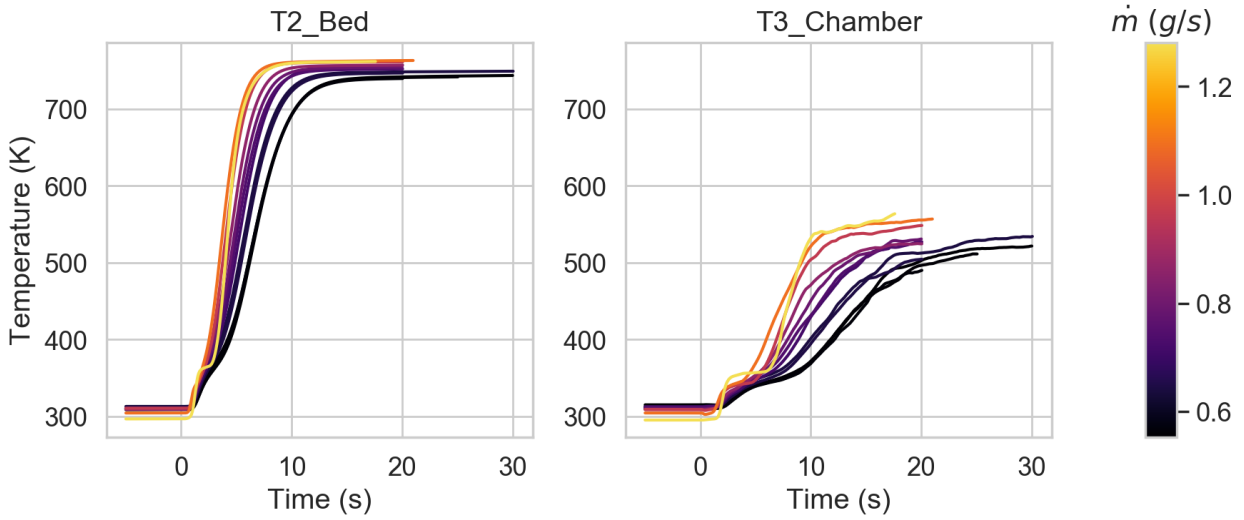

Figure 4.16: Temperature profiles for Tridyne testing with S-405 catalyst bed for varied $\dot{m}$.

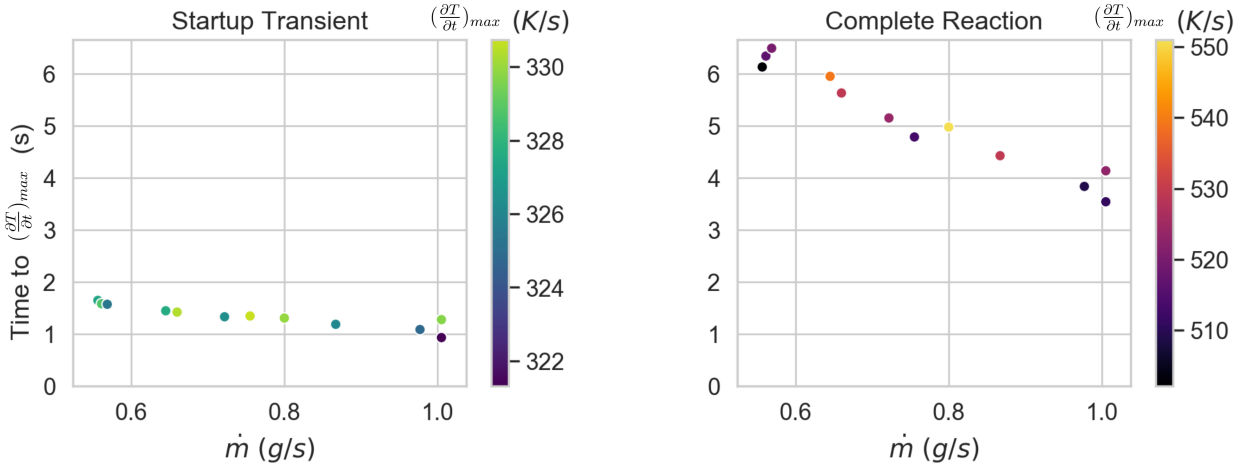

Figure 4.17: Time to local maximum in temperature gradient for the two phases of the room temperature Tridyne reaction vs. $\dot{m}$ and the associated magnitude of $(\frac{\partial T}{\partial t})_{max}$.

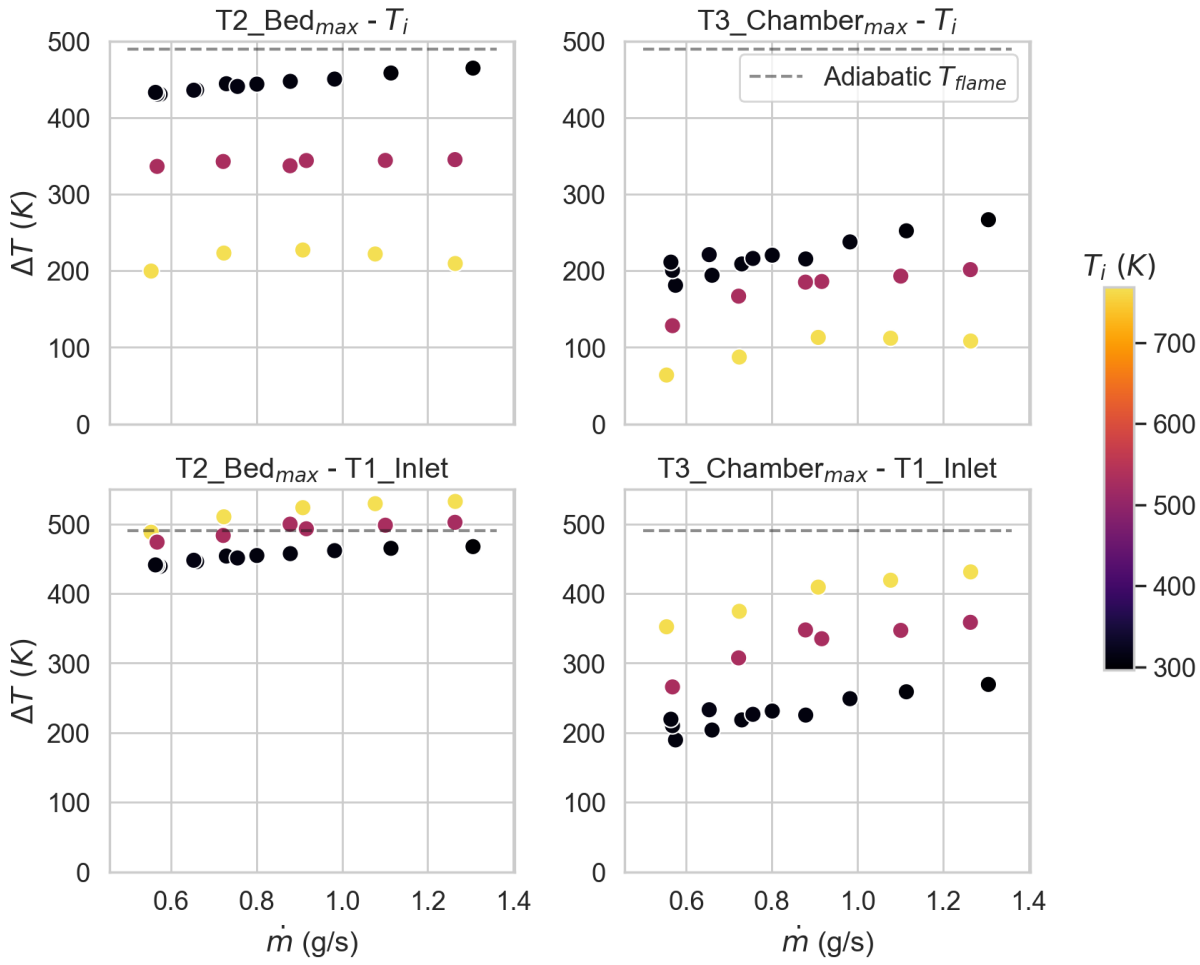

Figure 4.18: Maximum change in bed and chamber temperatures for heated catalyst shots versus $\dot{m}$. Top row represents change in thermocouple measurement, bottom row represents approximate change in gas temperature due to chemical reaction.

The Tridyne reaction with a heated catalyst bed was also studied for two catalyst bed preheat temperatures: 530 K and 760 K. The maximum temperature rise in T2 and T3 for all three preheat temperatures vs. $\dot{m}$ is displayed in Fig. 4.18. Note the temperature rise presented at the top of the figure is the measured rise of the thermocouples themselves, which started at an elevated preheat temperature; it was probable that the gas in the heated catalyst bed cases reached a comparable degree of completion as for the room temperature case. Considering this, the inlet temperature T1 was subtracted from the T2 and T3 measurements to isolate total temperature rise of the gas. In the pebble bed case, as stated the hot nitrogen temperature profiles approximated convective heat transfer within the pebble bed and were subtracted out, leaving an approximate temperature rise of the gas due solely to the Tridyne chemical reaction. For the catalyst bed cases the reaction was anticipated to occur much more spontaneously; the Tridyne was expected to react after passing over only a small portion of the heated catalyst bed. Upon reacting, the flame temperature would be much higher than the preheat temperature of the bed itself. Thus the same procedure for subtracting hot nitrogen profiles in the pebble bed thruster configuration not produce reliable results for this catalyst bed thruster configuration.

The temperature increase of the unreacted cool Tridyne gas due to heat transfer with the hot pebble bed, which was anticipated to occur within the leading portion of the catalyst bed before the gas began reacting, was not accounted for and explains why the approximation of gas temperature rise for the heated cases was greater than the adiabatic flame temperature. This heat transfer between the cool unreacted gas and hot catalyst bed is anticipated to be minimal. This anticipation matches the measured temperatures exceeding the adiabatic flame temperature by up to 50 K, or 10%. The catalyst bed temperature and chamber temperature time profiles were measured for three different preheat temperatures are shown in Fig. 4.19, referenced to inlet gas temperatures shown in Fig. 4.20.

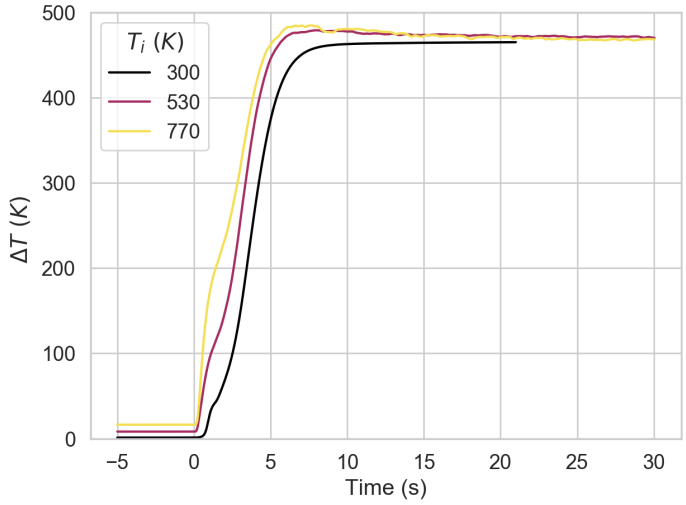

Figure 4.19: Tridyne temperature time profiles for reaction over S-405 catalyst bed at three preheat temperatures T_i. The inlet temperature T1 was subtracted in each case to isolate temperature increase due to the Tridyne chemical reaction.

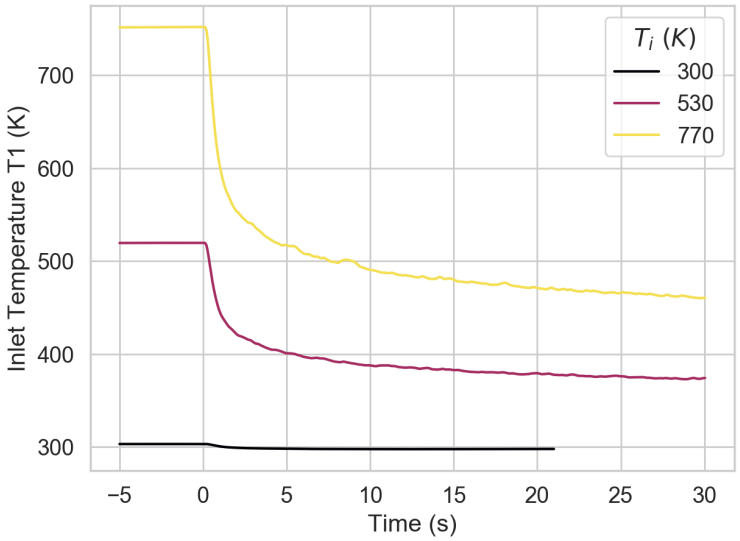

Figure 4.20: Typical inlet temperature T1 profiles for $\dot{m} = 1.08$ g/s and three different preheat temperatures.

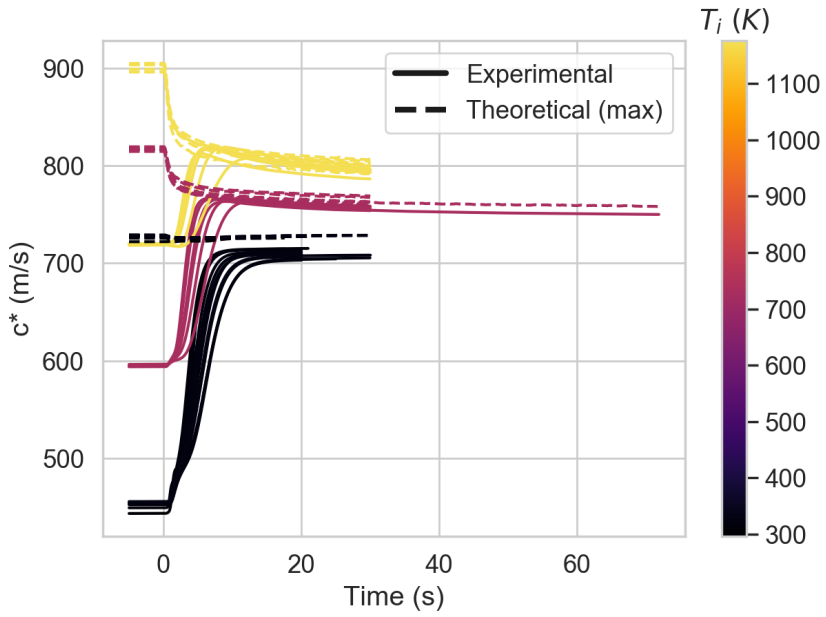

Figure 4.21: Theoretical and experimental characteristic velocities at the catalyst bed vs. time for S-405 testing at three preheat temperatures.

The c^* efficiency was calculated for a range of flow rates and preheat temperatures by calculating the adiabatic flame temperature based on the steady-state inlet temperature. This c^* efficiency was calculated two ways: using pressure measurements, and using temperature measurements. Recall the adiabatic flame temperature profile of Fig. 2.3 and the c^* equations from Section 1.1.2. The theoretical and experimental time profiles of c^* for catalyst bed Tridyne shots vs. preheat temperatures are displayed in Fig. 4.21 for the catalyst bed.

The theoretical characteristic velocity was calculated by using the preheat-temperature-dependent adiabatic flame temperature from NASA CEA, which was estimated based on the gas inlet temperatures. This also matches the "theoretical experimental" characteristic velocity calculated in the catalyst bed at $T2$, which reached adiabatic flame temperature as demonstrated in Fig. 4.18. This value represents the ideal combustion performance. For a flight-weight thruster, the nozzle should be placed at this location rather than 2.8 inches upstream as the gas cools due to heat transfer with the thruster walls after reacting.

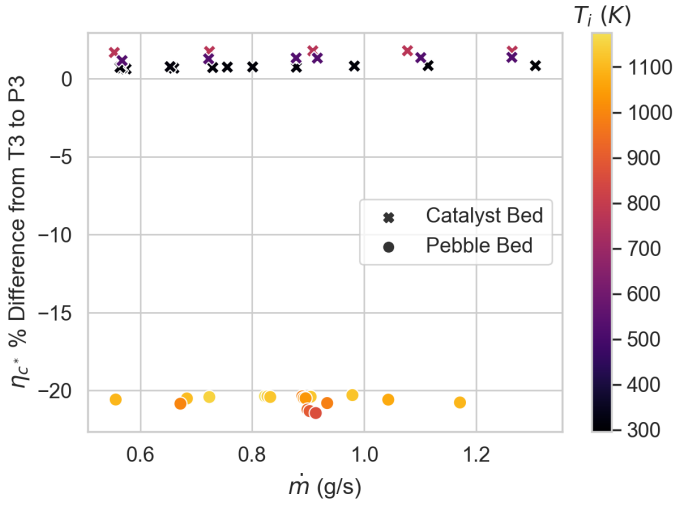

Figure 4.22: Percent difference in c^* efficiency (η_{c*}) calculation between T3 and P3 for catalyst and pebble bed tests.

The experimental characteristic velocity reported was calculated using chamber temperature T3, but was also be calculated by looking at chamber pressure P3 combined with the mass flow rate; the difference between calculating c^* by T3 vs. P3 and $\dot{m}$ was found to be negligible for the catalyst bed case (1%) but substantial for the heated pebble bed case (20%) as shown in Fig. 4.22. The chamber temperature c^* calculation is reported over the chamber pressure calculation in both cases for consistency with the theoretical c^* and "theoretical experimental" c^* at the catalyst bed center, which both rely on temperature measurements.

The characteristic velocities are calculated after estimating the gas temperature increase by subtracting the inlet temperatures as indicated in Fig. 4.19 and Fig. 4.20. The "theoretical experimental" characteristic velocity time profiles in the catalyst bed at thruster preheat temperatures of 290 K, 530 K, and 760 K are shown in Fig. 4.23.

The c^* efficiencies (η_{c*}) for all tests are reported in Fig. 4.24. The reaction front in the catalyst chamber was seen to essentially reach the theoretical adiabatic flame temperature for all cases ($\eta_{c*} = 1$). For the catalyst bed an $\eta_{c*} = 1$ occurs at T2, implying the reaction goes to completion halfway through the catalyst bed and thus at least the back half of

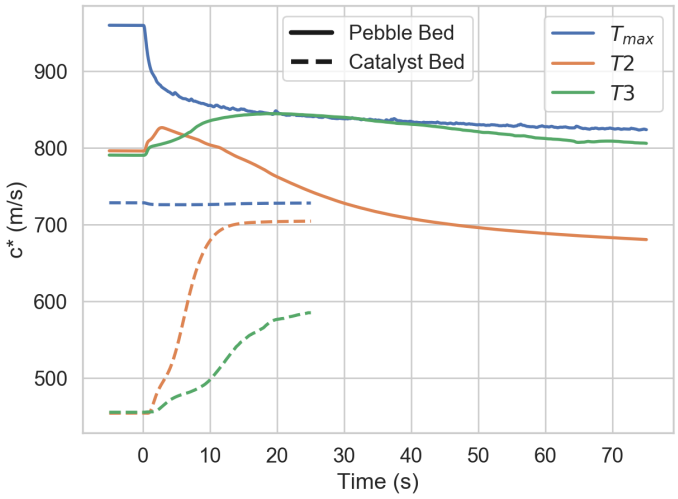

Figure 4.23: Theoretical and experimental characteristic velocities for pebble and catalyst beds. Blue curves represent the theoretical adiabatic flame temperatures T_{max}. SNs 200722015 (pebble, solid line) and 200731010 (catalyst, dashed line).

the catalyst bed is unnecessary. The c^* efficiency data for the pebble bed are often local maxima except at flow rates below 0.8 g/s, where steady-state reaction was sustained. The steady-state reaction timings for the pebble bed thruster are presented in Fig. 4.11. For the duration of the steady-state reaction times, complete ignition at the chamber temperature T3 was achieved after having completely passed through the pebble bed. Reported pebble bed η_{c*} values exceed 1.0 but are still within the anticipated 20% error range from Fig. 4.22.

After the Tridyne has reacted, the temperature in the gas cools due to heat transfer with the thruster walls. The distance between T2 and T3 is 1.8". The reported characteristic velocity at T3, while technically the true characteristic velocity efficiency of this thruster for atmospheric testing, is at this point mostly a measure of the extent of gas heat loss in the system. It is anticipated that a hotter thruster will extract less heat from the flowing gas, matching the values presented here. Future experiments should reduce the catalyst bed length and increase spatial temperature resolution along the bed to better characterize the Tridyne reaction. The thruster configuration should also have thinner walls to enable more

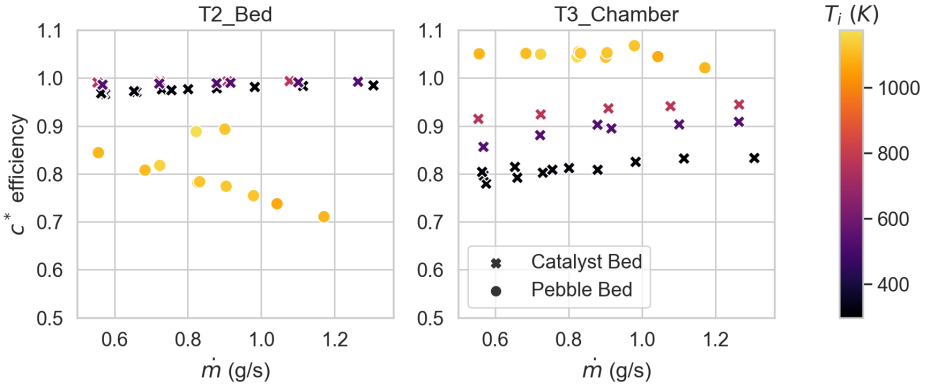

Figure 4.24: Characteristic velocity efficiencies for all Tridyne shots. Error bars for the pebble bed shots are not shown for clarity but include variance of ± 0.15.

rapid heat up. Changes in the insulation between the thruster and atmosphere should also impact the temperature measured at $T3$. Vacuum testing should also reduce the impact of heat transfer between the thruster and atmosphere.

The rise times for T2 and T3 to reach their steady-state, maximum temperatures for the catalyst bed thruster configuration are presented in Fig. 4.25, along with the mean temperature time rates of change. Higher flow rates were seen to reduce the rise time significantly, with higher preheat temperature further reducing the rise time (at a proportionally lower rate). In the context of average temperature gradients, this suggests that a hotter catalyst bed will propagate the Tridyne reaction at a higher rate.

The location at which T2 was installed, 0.6 inches within the S-405 catalyst bed, is roughly consistent with the catalyst length of the flight-weight thruster (rather than continuing for an additional 2.8" in the thruster). The temperature rise time measured at T2 is thus the most representative for performance analysis of the designed flight-weight thruster. The fastest achieved rise time was 7 seconds from a room-temperature catalyst bed. This is a comparatively slow startup time not ideal for a CubeSat thruster; the market niche where the ΔV and total impulse of this technology is competitive with the state-of-the-art is for simple attitude control thrusters, for which reliable and precise impulse bits are required.

The maximum mass of Tridyne propellant which can be stored for a 1.5U thruster is 900 g at 100 MPa (14,500 psi) based on estimates in Section 2.2; barring the challenges of storing and regulating such a high pressure in a confined volume in space, this mass translates to 720 seconds of flow for the nominal 0.8 g/s flight-weight thruster flow rate. A 7 second rise time thus represents a 1% loss of the initial propellant mass every time the thruster is turned on, which is a significant inefficiency for an attitude control thruster. This technology is better suited for a mission where minimal thruster on/off cycles are required. The trade-off of startup propellant loss should be evaluated against the other benefits of a Tridyne propulsion system such as extremely low required operating power - just the power to turn on and sustain a magnetic latching solenoid valve is needed and, unlike refrigerant thrusters, there is no resistive heating involved.

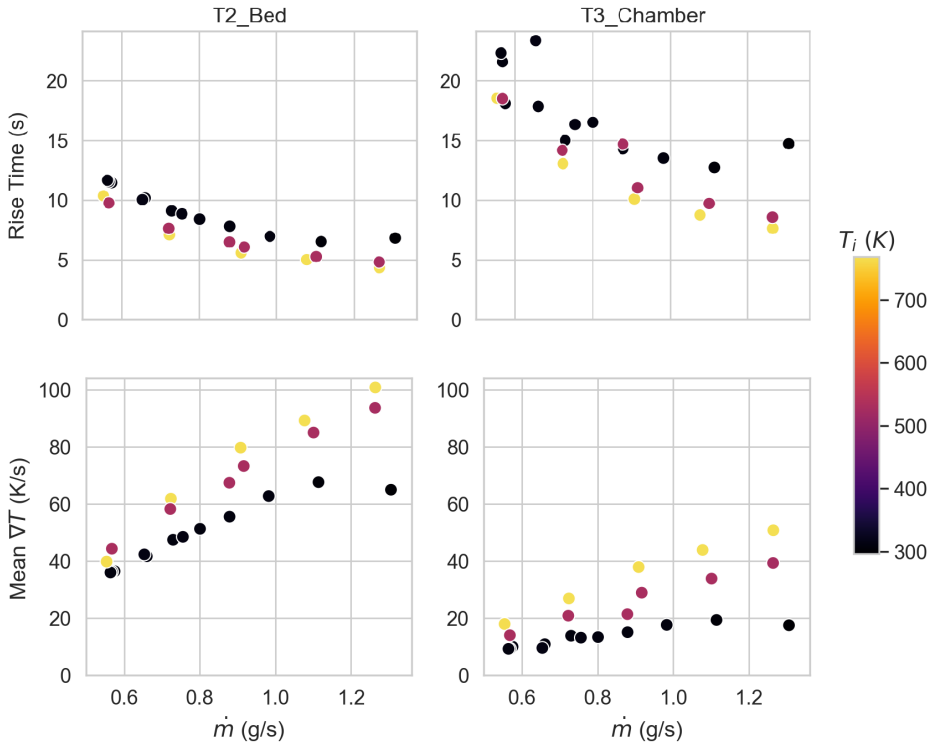

Figure 4.25: Catalyst bed thruster rises times for T2 and T3 maxima versus preheat temperature and mass flow rate.

Chapter 5

CONCLUSIONS

Post varios annos, per mille figuras,
Rursus ad humanæ fertur primordia vitæ

—Claudis, *In Rufinum*, 2, 1, cdxciii.

A Tridyne microthruster was developed and evaluated with a combination of computational modeling and experimental validation at the University of Washington. The Tridyne propellant is a 2:1 stoichiometric mix of hydrogen and oxygen with balance nitrogen catalyzed by the iridium-alumina S-405 catalyst. Nominally the Tridyne blend is 10% H_2, 5% O_2 by volume to maximize performance. For the laboratory testing in this effort the Tridyne blend was 6% H_2, 3% O_2 by volume due to gas supplier limitations. The designed Tridyne micropropulsion system is in the thrust class of 10 mN to 1 N and has significant advantages over other propellants such as minimal required power, extreme simplicity, and high specific impulse. This propellant requires high storage pressure to be competitive with the state-of-the-art in micropropulsion and requires a reaction startup time on the order of 5 seconds.

Chemical equilibrium analysis was performed for a range of Tridyne reactant concentrations, preheat temperatures, and storage pressures using NASA-CEA and CANTERA. The auto-ignition temperature was estimated in the range of 900 to 1000 K and validated experimentally using a heated pebble bed in the thrust chamber. The Tridyne mixture was found to be inert for any range of reactant concentrations below 800 K in the absence of a catalyst. The adiabatic flame temperature was calculated for a range of preheat temperatures and applied to experimental results to estimate c^* efficiencies. Increasing reactant concentration was found to increase the adiabatic flame temperature, with an ideal reactant concentra-

tion of 10% H_2 and 5% O_2 with balance N_2 providing a flame temperature of 1400 K. This temperature is ideal to maximize longevity of S-405 catalyst based on previous research.

Theoretical performance estimates are conducted in Python by solving a volume-constrained pressure vessel for a range of propellant storage pressures and material properties. The performance was found to be over 2x greater than conventional state-of-the-art saturated liquid thrusters when using an additively-manufactured titanium propellant storage tank. For a 1.5U thruster, the estimated maximum achievable total impulse is 1400 N-s with 900 g of Tridyne for a 100 MPa (14,500 psi) storage pressure. A minimum storage pressure of 20 MPa (2,900 psi) is required to compete with VACCO's R-236fa Standard MicroPropulsion System (MiPS), representing conventional state-of-the-art for saturated liquid thrusters.

A flight-weight 1.5U CubeSat propulsion unit was designed using a mix of commercial off-the-shelf components, including solenoid control valves and pressure transducers, and custom components such as an additively manufactured propellant tank and fill/vent port. The system was estimated to have 1.3U of the 1.5U volume available to be devoted to the propellant tank. The remaining 0.2U volume is required for the plumbing and instrumentation of the propulsion unit.

A bench-top experiment was designed, built, and tested for the performance characteristics of Tridyne while varying mass flow rate, preheat temperature, and reaction mechanism. The reaction was ignited using a hot pebble bed, and also catalyzed to ignition using S-405 catalyst. The hot pebble bed lost temperature proportional to the mass flow rate. Adiabatic flame temperatures were temporarily reached for all flow rates in the thruster exit for the pebble bed thruster, with sustained reactions occurring at the thruster exit for flow rates below 0.8 g/s. Heat transfer evidently plays a substantial effect in the interactions of reacting Tridyne gas with a heated pebble bed, complicating isolation of the temperature increase due purely to the chemical reaction.

The bench-top thruster with S-405 catalyst was found to repeatably and predictably catalyze the Tridyne reaction. Characteristic velocity efficiencies in the range of 0.97 to 1.0 were identified in the catalyst bed ("theoretical experimental" η_{c*}) for varying preheat

temperatures, with values at the thruster exit (experimental η_{c*}) in the range of 0.78 to 0.94 due to convective cooling of the reacted Tridyne gas with the thruster walls. Achievable η_{c*} for the flight-weight configuration is estimated in the range of 0.92 tp 1.0.

The temperature rise times for the Tridyne reaction in the catalyst bed were found to be in the range of 5 to 12 seconds, dependent on preheat temperature and mass flow rate. For a theoretical 1.5U thruster, this translates to a minimum 1% of the total stored propellant being lost every time the thruster is turned on. This is a substantial loss and suggests Tridyne would be better used in a ΔV-class mission with minimal cycling of the mass flow, rather than for attitude control which requires precise and reliable impulse bits.

5.1 Future Work

In-depth analysis of S-405 catalyst degradation versus flame temperature and thermal cycling is recommended for future investigation. The flame temperature, and thus performance, should be maximized while balancing S-405 catalyst degradation with an appropriate factor of safety based on mission requirements. Future work should consider transport properties calculated by the chemical equilibrium analysis simulations, such as viscosity and conductivity, and perform in-depth convective heat transfer analysis on the proposed thruster.

The pebble bed should be outfitted with a greater spatial resolution of thermocouples to increase confidence in isolation of the temperature rise due to heat transfer. Extended nitrogen testing at varying temperatures and flow rates should also be performed, along with computational modeling of convective heat transfer in the pebble bed.

Considering that combustion goes to completion within 0.6" of catalyst flow length, a new thruster should be designed using less catalyst and outfitted with more thermocouples to study the spatial reaction profile of Tridyne in an S-405 catalyst bed. The thickness of these walls should also be reduced to reduce the impact of heat transfer between the hot gas and thruster walls. The trade-off of startup propellant loss based on temperature rise times should be evaluated in-depth against the other benefits of a Tridyne propulsion system such as extremely low required operating power.

This effort was funded by the State of Washington's Joint Center for Aerospace Technology Innovation (JCATI) and partnered with Aerojet Rocketydyne of Redmond, WA, with an additional round of funding granted for Phase 2 of the project. Phase 2 of this project will construct a flight-weight 1.5U Tridyne propulsion unit and validate it in laboratory and vacuum conditions.

BIBLIOGRAPHY

[1] N. A. of Sciences Engineering and Medicine, *Achieving Science with CubeSats: Thinking Inside the Box*. The National Academies Press, 2016. 10.17226/23503.

[2] K. Lemmer, "Propulsion for cubesats," *Acta Astronautica*, vol. 134, pp. 231–243, 2017.

[3] N. Cohen, "Flammability and explosion limits of h2 and h2/co: a literature review," tech. rep., Aerospace Corp. El Segunda, CA Technologt Operations, 1992.

[4] H. Barber and C. Buell, "Tridyne attitude control thruster investigation," tech. rep., Rocketdyne, Apr 1970. Report No. R-8144.

[5] V. Industries, "Standard micro cubesat propulsion system." https://www.cubesat-propulsion.com/standard-micro-propulsion-system/, 2020.

[6] H. Barber, G. Falkenstein, C. Buell, and R. Gurnitz, "Microthrusters employing catalytically reacted n2-o2-h2 gas mixtures, tridyne," *Journal of Spacecraft and Rockets*, vol. 8, no. 2, pp. 111–116, 1971.

[7] P. W. Atkins, *Atkins' Physical chemistry*. New York: W.H. Freeman, 2006.

[8] T. Jennings, H. Voge, and W. Armstrong, "Catalysts for initiating the hydrogen-oxygen reaction at 78° k," *Journal of Catalysis*, vol. 24, no. 3, pp. 493–501, 1972.

[9] J. Clark, "The effect of catalysts on reaction rates," 2018. `https://www.chemguide.co.uk/physical/basicrates/catalyst.html`, Last accessed on 2020-08-02.

[10] J. Witte, "Orr catalysts with pt-based csnps: d-band theory," 2011. `https://sites.google.com/site/orrcatalysiswithptbasedcsnps/home/d-band-theory`, Last accessed on 2020-08-03.

[11] S. K. Dharan G., Hanania J. and D. J., "Conduction band," 2018. `https://energyeducation.ca/encyclopedia/Conduction_band`, Last accessed on 2020-08-03.

[12] M. Rightley and F. Williams, "Burning velocities of co flames," *Combustion and flame*, vol. 110, no. 3, pp. 285–297, 1997.

[13] L. Das, "Hydrogen-oxygen reaction mechanism and its implication to hydrogen engine combustion," *International Journal of Hydrogen Energy*, vol. 21, no. 8, pp. 703–715, 1996.

[14] S. Gordon and B. McBride, "Computer program for calculation of complex chemical equilibrium compositions and applications i. analysis," Tech. Rep. NASA-RP-1311, E-8017, NAS 1.61:1311, National Aeronautics & Space Administration, 1995.

[15] G. Sutton and O. Biblarz, *Rocket propulsion elements*. Wiley, 8 ed., 2010.

[16] R. A. Spores, "Gpim af-m315e propulsion system," in *51st AIAA/SAE/ASEE Joint Propulsion Conference*, p. 3753, 2015.

[17] EPA, "Hydrazine," tech. rep., Environmental Protection Agency, 2016. `https://www.epa.gov/sites/production/files/2016-09/documents/hydrazine.pdf`.

[18] C. Maleix, P. Chabernaud, R. Brahmi, R. Beauchet, Y. Batonneau, C. Kappenstein, M. Schwentenwein, R.-J. Koopmans, S. Schuh, and C. Scharlemann, "Development of catalytic materials for decomposition of adn-based monopropellants," *Acta Astronautica*, vol. 158, pp. 407–415, 2019.

[19] E. Savrun and S. J. Sawhill, "Corrosion resistant catalysts for decomposition of liquid monopropellants," Oct 2015.

[20] R. Amrousse, T. Katsumi, N. Azuma, and K. Hori, "Hydroxylammonium nitrate (han)-based green propellant as alternative energy resource for potential hydrazine substitution: From lab scale to pilot plant scale-up," *Combustion and Flame*, vol. 176, pp. 334–348, 2017.

[21] K. Anflo and B. Crowe, "In-space demonstration of an adn-based propulsion system," in *47th AIAA/ASME/SAE/ASEE Joint Propulsion Conference & Exhibit*, p. 5832, 2011.

[22] A. S. Gohardani, J. Stanojev, A. Demairé, K. Anflo, M. Persson, N. Wingborg, and C. Nilsson, "Green space propulsion: Opportunities and prospects," *Progress in Aerospace Sciences*, vol. 71, pp. 128–149, 2014.

[23] R. Masse, M. Allen, R. Spores, and E. A. Driscoll, "Af-m315e propulsion system advances and improvements," in *52nd AIAA/SAE/ASEE Joint Propulsion Conference*, p. 4577, 2016.

[24] R. Grist, *Design and Experimental Investigation of a Hydroxyl Ammonium Nitrate Based Workhorse Microthruster*. PhD thesis, University of Washington, 2016.

[25] K. Hori, T. Katsumi, S. Sawai, N. Azuma, K. Hatai, and J. Nakatsuka, "Han-based green propellant, shp163–its r&d and test in space," *Propellants, Explosives, Pyrotechnics*, vol. 44, no. 9, pp. 1080–1083, 2019.

[26] R. Pahl and C. Tutza, *Design, test, and validation of a refrigerant-based cold-gas propulsion system for small satellites*. PhD thesis, Missouri University of Science and Technology, 2010.

[27] D. Carroll, J. Cardin, R. Burton, G. Benavides, N. Hejmanowski, C. Woodruff, K. Bassett, D. King, J. Laystrom-Woodard, L. Richardson, C. Day, K. Hageman, and R. Bhandari, "Propulsion unit for cubesats (PUC)," in *62nd JANNAF Propulsion Meeting*, 06 2015.

[28] VACCO, "CuSP Propulsion System." Brochure, 2010. `https://www.cubesat-propulsion.com/wp-content/uploads/2017/08/X16038000-01-data-sheet-080217.pdf`.

[29] materialise manufacturing, "3D Printing Materials Datasheets." Brochure, 2020. `https://www.materialise.com/system/files/resources/materialise_datasheets_25_06_20.pdf`.

[30] U. Maas and J. Warnatz, "Ignition processes in hydrogen-oxygen mixtures," *Combustion and flame*, vol. 74, no. 1, pp. 53–69, 1988.

[31] B. Lewis, *Combustion, flames, and explosions of gases*. Orlando: Academic Press, 1987.

[32] D. G. Goodwin, R. L. Speth, H. K. Moffat, and B. W. Weber, "Cantera: An object-oriented software toolkit for chemical kinetics, thermodynamics, and transport processes." `https://www.cantera.org`, 2020. Version 2.4.0.

[33] P. Boivin, *Reduced-kinetic mechanisms for hydrogen and syngas combustion including autoignition*. PhD thesis, Escuela Politécnica Superior, 2011.

[34] E. Schmidt, *Hydrazine and its derivatives : preparation, properties, applications*. New York: Wiley-Interscience, 2001.

[35] H. Burge, M. Ladacki, and R. Roberts, "Investigation of catalytic ignition of oxygen/hydrogen systems final report, 15 jun. 1964-15 oct. 1965," *NASA Technical Reports*, 1965.

[36] J. C. for Aerospace Technology Innovation (JCATI), "Jcati funded research: 2020 jcati awardees. further development of a tridyne microthruster for cubesat applications.," 2020. `https://jcati.org/funding/jcati-funded-research`, Last accessed on 2020-08-10.

[37] I. S. in Space (ISIS), "Isis 3-unit cubesat dimensions," tech. rep., ISIS, 2014. https://www.isispace.nl/wp-content/uploads/2015/12/ISIS.STS_.0.1.003-RevB-Sheet1-1-3U-CubeSat-Dimensions-A0.pdf.

Appendix A

APPENDIX

A.1 NASA-CEA .inp file maker and .plt file viewer Codes

```
# -*- coding: utf-8 -*-
"""
Created on Thu Sep 19 09:50:58 2019

@author: bhend
"""
import numpy as np

lines = ['problem    ',
         '       rocket   fac ac/at=40 tcest ,k=1400',
         '   p,bar='+','.join([str(c) for c in np.arange(1,20,1)]),
         '   sup,ae/at=10, 25, 50',
         'react  ',
         '   fuel=H2 moles=6 t,k=',
         '   oxid=O2 moles=3 t,k=',
         '   name=N2 moles=91 t,k=',
         'output   short',
         '     plot p t rho gam h mw mach aeat cf isp vis cond',
         ' end'
         '']
```

```
nTemp = 20
Temps = 273 + np.linspace(20, 950, nTemp)

for i in range(nTemp):


    fname = '%02d.inp'%i

    with open(fname, 'a') as file:
        for row in lines:
            if 'k=' in row and 'tcest' not in row:
                row += str(int(Temps[i]))

            file.write(row+'\n')
```

```
# -*- coding: utf-8 -*-
"""
Created on Tue Sep  3 11:40:20 2019

@author: bhend
"""

import numpy as np
import matplotlib.pyplot as plt
import matplotlib
from glob import glob
import re
from scipy.signal import savgol_filter as sgf
matplotlib.rcParams.update({'font.size': 14})
psia2bar = 0.0689476



###
#Load the data
pltfiles = glob('plt_files/*.plt')

numPressures = 19
numTemps = 20
T0s = 273 + np.linspace(20, 950, numTemps)
data = np.zeros([int(6*numTemps*numPressures),14])
null = np.ones(14)*np.nan
tick, tickprev=0,0
```

```
for f in pltfiles:
    tempdata = np.genfromtxt(f)

    tick = tickprev + len(tempdata)
    data[tickprev:tick,:12]=tempdata
    tickprev=tick



data=np.swapaxes(data,0,1)

data[-2] = (data[3]*data[1]*8314/data[5])**0.5 #sound speed a-m/s
data[-1] = data[6]*data[-2] #velocity v-m/s

data = np.rollaxis(
        np.asarray(
        np.split(data, int(numPressures*numTemps), axis=1)), 0, 3)

data = np.rollaxis(
        np.asarray(
        np.split(data, numTemps, axis=-1)), 0, 3)
#Data shape is now [property, location, T0, P0]
# #14 entries denoting properties:
# data = data[:,:,0,:]
# data = np.delete(data,[3,4],axis=1)
P, Temp, rho, gam, h, MW, mach, aeat, cf, Isp, vis, cond, a, v = data
```

```
P*=1e5 #bar to pa

#6 entries follow denoting locations:
#0:INJECTOR (I)        1:COMB END (C)        2:THROAT (T)        3,4,5: Exits



P0s = P[0,0]*14.504e-5 #pa to psi
#plt.plot(T0s, Temp[0,:,0])

# Dt_ = np.linspace(1,50,50)
# T_ = np.linspace(.1,1,50)
# Dt, T, mdotT, mdotDt = np.zeros([4,50,len(P0s)])
# Gamma = (gam**0.5 * (2/(gam+1)) ** ((gam+1)/(2*(gam-1))))[2][0]
# MW = MW[0][0]

# for i in range(50):
#       At = T_[i]/(cf[3]*P[1])
#       Dt[i] = 1e3/.0254 * (4/np.pi*At)**0.5
#       mdotT[i] = 1e3*P[2]*At*Gamma / (Temp[2]*8314/MW)**0.5 #mass flow; g/s

#       At = np.pi/4 * (Dt_[i]*.0254e-3)**2 #
#       T[i] = cf[3]*P[1]*At#At = T/(cf_e*P_c)
#       mdotDt[i] = 1e3*P[1]*At*Gamma / (Temp[1]*8314/MW)**0.5 #mass flow; g/s
```

```
# plt.contourf(P0s[:9], Dt_, mdotDt[:,:9])
# clb2 = plt.colorbar()
# clb2.ax.set_title(r'$\dot{m}$ (g/s)', pad=14)

# plt.contourf(P0s[:9], Dt_, T[:,:9])
# clb = plt.colorbar()
# clb.ax.set_title('T (N)', pad=14)

# plt.xlabel('Chamber Pressure (psi)')
# plt.ylabel('Throat Diameter (thou)')
# plt.tight_layout()
#plt.savefig('CEA_T_vs_Pc_and_Dt.png', dpi=200, bbox_inches='tight')
# T = 1 #N; design variable
# ###Plotting!
# # fig, ax = plt.subplots(1,2, figsize=(12,5))
# At, Dt, Gamma, mdot = np.zeros([4,3,numTemps,numPressures])
# Ac = np.pi/4 *(.5*.0254)**2
# for i in range(3):
#     At[i] = T/(cf[i+3]*P[1])        #At = T/(cf_e*P_c)
#     Dt[i] = 1e3/.0254 * (At[i]*4/np.pi)**0.5 #throat diam; .001 inch
#     Gamma[i] = (gam**0.5 * (2/(gam+1)) ** ((gam+1)/(2*(gam-1))))[2]
#     mdot[i] = 1e3*P[2]*At[i]*Gamma[i] / (Temp[2]*8314/MW[2])**0.5 # g/s

#     plt.figure()
#     plt.contourf(P0s, T0s, mdot[i])
#     plt.colorbar()
```

```
fig, ax = plt.subplots()
ax = [ax, ax.twinx()]
ax[0].plot(T0s, Temp[0,:,0], c='C0', label=r'$T_{flame}$')
ax[1].plot(T0s, Temp[0,:,0]-T0s,c='C1',label=r'$\Delta T$')

ax[0].legend(loc='center left')
ax[1].legend(loc='center right')

ax[0].set_ylabel('Adiabatic Flame Temperature (K)',labelpad=10)
ax[1].set_ylabel('Rise from Initial Temperature (K)',labelpad=20)

ax[0].set_xlabel('Initial Temperature (K)')
plt.tight_layout()
plt.savefig('CEA_Tflame_vs_T0.png',dpi=200,bbox_inches='tight')
```

A.2 Performance vs. Storage Pressure Code

```
# -*- coding: utf-8 -*-
"""
Created on Wed Aug  7 10:30:46 2019

@author: bhend

This program is for comparing the perfomance of various thruster types.
Specifically, we will look at cold gas, refrigerant, and Tridyne thrusters
For cold gas, we assess N2
For refrigerants, we assess R-134a (later maybe Isobutane or HFC 236fa)
For Tridyne, we have 88% N2, 4% O2, and 8% H2

For each system, we estimate Isp, m_p, and m_f
m_p is estimated from a common target deltaV and the calculated Isp
m_f is estimated from the required pressure P_p of the propellant chamber,
    and how that affects the chamber mass.
    We assume identical chamber volumes, and consider additional masses
    such as a catalyst bed heater/psu if relevant.
"""

import numpy as np
import matplotlib.pyplot as plt
import matplotlib
matplotlib.rcParams.update({'font.size': 14})
import seaborn as sns
```

```
R = 8.314 # kg m^2/(mol K s^2)
pi = np.pi

#Tridyne propellant properties
y = 1.35 #specific heat ratio
M = 27.4 #kg/kmol
Isp = 146 #s;
T = 273 #K; assume calorically perfect ideal gas
Px = np.linspace(1,1000,1000)*1e5
Z = 1.055 #compressibility at P,T


#Aluminum vessel properties
metals = [r'$AlSi_{10}Mg$', '316 SS', r'$Ti_6Al_4V$']
rhos = [2.65e6, 7.95e6, 4.39e6]
sigys = [190e6, 340e6, 980e6]
FSs = [8, 3.7, 2.77]
FS_pfs = [[-6.21051e-24,  1.47945e-15, -1.40204e-07,  7.85279e+00],
          [-1.77388e-25,  7.23044e-17, -1.73944e-08,  3.69889e+00],
          [-2.862194-27,  3.21233e-18, -3.000894e-09,  2.76999e+00]]
FS2_pfs = [[ 4.07507e-27, -4.55959e-18,  4.13947e-10,  2.49999e+00],
           [ 1.76350e-25, -7.09795e-17,  5.36311e-09,  2.49973e+00],
           [ 3.37396e-24, -7.64198e-16,  4.27241e-08,  2.50942e+00]][::-1]

r = np.linspace(10e-3,48e-3,1000)
l = np.linspace(30e-3,80e-3,1000)
```

```
rr, ll = np.meshgrid(r, l)


def optimize_dimensions(mpt, Ve):
    ir, il = len(r)-1, len(l)-1
    if np.ma.is_masked(Ve)==True:
        while np.ma.is_masked(Ve[il,:])==True:
            il-=1
            if il==0:
                ir = np.argmax(mpt[il,:])
                break
    return ir, il


#Calculate dimensions and masses
V = pi*rr**2*ll + 4/3*pi*rr**3

mpo, mvo, V_p, V_t, Pbs, dVs, Its = np.zeros([7, 4, 3, len(Px)])

Vs = np.array([360, 700, 1000, 1440])*1e-6
vacco_md = np.array([639, 799, 956, 1144])
vacco_mp = np.array([209, 557, 857, 1314])
vacco_mt = vacco_md + vacco_mp

vacco_itot = np.array([82, 219, 336, 515])
vacco_dv = 9.81*54*np.log((vacco_md*5+vacco_mp)/(vacco_md*5))
```

```
# for i_sizes in range(4):
#       Vmax = 0.8*Vs[i_sizes]
#       md = vacco_md[i_sizes]*.6 #dry mass
#       mpay = vacco_md[i_sizes]*4 #payload mass
#       mm = mpay+md


#       for j in range(3):
#           rho, sigy = rhos[j], sigys[j]
#           for i in range(len(Px)):
#               P = Px[i]
#               FS = (2.5/np.polyval(FS_pfs[j],P)) * FSs[j] #dynamically adjust
#               FS *= 2.5/np.polyval(FS2_pfs[j],P) #FS vs. P for proper Pb/P
#               tc = FS* P*rr/(sigy-.6*P) #cylinder thickness; m
#               th = FS* P*rr/(2*sigy-.2*P) #head thickness; m
#               V_eff = pi*(rr+tc)**2*ll + 4/3*pi*(rr+th)**3

#               mv = (V_eff - V) * rho #g
#               mp = P*V*M/(R*T*Z) #g
#               mt = mv+mp


#               #Mask arrays for plotting based on volumes too large
#               mpt = np.ma.array(mp/mt, mask=V_eff >Vmax)
#               Ve = np.ma.array(V_eff, mask=V_eff >Vmax)
```

```
#                #Choose optimal dimensions
#                #il = np.where(l>=.0875)[0][0]

#                ir, il = optimize_dimensions(mpt, Ve)
#                ro, lo = r[ir]*1e2, l[il]*1e2

#                #Calculate burst pressure from chosen thicknesses
#                tco, tho = tc[il,ir], th[il,ir]
#                Pb1 = tco*sigy/(r[ir]+.6*tco)
#                Pb2 = tho*2*sigy/(r[ir]+.2*tho)
#                Pb = min(Pb1, Pb2)
#                # print('%.2f\t%.2f\t%.2f\t%.2f\t%.2f\t%.2f'%
#                        (P*1e-6,Pb/P,tco*1e2,tho*1e2,mv[il,ir]*1e3,mp[il,ir]*1e3)
#                #Calculate perfomance
#                mpo[i_sizes, j, i], mvo[i_sizes, j, i], V_p[i_sizes, j, i],
#                   V_t[i_sizes, j, i], Pbs[i_sizes, j, i] = mp[il,ir], mv[il,ir],
#                       V[il,ir], Ve[il, ir], Pb

#            dVs[i_sizes, j] = 9.81*Isp*np.log((mm+mpo[i_sizes, j]+\
#                                    mvo[i_sizes, j])/(mm+mvo[i_sizes, j]))
#            Its[i_sizes, j] = 9.81*Isp*mpo[i_sizes, j]*1e-3
```

Vs*=1e3

Px*=1e-6

```
# np.save('dVs_size_material_pressure.npy',dVs)
# np.save('Its_size_material_pressure.npy',Its)
# np.save('mpo_size_material_pressure.npy',mpo)
# np.save('mvo_size_material_pressure.npy',mvo)
# np.save('V_p_size_material_pressure.npy',V_p)
# np.save('V_t_size_material_pressure.npy',V_t)


dVs = np.load('dVs_size_material_pressure.npy')
Its = np.load('Its_size_material_pressure.npy')
mpo = np.load('mpo_size_material_pressure.npy')
mvo = np.load('mvo_size_material_pressure.npy')
V_p = np.load('V_p_size_material_pressure.npy')
V_t = np.load('V_t_size_material_pressure.npy')



metal = 2
sbtits = [r'$m_p$ (g)', r'$m_{tank}$ (g)']
cmaps = [plt.cm.viridis, plt.cm.magma]
vecs = [mpo, mvo]

fig, ax = plt.subplots(1,2, figsize=(9.2,4))
for h in range(2):
    cf = ax[h].contourf(Px, Vs, vecs[h][:,metal], cmap = cmaps[h])

    plt.colorbar(cf, ax=ax[h])
```

```
    ax[h].set_title(sbtits[h])
    ax[h].set_xlim(Px[0],Px[-1])

    ax[h].set_ylim(Vs[0],Vs[-1])
    ax[h].set_xlabel('Storage Pressure (MPa)')

    ax[h].set_yticks(Vs)

ax[0].set_ylabel('CubeSat Size (U)')
plt.tight_layout()
plt.subplots_adjust(wspace=.3)
plt.suptitle('Titanium Propellant Tank')

#plt.savefig('Titanium_masses.png', dpi=200, bbox_inches='tight')




# fig, ax = plt.subplots()
# ax = [ax, ax.twinx()]
```

```
# vacco_ldV = ax[0].hlines(63, 0, 15, label='VACCO',
#                 color='C3', linestyle='--', alpha=.4)
# vacco_lItot = ax[1].hlines(336, 85, 100, label='VACCO',
#                 color='C4', linestyle='--', alpha=.4)
# dVps, dIts = [], []
# for j in range(3):

#     try:
#         P_Itot_tradeoff = Px[np.where(tot_impulse[j]>336)[0][0]]*1e-6
#     except IndexError:
#         P_Itot_tradeoff = Px[0]*1e-6

#     try:
#         P_dV_tradeoff = Px[np.where(deltaV[j]>63)[0][0]]*1e-6
#     except IndexError:
#         P_dV_tradeoff = Px[-1]*1e-6



#     dVps.append(ax[0].plot(Px*1e-6, deltaV[j], label=metals[j])[0])
#     dIts.append(ax[1].plot(Px*1e-6, tot_impulse[j], c='w', alpha=0)[0])



# legend1 = ax[0].legend(dVps, metals,
#                        title='Tank Material', loc='upper left')
# legend2 = ax[1].legend([vacco_ldV, vacco_lItot],
#                        [r'$\Delta V$', r'$I_{tot}$'], loc='center right'
```

```
#                                   title='VACCO',  bbox_to_anchor=(1,.6))
# ax[0].add_artist(legend1)
# ax[1].add_artist(legend2)



# ax[0].set_xlim([0,100])
# ax[0].set_xlabel(r'Initial Propellant Storage Pressure, $P_0$ (MPa)')
# ax[0].set_ylabel('Total Velocity Change (m/s)')
# ax[1].set_ylabel('Total Impulse (N-s)')

# fig.tight_layout()
# fig.set_size_inches(7.75, 4.75)
# plt.savefig('Itot_dV_vs_P0.png',dpi=300,bbox_inches='tight')



# fig, ax = plt.subplots()
# m1, m2 = [], []

# for i in range(3):
#     m1.append(ax.plot(Px*1e-6, mvo[i]*1e-3,
#                       label='Pressure Vessel', c='C%i'%i)[0])
#     m2.append(ax.plot(Px*1e-6, mpo[i]*1e-3, label='Propellant',
```

```
#                       linestyle='--', c='C%i'%i)[0])

#     ax.set_ylabel('Velocity (m/s)')
#     ax.set_ylabel('Mass (kg)')


# leg_colors = m1
# leg_lines = [m1[0], m2[0]]
# legend0 = ax.legend(leg_colors, metals, title='Tank Material',
#                     loc='upper left')
# legend2 = ax.legend(leg_lines, ['Pressure Vessel', 'Propellant'],
#                     loc='center right', bbox_to_anchor=(1,.6))
# ax.add_artist(legend0)
# ax.add_artist(legend2)


# plt.title('')
# plt.title('Pressure vessel volume constraint: %.2fU\n'%(Vmax*1e3)+\
#           '4 kg payload + %.2f kg dry mass'%(mdry*1e-3), fontsize=15)
# fig.tight_layout()
# fig.set_size_inches(7.75, 4.75)
# plt.savefig('masses_vs_P0.png',dpi=300,bbox_inches='tight')
```

A.3 Cantera Auto-flammability Estimate Code

```
# -*- coding: utf-8 -*-
"""
Created on Fri May  8 11:08:28 2020

@author: bhend
"""

import numpy as np
import cantera as ct
import matplotlib.pyplot as plt

psi2pa = 101325/14.7



#Specify the number of time steps and the time step size
nt = int(2e3)
dt = 1e-3 #s
time = np.linspace(dt, dt*nt, nt)

def Autoignition_Timing(T0, P0, H2x):
    #Mechanism used for the process
    gas = ct.Solution('Boivin_newTherm.cti','h2_12s_mix')
    gas.TPX = T0, P0, ('H2:%i, O2:%i, N2:%i'%(H2x,H2x/2,100-3/2*H2x))

    #Storage space
    nfrac = np.zeros((gas.n_species,nt))
```

```
time, temp, pressure = np.zeros([3,nt])
mfrac = np.zeros([gas.n_species, nt])

# Create the batch reactor and fill it with the gas
r = ct.IdealGasReactor(gas)
# Now create a reactor network consisting of the single batch reactor
sim = ct.ReactorNet([r])

##################################################################
# Run the simulation
t = 0.0
#Loop for nt time steps of dt seconds.
for n in range(nt):
    t += dt
    sim.advance(t)
    #save the time and temperature of each time step
    time[n] = t
    temp[n] = r.T
    pressure[n] = r.thermo.P
    mfrac[:,n] = r.thermo.Y

#Get Autoignition Timing
if temp[-1] < temp[0]+10: # no reaction
    if temp[-1]<1100:
        autoign_time = 1.1
    else: autoign_time = 0
else: autoign_time = time[np.diff(temp).argmax()] # maximum temp gradient
```

```
    if autoign_time > 1: autoign_time = 1.1

    #Return solution
    return temp, pressure, autoign_time


all_data = []
nT, nP = 40, 40

T0_list = np.linspace(700, 1000, nT)
P0_list = np.linspace(14.7, 500, nP)*psi2pa
H0_list = np.linspace(0,64,30)
temp, pressure = np.zeros([2,len(H0_list),nT,nP,nt])
at = np.zeros([len(H0_list),nT,nP])

for iH, H0 in enumerate(H0_list):
    for iT in range(nT):
        for iP in range(nP):
            T0, P0 = T0_list[iT], P0_list[iP]

            temp_, pressure_, autoign_time = Autoignition_Timing(T0,P0,H0)

            at[iH, iT, iP] = autoign_time
            temp[iH, iT, iP] = temp_
            pressure[iH, iT, iP] = pressure_
```

```
    fig, ax = plt.subplots(1,1, figsize=(10,6))
    vmax=100
    vmin=0
    levels = [0, 0.01, 0.1, 0.5, 1, 1.1]
    plt.contourf(P0_list/psi2pa, T0_list, at[iH], levels=levels,
                                cmap=plt.cm.magma_r)
    cb = plt.colorbar()
    cb.ax.set_title('Autoignition\nTime (s)')
    cb.ax.set_yticklabels(['0','0.01', '0.1', '0.5', '1','>1\n(No Ignition)']
    cb.ax.invert_yaxis()
    ax.set_title(r'Initial $H_2$' + ' = %i%%'%H0)
    plt.xlabel(r'$P_0$ (psi)')
    plt.ylabel(r'$T_0$ (K)', rotation=0, labelpad=15)

    #plt.savefig('P0_T0_autoign_H0_%02d.png'%H0, dpi=300, bbox_inches='tight'
    #plt.close('all')



nT, nH = 400, 200
T0_list = np.linspace(700, 1000, nT)
H0_list = np.linspace(0,45,nH)
autoign_time, temp = np.zeros([2, nT, nH])
for iH, H0 in enumerate(H0_list):
    for iT, T0 in enumerate(T0_list):
        t,p,at = Autoignition_Timing(T0, 100*psi2pa, H0)
```

```
    temp[iT,iH], autoign_time[iT,iH] = t[-1],at
print(iH)

vmax=100
vmin=0
levels = [0, 0.01, 0.1, 0.5, 1, 1.1]

fig, ax = plt.subplots(1,2,figsize=(10,4.5))
cf = ax[0].contourf(H0_list, T0_list, temp,
                    cmap=plt.cm.viridis)
cb = fig.colorbar(cf, ax=ax[0])
ax[0].set_title('Flame Temperature (K)')


cf = ax[1].contourf(H0_list, T0_list, autoign_time, levels=levels,
                    cmap=plt.cm.magma_r)
cb = fig.colorbar(cf, ax=ax[1])
ax[1].set_title('Autoignition Time (s)')
cb.ax.set_yticklabels(['0','0.01', '0.1', '0.5', '1','>1\n(No Ignition)'])
cb.ax.invert_yaxis()


fig.tight_layout()
plt.subplots_adjust(wspace=.4)
```

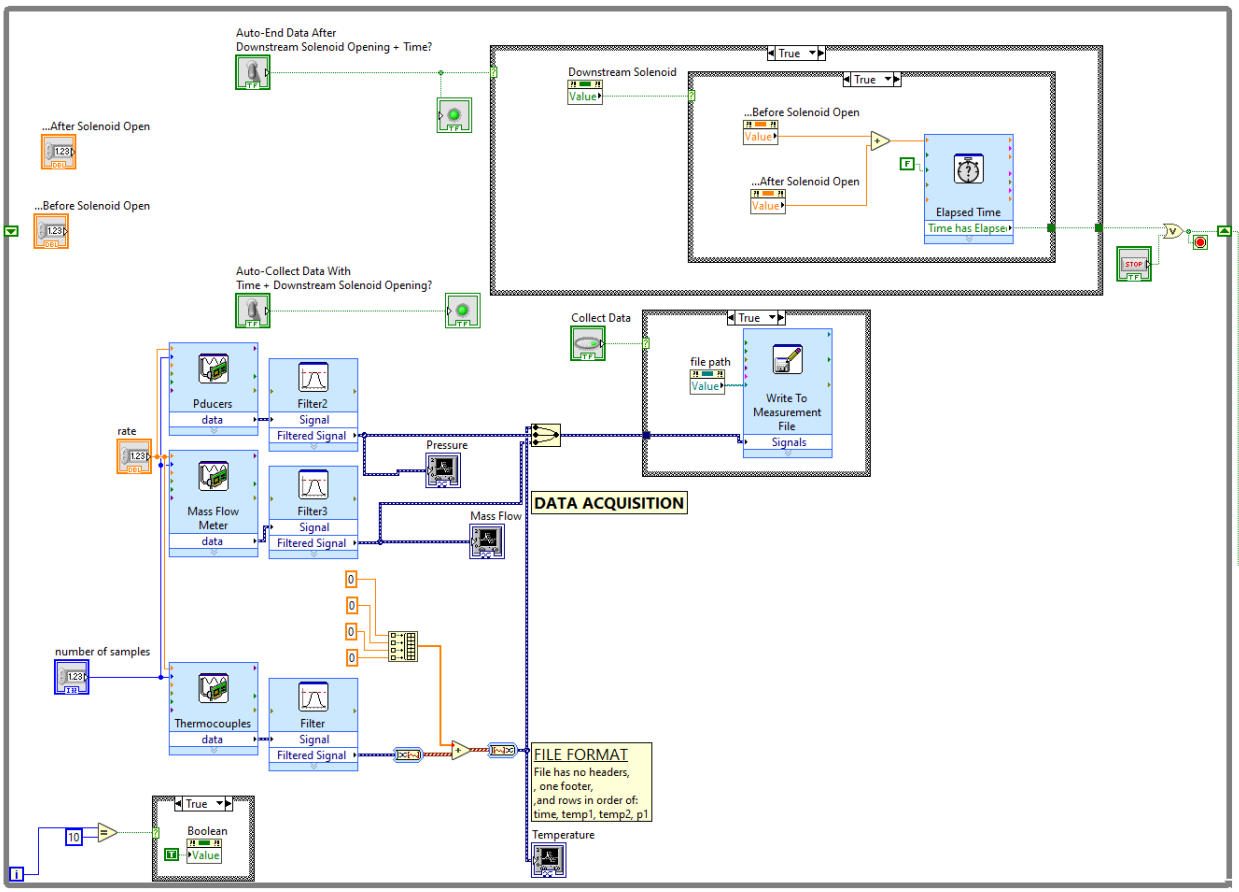

Figure A.1: LabVIEW GUI back-end, main loop

A.4 LabVIEW Graphical User Interface Back-End

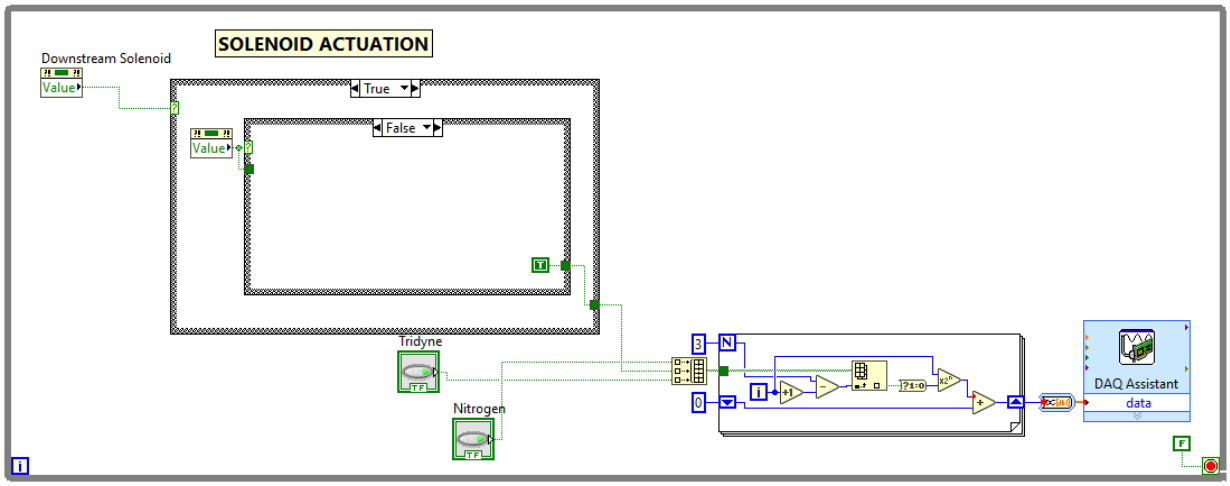

Figure A.2: LabVIEW GUI back-end, solenoid loop

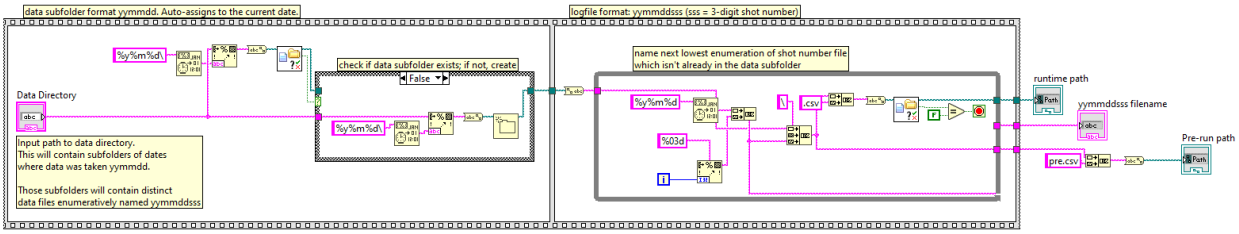

Figure A.3: LabVIEW GUI back-end, file naming loop

A.5 Experimental Data Organization into a DataFrame

```
# -*- coding: utf-8 -*-
"""
Spyder Editor

This is a temporary script file.
"""
import numpy as np
from scipy.signal import find_peaks as fp
from scipy.signal import savgol_filter as sf
from glob import glob
import pandas as pd

shots = glob('relevant_shots\\*.csv')
CatalystShots = ['200731', '200805', '200810']
NitrogenShots = ['200720']

psi2pa = 6894.76 #pa/psi
Patm = 14.6959 #psi
alpha = 8.8e-6 #in/(in F)
def hot_At(At, T): #new hole area from thermal expansion
    Tf = (T - 273.15)*9/5 + 32
    Ah = At*(1+2*alpha*Tf)
    return Ah

def hot_n2(mdot, Ti): #subtract convective heat transfer based on hot N2
    return np.polyval([199.70414201, 290.54733728], mdot)*Ti/1100
```

```
def gamma(T):
    return np.polyval([ 3.29969583e-08, -1.10209257e-04,  1.38287615e+00], T)

def rho_(P,T,Mmass): #P in psi and T in K, rho in g/m3
    return P*psi2pa*Mmass/(8.314*T)

def Tfmax(T): #maximum flame temp from CEA
    return np.polyval([0.93525223, 510.49081167], T)

def get_Data(s):
    snum = s[-13:-4]
    yymmdd = snum[:-3]

    run = np.swapaxes( np.genfromtxt(s, delimiter=',',skip_footer=1) ,0,1)
    t, T, P, m_slm = run[0], run[1:5,:], run[5:9,:], run[9]
    t-=5
    T+=273.15



    if yymmdd in NitrogenShots:
        gastype = 'Nitrogen'
        Mmass = 28.02
        gam = 1.4
    else:
        gastype = 'Tridyne'
        Mmass = 27.395
```

```
    gam = gamma(T[3])
cgam = ((gam*Mmass/8314)**.5) * ((gam+1)/2)**(-(gam+1)/(2*gam-2))


if yymmdd in CatalystShots:
    shottype = 'Catalyst_Bed'
    dt = 0.052 *.0254
    m_const = .999
else:
    shottype = 'Pebble_Bed'
    dt = 0.05 *.0254
    m_const = .807

At = np.pi/4 * dt**2
Ah = hot_At(At, T[3])

m = m_slm/60e3*rho_(14.504,273.15,Mmass)
m_th = (Ah*m_const * (((P[-1]+Patm)*psi2pa))/(T[-1]**.5) *cgam) *1e3
Cd = sf(m/m_th,251,1)


if yymmdd in CatalystShots:
    cstar_max = Tfmax(T[1])**0.5/cgam
else:
    Tfadj = hot_n2(m_th[-200:-100].mean(), T[2][:50].mean())
    cstar_max = (Tfmax(T[1] + Tfadj)-50)**0.5/cgam
```

```
    cstar_P = ((P[3]+Patm)*psi2pa*At/(m_th*1e-3))
    cstar_T2 = ((T[2])**.5/cgam)
    cstar_T3 = ((T[3])**.5/cgam)

    ldf = np.swapaxes(
        np.asarray( [t,T[0],T[1],T[2],T[3],P[0],P[1],P[2],P[3],
                     m,m_th,Cd,cstar_T2, cstar_T3, cstar_P,cstar_max] ), 0,1)
    ldf = pd.DataFrame(ldf, columns=ldf_columns)

    ldf['shottype'] = shottype
    ldf['sn'] = snum
    ldf['gastype'] = gastype

    return ldf

''' Indices of sdf
#0: shotnum
#1: P0_preSolenoid
#2: P0
#3: P1
#4: P2
#5: P3
#6: mdot_exp
#7: mdot_th
#8: cstar_T
#9: cstar_P
#10: cstar_max
```

```
#11: T2_i
#12: T3_i
#13: T_th_max
#14: T2max
#15: T3max
#16: t_rise_T2max
#17: t_rise_T3max
#18: dT2_mean
#19: dT3_mean
#20: t_transient_dTmax (Catalyst)
#21: t_rxn_dTmax (Catalyst)
#22: dT2_transient_max (Catalyst)
#23: dT2_rxn_max (Catalyst)
#24: t_res_T2max (Pebble Bed)
#25: t_res_T3max (Pebble Bed)
#26: t_res_T3_noEnd (Pebble Bed)
'''


def get_residence_time(t,T,T_i,T_max,it_rise_Tmax):
    try:
        it_fall_Tmax = it_rise_Tmax+50 + \
                       np.where(T_max - T[it_rise_Tmax+50:] > \
                                0.1*(T_max - T_i))[0][0]
        t_res = t.iloc[it_fall_Tmax] - t[it_rise_Tmax]
        t_noEnd = 0
    except IndexError:
        t_res = t.iloc[-1] - t[it_rise_Tmax]
```

```
        t_noEnd = 1
    return t_res, t_noEnd


def get_Scalar_Data(shotnum, ldf):
    it_start = np.where(ldf['t']>=0)[0][0]

    T2_i, T3_i =[ldf['T%i'%i][it_start-100:it_start-50].mean() for i in [2,3]
    T2_max, T3_max = ldf['T2'].max(), ldf['T3'].max()

    T1_e = ldf['T1'][-200:-100].mean()
    T_max_th = Tfmax(T1_e)



    it_rise_T2max = np.where(T2_max-ldf['T2'] < 0.05*(T2_max-T2_i))[0][0]
    it_rise_T3max = np.where(T3_max-ldf['T3'] < 0.05*(T3_max-T3_i))[0][0]
    t_rise_T2max = ldf['t'][it_rise_T2max]
    t_rise_T3max = ldf['t'][it_rise_T3max]

    eta_cstars = np.asarray([ldf['cstar_T2'],ldf['cstar_T3'],ldf['cstar_P']])
    eta_cstars /= ldf.cstar_max

    lsdf = np.ones(29)*np.nan
    lsdf[0] = ldf['sn'][0]
    lsdf[1] = ldf['P0'][:200].mean() #P0_i
    lsdf[2:9] = [ldf.iloc[:,s+5][-200:-100].mean() for s in range(7)]
    lsdf[9:12] = [eta_cstars[s][-200:-100].mean() for s in range(3)]
```

```
lsdf[12:14] = [T2_i, T3_i]
lsdf[14] = T_max_th
lsdf[15:19] = [T2_max, T3_max, t_rise_T2max, t_rise_T3max]

dT2 = np.gradient(ldf['T2']-ldf['T1'],ldf['t'])
dT3 = np.gradient(ldf['T3']-ldf['T1'],ldf['t'])
dT2_mean = dT2[it_start:it_rise_T2max].mean()
dT3_mean = dT3[it_start:it_rise_T3max].mean()
lsdf[19] = dT2_mean
lsdf[20] = dT3_mean
lsdf[28] = T1_e

if ldf['shottype'][0]=='Catalyst Bed':
    it_dT2_maxs = fp(dT2,prominence=1)[0]
    it_dT2_maxs = it_dT2_maxs[np.argsort(dT2[it_dT2_maxs])][-2:]
    t_dT2_maxs, dT2_maxs = ldf['t'][it_dT2_maxs], ldf['T2'][it_dT2_maxs]

    lsdf[21:23] = t_dT2_maxs
    lsdf[23:25] = dT2_maxs



elif ldf['shottype'][0]=='Pebble Bed':
    it_rise_Tmaxs = [it_rise_T2max, it_rise_T3max]
    for i in [2,3]:
        t_res, t_noEnd = get_residence_time(ldf['t'], ldf['T%i'%i], \
                                            lsdf[i+11], \
                                        lsdf[i+14], it_rise_Tmaxs[i-2])
```

```
            lsdf[23+i] = t_res
        lsdf[27] = t_noEnd
        lsdf[28] += hot_n2(lsdf[7],lsdf[12])
    return lsdf



ldf_columns = ['t','T0','T1','T2','T3','P0','P1','P2','P3',
               'm','m_th','C_d', 'cstar_T2','cstar_T3','cstar_P','cstar_max']
lsdf_columns = ['sn', 'P0_i', 'P0', 'P1', 'P2', 'P3', 'mdot_exp', 'mdot_th',
                'C_d', 'eta_cstar_T2', 'eta_cstar_T3', 'eta_cstar_P', 'T2_i',
                'T_th_max', 'T2_max', 'T3_max', 't_rise_T2max',
                't_rise_T3max', 'dT2_mean', 'dT3_mean', 't_transient_dTmax',
                't_rxn_dTmax', 'dT2_transient_max', 'dT2_rxn_max',
                't_res_T2', 't_res_T3', 't_res_T3_noEnd', 'T1_e']

df_list, sdf_list = [], []
for i,s in enumerate(shots):
    ldf = get_Data(s) #local dataframe
    lsdf = get_Scalar_Data(s,ldf) #local scalar dataframe

    df_list.append(ldf)
    sdf_list.append(lsdf)

df = pd.concat(df_list, ignore_index=True).reset_index() #raw dataframe
sdf = pd.DataFrame.from_records(np.asarray(sdf_list), columns=lsdf_columns)
sdf['sn'] = sdf.astype({'sn': 'int32'}).astype({'sn': 'str'})
```

```
sdf['shottype'] = \
    [df['shottype'][df['sn']==sn].iloc[0] for sn in df['sn'].unique()]

sdf['gastype'] = \
    [df['gastype'][df['sn']==sn].iloc[0] for sn in df['sn'].unique()]

sdf['mm'] = [df['sn'][df['sn']==sn].iloc[0][2:4] for sn in df['sn'].unique()]

sdf['dd'] = [df['sn'][df['sn']==sn].iloc[0][4:6] for sn in df['sn'].unique()]

sdf['Cd'] = sdf['mdot_exp']/sdf['mdot_th']

a = {sn:df['m_th'][df['sn']==sn].iloc[-200:-100].mean() for \
     sn in df['sn'].unique()}

b = {sn:df['sn'][df['sn']==sn].iloc[0][:-3] for \
     sn in df['sn'].unique()}

c = {sn:df['sn'][df['sn']==sn].iloc[0][-3:] for \
     sn in df['sn'].unique()}

d = {sn:df['T2'][df['sn']==sn].iloc[:50].mean() for \
     sn in df['sn'].unique()}

e = {sn:df['T3'][df['sn']==sn].iloc[:50].mean() for \
     sn in df['sn'].unique()}
```

```
f = {sn:df['P3'][df['sn']==sn].iloc[-200:-100].mean() \
     for sn in df['sn'].unique()}

g = {sn:df['T1'][df['sn']==sn].iloc[-200:-100].mean() \
     for sn in df['sn'].unique()}

# df['m_s'] = [a[row['sn']] for (i,row) in df.iterrows()]
# df['mmdd'] = [b[row['sn']] for (i,row) in df.iterrows()]
# df['sss'] = [c[row['sn']] for (i,row) in df.iterrows()]
# df['T2_i'] = [d[row['sn']] for (i,row) in df.iterrows()]
# df['T3_i'] = [e[row['sn']] for (i,row) in df.iterrows()]
# df['P3_i'] = [f[row['sn']] for (i,row) in df.iterrows()]
# df['T1_e'] = [f[row['sn']] for (i,row) in df.iterrows()]

# #Save dataframes
# df.to_pickle('relevant_shots_vectors1.pkl')
sdf.to_pickle('relevant_shots_scalars.pkl')



# sdf = pd.read_pickle('relevant_shots_scalars.pkl')
# df = pd.read_pickle('relevant_shots_vectors.pkl')
```